UNIVERSIDAD COMPLUTENSE DE MADRID
FACULTAD DE CIENCIAS QUÍMICAS

TESIS DOCTORAL

Estudio computacional de materiales como electrodo positivo para baterías recargables de calcio

Computational Investigation of cathode materials for rechargeable calcium batteries

MEMORIA PARA OPTAR AL GRADO DE DOCTOR

PRESENTADA POR

Arturo Torres Gutiérrez

Directora

Mª Elena Arroyo y de Dompablo

Madrid

UNIVERSIDAD COMPLUTENSE DE MADRID
FACULTAD DE CIENCIAS QUÍMICAS

TESIS DOCTORAL

ESTUDIO COMPUTACIONAL DE MATERIALES COMO ELECTRODO POSITIVO PARA BATERÍAS RECARGABLES DE CALCIO

MEMORIA PARA OPTAR AL GRADO DE DOCTOR

PRESENTADA POR

ARTURO TORRES GUTIÉRREZ

DIRECTOR

Mª ELENA ARROYO Y DE DOMPABLO

UNIVERSIDAD COMPLUTENSE DE MADRID

FACULTAD DE CIENCIAS QUÍMICAS

DEPARTAMENTO DE QUÍMICA INORGÁNICA

TESIS DOCTORAL

Estudio computacional de materiales como electrodo positivo para baterías recargables de calcio

Computational Investigation of cathode materials for rechargeable calcium batteries

MEMORIA PARA OPTAR AL GRADO DE DOCTOR

PRESENTADA POR

Arturo Torres Gutiérrez

DIRECTORA

Mª Elena Arroyo y de Dompablo

Madrid, 2020

El trabajo desarrollado en esta Tesis Doctoral se ha llevado a cabo en el Departamento de Química Inorgánica I de la Universidad Complutense de Madrid gracias a un contrato predoctoral financiado por el poyecto CAlcium Rechargeable BAttery Technology (CARBAT) dentro de las acciones FET (Future and Emerging Technologies) del programa de Investigación e Innovación de la Unión Europea Horizon 2020 (convocatoria 2016/17). Los recursos computacionales han sido cofinanciados por el Ministerio de Educación y Ciencia a través del proyecto MALTA-CONSOLIDER-CSD2007-00045, del Ministerio De Economía y Competitividad (MAT2015-71070-REDC) y del Ministerio de Ciencia, Innovación y Universidades (RED2018-102612-T).

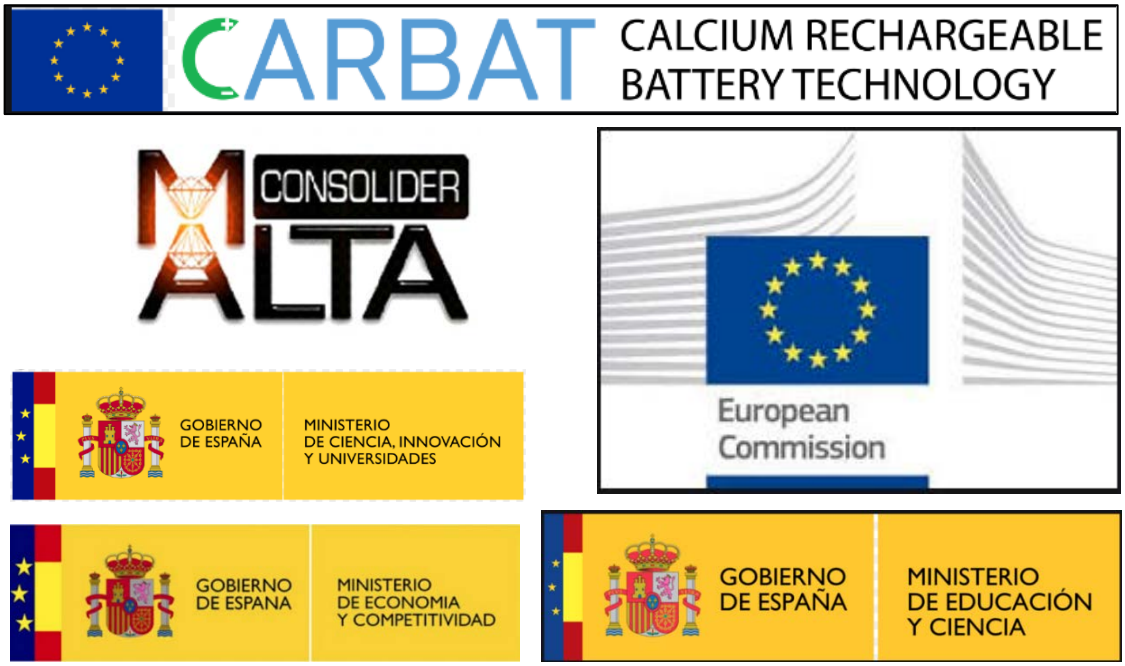

ÍNDICE

RESUMEN

Actualmente las baterías recargables de ion-litio se utilizan en multitud de dispositivos electrónicos, en vehículos eléctricos y se presentan como una alternativa en el desarrollo de sistemas de almacenamiento integrados en la red eléctrica. A pesar de su buen resultado, el desarrollo de baterías recargables más livianas, baratas, estables, basadas en elementos abundantes y no tóxicos, y que proporcionen una mayor densidad de energía, es una necesidad urgente social, económica y medioambiental. Entre las tecnologías emergentes se han propuesto baterías recargables que utilicen como electrodo negativo elementos metálicos más abundantes que el litio y que funcionarían mediante la inserción reversible de los correspondientes iones metálicos en el electrodo positivo (Na, K, Mg, Ca, Al). El calcio es un candidato atractivo debido a su bajo coste, abundancia natural y potencial de reducción relativamente bajo. La posibilidad de desarrollar las baterías recargables de calcio se ha visto impulsada por recientes avances en electrolitos no acuosos compatibles con el depósito y pelado reversible de un ánodo de Ca metálico. Para el desarrollo de estas baterías es imprescindible encontrar materiales capaces de actuar como electrodo positivo, en los que los iones calcio puedan ser reversiblemente intercalados, y que deben además cumplir una serie de requisitos de cara a que la batería proporcione buenas prestaciones.

Hasta la fecha algunos materiales han sido estudiados como electrodo positivo en baterías recargables de calcio experimental y computacionalmente. De estos estudios se desprende que la baja movilidad del ion Ca^{2+} en las estructuras cristalinas es la mayor dificultad para el desarrollo de materiales capaces de actuar como cátodo. En esta Tesis se aborda la búsqueda de materiales de electrodo positivo mediante el uso de técnicas computacionales, en concreto de la metodología basada en la Teoría del Funcional de la Densidad (Density Functional Theory, DFT). Para los materiales estudiados (de forma genérica Ca_xHost), se considera la reacción de intercalación de Ca:

$$(x_2\text{-}x_1)\ Ca(s) + Ca_{x1}Host \rightarrow Ca_{x2}Host$$

Las propiedades evaluadas a partir de los cálculos DFT han sido fundamentalmente tres:

- La variación de volumen asociada a la reacción de inserción, propiedad ligada a la capacidad específica que podría desarrollar el material como electrodo positivo.
- El voltaje de intercalación del Ca, propiedad que junto con la capacidad específica determina la energía especifica suministrada por el material de electrodo.

- La movilidad de los iones Ca^{2+} en los materiales Ca_xHost, para lo que se ha determinado la energía de activación (Ea) de un mecanismo de difusión tipo hopping. Esta propiedad está relacionada con la potencia de la batería; una baja movilidad (Ea > 1 eV) descarta la aplicabilidad del material.

Con respecto a los materiales estudiados, puesto que una de las ventajas del calcio es su abundancia en la corteza terrestre, se han investigado las reacciones de desintercalación de Ca de minerales. El calcio se encuentra en la corteza terrestre formando parte de diversos minerales, combinándose en alguno de ellos con metales de transición. Entre estos últimos, se han evaluado como electrodo positivo minerales pertenecientes a los grupos del olivino ($CaFeSiO_4$; kirschsteinita), piroxenos ($CaFe/MnSi_2O_6$; hedenbergita y johannsenita, respectivamente), granates ($Ca_3Fe/Cr_2Si_3O_{12}$; andradita y uvarovita, respectivamente), anfíboles ($Ca_2Fe_5Si_8O_{22}(OH)_2$; ferroactinolita) y carbonatos dobles ($CaMn(CO_3)_2$; kutnahorita). Los resultados indican que algunos de estos minerales podrían proporcionar altas energías específicas (desde 780 hasta 1500 Wh/kg) con variaciones estructurales moderadas (variación de volumen ~ 15%). No obstante las barreras energéticas asociadas a la difusión del Ca (> 2eV) descartan su aplicación como electrodos.

Un segundo grupo de materiales lo constituyen los óxidos de metales de transición $CaFeO_{2.5}$, $CaMnO_{2.5}$ y $CaMn_4O_8$, que tienen la característica común de presentar estructuras cristalinas tridimensionales con vacantes de iones óxido o Ca^{2+}. Como resultado más relevante, se ha encontrado que en la browmillerita-$CaFeO_{2.5}$ la presencia de vacantes óxido genera caminos de difusión que minimizan las repulsiones electrostáticas entre el ion Ca que difunde y los cationes Fe^{3+} de la red cristalina. Como consecuencia, la energía de activación calculada (Ea = 1 eV) es sustancialmente menor que en el material sin vacantes (perovskita, Ea ~ 2 eV).

Continuando con la dimensionalIdad de las estructuras cristalinas, se aborda el estudio de tres óxidos de Co con distinta dimensionalidad: 3D-$CaCoO_{2.5}$ (estructura tipo pervoskita), 2D- $Ca_3Co_4O_9$ (que presenta una estructura desajustada *misfit*) y 1D-$Ca_3Co_2O_6$ (estructura tipo K_4CdCl_6). Para los tres compuestos la potencial actividad redox se asociaría al par Co^{4+}/Co^{3+}. Los resultados indican que mientras que los tres materiales ofrecen buenos valores de voltaje de intercalación (3-4 V), capacidad específica (160-190 mAh/g) y variación del volumen (< 8%), la difusión del Ca^{2+} está favorecida en las estructuras de baja dimensionalidad (Ea = 0.9 eV). Un estudio más detallado de las fases $Ca_{3-x}Co_2O_6$ sugiere una

posible transformación irreversible de $Ca_3Co_2O_6$ al desinsertarse los iones calcio de su estructura.

Finalmente, dada la abundancia, baja toxicidad y alto potencial de los pares redox Fe^{3+}/Fe^{2+} y Fe^{4+}/Fe^{3+}, se ha estudiado la familia $CaFe_{2+n}O_{4+n}$ ($0 < n < 3$). El término n =1/4 reúne las características más prometedoras: capacidad específica de 230 mAh/g, voltaje de 4.16 V y energía de activación para la difusión de Ca^{2+} 0.72 eV (la más baja reportada para óxidos hasta la fecha). Dado el potencial interés de este material, se presentan los resultados de la investigación paralela experimental realizada en el Instituto de Ciencia de Materiales de Barcelona-CSIC.

ABSTRACT

The Li-ion technology currently dominates the rechargeable battery market for portable electronics and appears to be a possible near term solution for applications such as electric vehicles and grid storage. While the current state-of-the-art in rechargeable batteries is the Li-ion technology, research efforts are being intensified towards the development of alternative technologies to satisfy the ever-increasing demand for enhanced energy density and lower costs. This prompted the development of rechargeable batteries based on the more abundant and cheaper Na, K, Ca, Mg and Al metals. Rechargeable batteries based on a Ca-metal anode are attractive given the abundance of calcium in the Earth's crust, the high capacity of calcium anodes (1340 mAh/g) and its negative reduction potential (only 170 mV above that of lithium metal). Under the perspective of high specific energies (exceeding 600 mWh/g positive electrode material), researchers from various disciplines have joined endeavors in the quest of suitable electrode and electrolytes for the emerging Ca technology. Recent findings demonstrate the feasibility of the reversible calcium plate and stripping using different non-aqueous electrolytes with a large voltage stability window. The identification of suitable cathode materials, able to reversibly intercalate Ca ions and with appealing electrode characteristics, is a must in the development of this emerging technology.

Previous computational an experimental investigations in some materials pointed to the low mobility of Ca^{2+} ions in inorganic structures as the major handicap in the cathode design for cathode design. In this Thesis computational techniques, based on the DFT method, have been used to quickly screen a variety of materials to identify those with potential application as positive electrode for rechargeable Ca batteries. For the materials under investigation (denoted as Ca_xHost), the intercalation reaction can be expressed as:

$$(x_2\text{-}x_1)\ Ca(s) + Ca_{x1}Host \rightarrow Ca_{x2}Host$$

The materials are evaluated through the computation of the following properties:

- volume changes associated to the intercalation reaction, a parameter linked to the maximum specific capacity deliverable by the electrode material
- intercalation voltages, which together with the specific capacity determine the specific energy
- mobility of Ca^{2+} ions. The migration energy barriers (Ea), which can be extracted from DFT calculations for a simple hopping mechanism, provide an approximate estimate

of the ionic diffusivity. Energy barriers exceeding 1 eV disregard the application of a material as cathode for Ca cells.

A first group on materials focuses on Ca-bearing minerals because they represent stable and abundant compounds. Suitable minerals should contain a transition metal able of being reversibly reduced and oxidized, which points to several major classes of silicates and carbonates: olivine ($CaFeSiO_4$; kirschsteinite), pyroxene ($CaFe/MnSi_2O_6$; hedenbergite and johannsenite, respectively), garnet ($Ca_3Fe/Cr_2Si_3O_{12}$; andradite and uvarovite, respectively), amphibole ($Ca_2Fe_5Si_8O_{22}(OH)_2$; ferroactinolite) and double carbonates ($CaMn(CO_3)_2$; kutnahorite and $CaFe(CO_3)_2$; ankerite). The results indicate that upon Ca deintercalation, compounds such as pyroxene, garnet and double carbonate minerals could display high theoretical energy densities (ranging from 780 to 1500 mWh/g) with moderate structural modifications. As a downside, DFT calculations indicate a hampered Ca mobility in their crystal structures. The overall analysis then disregards olivine, garnet, pyroxene, amphibole and double carbonates as structural types for future Ca-cathode materials design.

Transition metal oxides are interesting candidates due to their theoretical high energy densities, but with the drawback of a low Ca^{2+} mobility. Previous computational/experimental investigations associate the electrochemical inactivity of various oxides ($CaMO_3$-perovskite, $CaMn_2O_4$-post-spinel and CaV_2O_5) to high energy barriers for Ca migration. The introduction of oxygen and/or Ca vacancies in ternary transition metal oxides is a likely way to reshape the local topology and hence improve the Ca diffusivity. In this work, the energy barriers for Ca migration are calculated and discussed for (i) oxygen-deficient perovskites within the related $Ca_2Fe_2O_5$-brownmillerite and $Ca_2Mn_2O_5$ structures, and (ii) tunnel $CaMn_4O_8$, a derivative of the $CaMn_2O_4$-marokite with Ca vacancies. The DFT results evidence that for some of these oxidized/reduced oxides the Ca mobility is equally hampered than in the parent oxides (i.e., $CaMn_4O_8$ or $Ca_2Mn_2O_5$), due to the occurrence of Ca sites with small triangular faces. A second key factor is to forestall the face sharing between the TM polyhedra and the Ca intermediate site. DFT results reveal that this can be accomplished in some reduced oxides (i.e. $Ca_2Fe_2O_5$ versus $CaFeO_3$).

The investigation of transition metal oxides pursued with the evaluation of the electrode characteristics of three ternary calcium cobalt oxides with distinct dimensionality: 3D-$Ca_2Co_2O_5$ (brownmillerite type structure), 2D-$Ca_3Co_4O_9$ (a misfit compound) and 1D-$Ca_3Co_2O_6$ (K_4CdCl_6 structural type). For the three compounds, calculations predict Co^{4+}/Co^{3+} voltages in the 3–4 V range, with a volume variation below 8% upon Ca deinsertion. Further

Co^{4+} oxidation is predicted at too high voltages not reachable in practice. The maximum specific capacities are therefore 192 mAh/g ($Ca_2Co_2O_5$), 165 mAh/g ($Ca_3Co_4O_9$) and 160 mAh/g ($Ca_3Co_2O_6$). With energy barriers for Ca diffusion of 0.9 eV, the 2D and 1D oxides are appealing as low rate cathode materials. To complete a previous experimental investigation, we have analyzed the reversibility of the Ca deintercalation reaction of 1D-$Ca_3Co_2O_6$. It is found that a phase transformation takes place upon decalciation driven by the change in the electronic configuration of Co ions (from High Spin-trigonal prismatic Co^{3+} to octahedral Low Spin-Co^{4+}) and involving the Ca diffusion pathways.

Sustainable cathode materials should include abundant and non-toxic elements, and at the same time, comply with the high energy density requirements. These criteria prompted the investigation of the $CaFe_{2+n}O_{4+n}$ ($0 < n < 3$) family, for which both the average intercalation voltage and the theoretical specific capacity decrease with the increasing n value. The term n = 1/4, $Ca_4Fe_9O_{17}$, meets the most appealing characteristics: a calculated average voltage of 4.16 V, a theoretical specific capacity of 230 mAh/g and the lowest energy barrier for Ca migration so far predicted for an existing oxide (0.72 eV). The computational study of $Ca_4Fe_9O_{17}$ is combined with the experimental investigation carried out in the Instituto de Ciencia de Materiales de Barcelona-CSIC.

CAPÍTULO 1

INTRODUCCIÓN

1.1. BATERÍAS RECARGABLES DE CALCIO

El uso de la energía ha acompañado a los seres humanos desde la más remota antigüedad. A lo largo de la historia, las necesidades de la sociedad han impulsado la búsqueda de nuevas fuentes de energía, hasta llegar al siglo XX con una amplia gama de materiales y procesos diseñados o descubiertos con este fin. En las últimas décadas, el consumo exponencialmente creciente de combustibles fósiles (carbón, petróleo y gas natural) ha desencadenado graves problemas medioambientales como el calentamiento global, junto con problemas de sostenibilidad debidos al previsible agotamiento de las fuentes energéticas tradicionales. Por tanto, la comunidad científica ha de restringir la búsqueda de nuevas fuentes de energía hacia procesos y materiales susceptibles de renovarse y medioambientalmente benignos. En paralelo al desarrollo de fuentes de energía renovable, surge la necesidad de almacenar la energía generada siguiendo los mismos principios de conservación medioambiental y sostenibilidad [1-3] .

Los sistemas de almacenamiento de energía pueden clasificarse atendiendo a la forma que adopta la energía almacenada: mecánica, térmica, termoquímica, química, eléctrica, o electroquímica [4, 5] (figura 1.1). Dentro de esta última categoría se encuentran las baterías recargables, cuya andadura se inició en 1859 con la invención de la batería de plomo-ácido por Gaston Planté [6]. La búsqueda de baterías recargables, más ligeras, seguras y con mayor densidad energética dio como resultado en 1985 el primer prototipo de una batería recargable de ion-litio [7, 8].

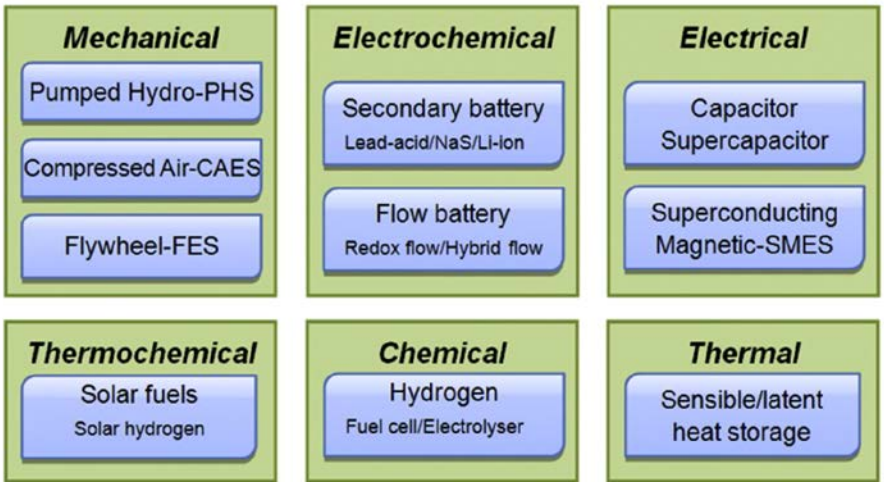

Figura 1.1. Clasificación de sistemas de almacenamiento de energía [4].

Hoy en día las baterías recargables de ion-litio se utilizan en multitud de dispositivos electrónicos, en vehículos eléctricos y son una alternativa fundamental en el desarrollo de sistemas de almacenamiento integrados en la red eléctrica [9-11]. A pesar del buen resultado de las baterías de ion-litio, la búsqueda de baterías recargables más livianas, baratas, estables y que proporcionen una mayor densidad de energía, ya es una necesidad urgente social, económica y medioambiental [12] . En los últimos años, las preocupaciones sobre la disponibilidad del litio, níquel y cobalto presentes en las baterías de alta densidad energética comercializadas de ion-litio, han llevado a la búsqueda de distintas alternativas (figura 1.2). Entre las tecnologías emergentes se han propuesto baterías recargables que utilicen como electrodo negativo elementos metálicos más abundantes que el litio y que funcionarían mediante la inserción reversible de los correspondientes iones metálicos en el electrodo positivo (figura 1.3) [13-15].

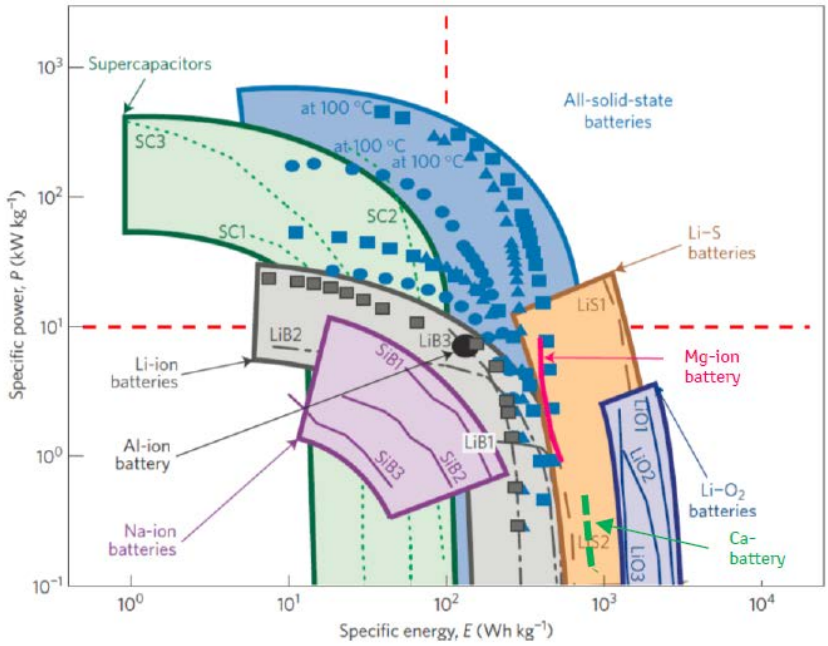

Figura 1.2. Densidad energética y densidad de potencia esperadas para algunos sistemas electroquímicos de almacenamiento de energía recargables. Adaptado de [16]. Se muestran las expectativas para baterías recargables basadas en reacciones de intercalación de iones metálicos Al^{3+}, Li^{+}, Na^{+}, Mg^{2+} y Ca^{2+}.

El funcionamiento de este tipo de baterías se muestra en la figura 1.3 tomando como ejemplo el uso de Ca metálico como electrodo negativo. Durante la etapa de descarga de la batería los electrones circulan desde el electrodo negativo (Ca metal) hasta el electrodo positivo (material anfitrión), y los iones Ca^{2+} se desplazan desde el electrodo negativo al electrodo positivo a través del electrolito. Así, los iones Ca^{2+} se insertan en el

electrodo positivo y los electrones se incorporan en su estructura de bandas (reducción del electrodo positivo). Esta reacción de inserción es espontánea, por lo que la etapa de descarga proporciona energía. En las baterías secundarias, durante el proceso de carga se producen la reacciones inversas; los electrones circulan desde el electrodo positivo al electrodo negativo (oxidación del electrodo positivo), y los iones calcio se desinsertan del electrodo positivo para migrar a través del electrolito hacia el electrodo negativo. La reacción que tiene lugar no es espontánea y, por tanto, requiere un aporte de energía.

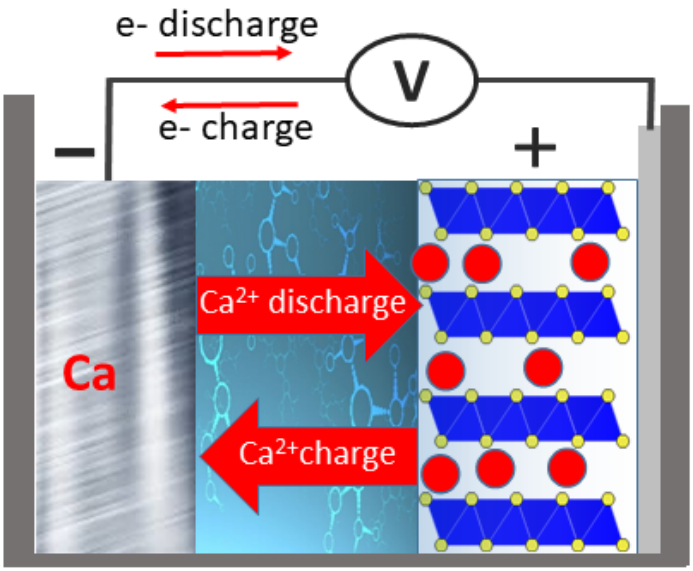

Figura 1.3. Esquema de una batería recargable de calcio mostrando el funcionamiento durante las etapas de descarga (inserción de Ca^{2+} en el electrodo positivo) y carga (depósito de Ca^{2+} en el electrodo negativo, que en este caso está formado por Ca metálico) [17].

En la figura 1.3. la batería esquematizada utiliza Ca metal como electrodo negativo y un compuesto genérico Ca_{x1}-Host como electrodo positivo, por lo que la reacción global de la batería se expresaría:

$$(x_2\text{-}x_1)\ Ca(s) + Ca_{x1}Host \leftrightarrow Ca_{x2}Host \qquad (1.1)$$

Entre las distintas tecnologías propuestas según la naturaleza del ion intercalado (M^{n+}), las baterías basadas en portadores de carga multivalentes (Mg^{2+}, Ca^{2+}, Al^{3+}) pueden exhibir ventajas en términos de densidad de energía, ya que para una cierta cantidad de portadores de carga, la capacidad se duplica (n = 2) o se triplica (n = 3) en comparación con los portadores monovalentes como Li^+ o Na^+ [13, 18-20]. El calcio es un candidato atractivo debido a su bajo coste, abundancia natural y potencial de reducción

relativamente bajo. Por otro lado, como se desprende de la figura 1.4, el calcio metálico tiene un enorme interés ya que posee capacidades volumétricas más altas que el litio metálico (3073 mAh cm^{-3} frente a 2061 mAh cm^{-3} para el litio) con un potencial redox muy similar (−2.9 V en comparación con −3.0 V para Li vs NHE). Finalmente, una de las principales ventajas del Ca es que los procesos electroquímicos relacionados con su recubrimiento/pelado ocurren de forma reversible sin formación de dendritas, lo que alivia las preocupaciones de seguridad relacionadas con su uso como electrodo negativo en las baterías [21].

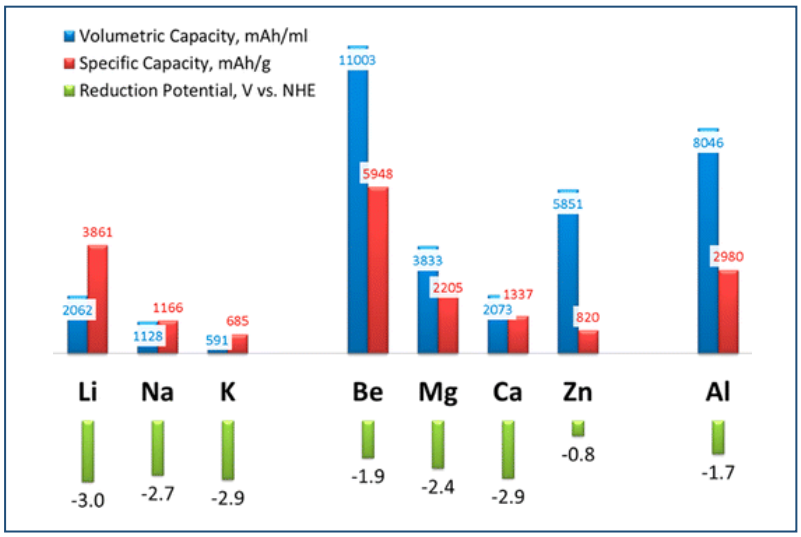

Figura 1.4. Características de algunos metales propuestos para baterías secundarias [13].

El uso del calcio en baterías no es nuevo (figura 1.5), datando su primera utilización de 1935 [22], concretamente como aditivo en baterías de ácido-plomo. Las décadas siguientes se centraron en su uso como ánodo en baterías primarias (véase [17] y sus referencias). El desarrollo de baterías secundarias requiere que el Ca metal pueda ser reversiblemente pelado y depositado. Con este objetivo, en torno al año 1990 se iniciaron diversos estudios utilizando electrolitos orgánicos [23], y que ha culminado recientemente, en el desarrollo de dos electrolitos (ambos disoluciones de $Ca[B(hfip)_4]_2$ en DME) que permiten depositar calcio reversiblemente a temperatura ambiente y con una estabilidad anódica de 4 V [24, 25]. Aunque aún queda mucho trabajo por hacer en cuanto a la optimización del electrolito, del ánodo de Ca y de las interfases [17], estos avances permiten plantear la posibilidad de una batería recargable de Ca. Para ello, es imprescindible encontrar materiales de electrodo positivo.

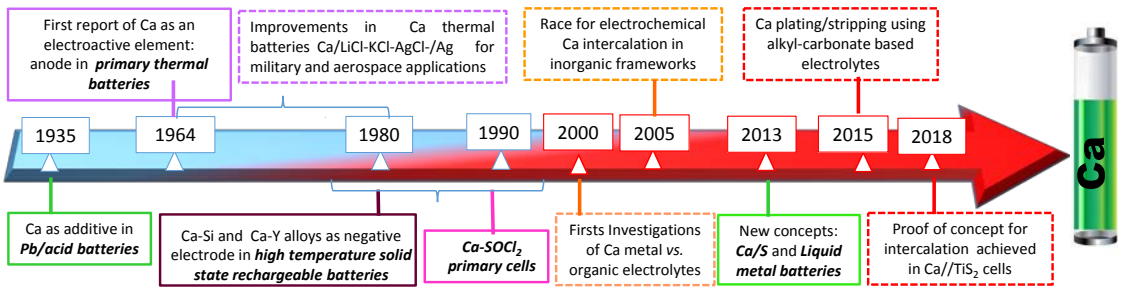

Figura 1.5. Eje cronológico de la utilización del calcio en baterías [17].

1.2. MATERIALES COMO ELECTRODO POSITIVO PARA BATERÍAS RECARGABLES DE CALCIO

El desarrollo de baterías secundarias basadas en reacciones de intercalación de calcio abre la necesidad de buscar materiales útiles como electrodo positivo, y que deben cumplir una serie de requisitos de cara a que la batería proporcione buenas prestaciones [7, 11, 26]. En esta sección se revisan brevemente los parámetros asociados a las prestaciones de las baterías recargables para, a continuación, exponer los requisitos que deben cumplir los materiales de electrodo positivo. Finalmente se presenta el estado del arte en la búsqueda de materiales capaces de actuar como electrodo positivo en baterías recargables de calcio.

1.2.1. Parámetros de la batería

Una de las magnitudes más importantes para determinar el interés tecnológico de una batería es la diferencia de potencial entre sus electrodos (V, o voltaje) ya que mide la tendencia que presenta el sistema a que se produzca el proceso electroquímico. El potencial está relacionado con la variación de energía libre del proceso (ΔG) a través de la expresión:

$$\Delta G = -nzFV \qquad (1.2)$$

donde n es el número de moles de especie activa que participa en la reacción, z el número de electrones transferidos por átomo y F la constante de Faraday, 96485 C mol^{-1}. La anterior ecuación es sólo estrictamente cierta cuando no circula corriente a través de la célula. Generalmente, debido a efectos irreversibles de polarización de los electrodos y de

resistencia interna, se producen ciertas pérdidas de energía. Por eso el valor de ΔG indica el máximo trabajo que se podría obtener del sistema.

Otro de los parámetros característicos en baterías es la capacidad específica (C_e, mAh/g), que da una idea de la cantidad de electrones (o de electricidad) que circulan por el circuito externo durante la reacción electroquímica. Se calcula según:

$$C_e = nzF / W \quad (1.3)$$

donde *n* es el número de moles de la especie huésped (Ca^{2+} en nuestro caso) que participan en la reacción, z en el número de electrones transferidos por átomo interclado (2 por cada mol de Ca^{2+}) y W el peso fórmula del compuesto anfitrión (Ca_{x1}Host) donde se intercala la especie huésped. Para calcular la energía específica almacenable por la célula (E_e) basta con multiplicar la capacidad específica por el voltaje de salida.

$$E_e=VC_e \quad (1.3)$$

Por lo tanto, la densidad energética por masa de electrodo (mWh/g) se maximiza con el voltaje de operación y la capacidad específica. La figura 1.2 muestra los rangos de energía específica obtenidos con varias tecnologías y su relación con la densidad de potencia de la batería (mWh/g). Esta última informa sobre la velocidad con la que se accede a la energía suministrada por la batería. Dependiendo de la aplicación, pueden utilizarse baterías que combinen mayor/menor energía/potencia. Por ejemplo, en un vehículo eléctrico la densidad energética determina la autonomía del coche, y la densidad de potencia el tiempo de aceleración necesario para un determinado incremento de la velocidad [7].

En el caso de baterías secundarias resulta de gran importancia la vida media, que se refiere al número total de ciclos carga-descarga que se pueden repetir antes de observar una degradación en los valores de los parámetros comentados anteriormente. Para cualquier tecnología de baterías, las medidas de su rendimiento (capacidad específica, densidad de energía, vida media, densidad de potencia) están relacionadas con las propiedades intrínsecas de los materiales que forman los electrodos positivo y negativo. Otras características de la batería serían el proceso de reciclaje, el coste económico, la posibilidad de un segundo uso, etc; consideraciones medioambientales y económicas que son de extremada importancia.

1.2.2. Requisitos del electrodo positivo

Los requisitos que debe presentar un material para actuar como electrodo positivo comienzan por aquellos que permiten intercalar los iones metálicos (Ca^{2+} en este caso) en su estructura [26-28]. Para actuar como material anfitrión en una reacción de intercalación los materiales deben poseer una estructura abierta con huecos interconectados capaces de albergar a la especie huésped (Ca^{2+}) y permitir su difusión, alta conductividad electrónica y centros redox capaz de oxidarse/reducirse. Habrá materiales que puedan intercalar iones Ca^{2+}, pero que no sean útiles como electrodo positivo por no proporcionar parámetros adecuados para la batería. La relación entre los parámetros de la batería y las propiedades intrínsecas del material de intercalación (figura 1.6) puede resumirse en una serie de consideraciones básicas [26, 28].

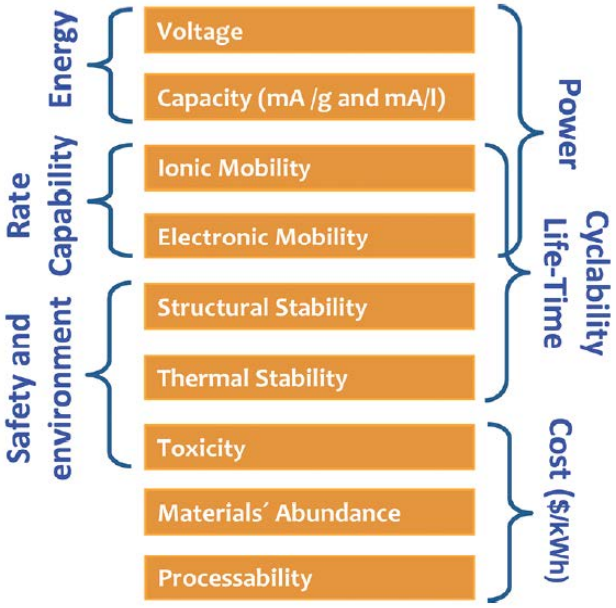

Figura 1.6. Propiedades intrínsecas de los materiales de los electrodos en relación con los parámetros de la batería [29].

Una alta capacidad específica (ecuación 1.2) requiere que el material de electrodo sea ligero y capaz de albergar una elevada concentración de Ca en su interior. Es decir, la capacidad específica dependerá tanto de la composición como de la estructura cristalina del material. El requisito del bajo peso-fórmula limita la composición, así los materiales de electrodos deben contener preferiblemente elementos ligeros. La reacción de intercalación solo debe causar cambios limitados en la estructura cristalina del material

anfitrión para asegurar la reversibilidad de proceso y la retención de la capacidad específica durante la vida de la batería.

Para tener el potencial más alto posible, hay que prestar especial atención a los materiales que se van a usar tanto de ánodo como de cátodo, tratando de que el primero tenga el potencial más bajo posible y el segundo el más alto. El electrodo positivo es Ca metal, y el electrodo positivo debe tener un potencial alto, pero dentro de los límites de estabilidad del electrolito utilizado. El potencial de operación del cátodo está mayoritariamente gobernado por la naturaleza del centro redox (típicamente un elemento de metal de transición), y en menor medida por la estructura cristalina. Se preferirán los compuestos que contienen metales de transición abundantes, ligeros, no tóxicos y que exhiben potenciales redox adecuados para ser utilizados como materiales de electrodo positivos (Mn, Fe). Para un mismo par redox, el potencial depende de la naturaleza de los aniones, pasando de voltajes más bajos en sulfuros a voltajes más altos en óxidos y en estructuras basadas en polianiones como silicato y fosfato [11, 30].

La conductividad electrónica y la difusión de Ca en el material determinan la potencia de la batería. En las baterías recargables multivalentes, la alta potencia requiere que la difusión de Mg, Ca o Al dentro y fuera de los materiales del electrodo tenga lugar lo suficientemente rápido como para suministrar la corriente eléctrica. No hay duda de que el diseño de ingeniería del electrodo (porosidad, tamaño de grano y partícula, cristalinidad…) es un factor importante para el rendimiento de alta potencia. Sin embargo, la difusión de cationes en el material activo es una propiedad intrínseca del material del electrodo y es una condición necesaria para un rendimiento de alta velocidad.

En términos generales, puede decirse que otros parámetros como la vida media y la seguridad de la batería dependen de la naturaleza y estabilidad de los materiales del electrodo, pero también de los electrolitos y de las interfaces electrodo / electrolito.

1.2.3. Materiales probados como electrodo positivo en celdas de calcio

Hasta la fecha, distintos grupos de investigación han abordado la investigación de algunos materiales como posibles electrodos de baterías de calcio. Los materiales estudiados, junto con un resumen del comportamiento observado, se recogen en la tabla 1.1. Una comparativa más extensa de las condiciones experimentales utilizadas para estudiar cada material puede encontrarse en un artículo de revisión reciente [17]. Desde las primeras

investigaciones en V_2O_5 [31], pasando por diversos óxidos de Mn [32, 33] y Co [34, 35], hasta algunas composiciones más exóticas (como $CaTaN_2$ [36]) puede decirse que hasta el momento no se ha encontrado un material con aplicabilidad como electrodo positivo en baterías de Ca recargables. Es más, para muchos de los compuestos estudiados, incluso la intercalación reversible de Ca está pendiente de confirmación, ya que la señal electroquímica observada podría ser concomitante a la inserción de protones y/o de reacciones de descomposición del electrolito [35, 37, 38]. Así mismo, en la mayoría de los materiales que parecen insertar o desinsertar Ca debe mejorarse la caracterización de los productos intercalados/desintercalados para establecer los mecanismos de la reacción y demostrar su reversibilidad.

TABLA 1.1. Compuestos inorgánicos probados como electrodo positivo en celdas de Ca con configuración de dos o tres electrodos.

Compuesto	Resultado
CaV_2O_5 [38], $CaMoO_3$[39], $CaMn_2O_4$[33]	Inactividad del material de electrodo positivo. La respuesta electroquímica se debe a reacciones colaterales del electrolito
$NH_4V_4O_{10}$ [40], $Ca_{0.5}Co_2O_4$ [34], V_2O_5 [31, 41] [38, 42-44], MoO_3 [45] [46] $K_{0.31}MnO_2.0.25H_2O$ (birnessite) [32] $Mg_{0.19}Na_{0.07}MnO_2$ 0.37 H_2O (todorokite) [47], $K_2BaFe(CN)_6$ [48], $Na_{0.2}MnFe(CN)_6$ [49], $KNiFe(CN)_6$ [50], $NaFePO_4F$ [51], Mo_6Se_8 [52]	Posible actividad del material de electrodo positivo. Se requiere caracterización adicional para elucidar el mecanismo: intercalación/desintercalación de Ca, reacciones colaterales del electrolito, inserción de H^+
$Ca_3Co_2O_6$ [35]	Desinserción de 1 mol de Ca. Proceso irreversible
$CaTaN_2$ [36]	Descompone al oxidarse (posible desinserción de Ca)
TiS_2 [37] [53]	Intercalación reversible de 0.2 moles de Li. Extensiva reacción colateral del electrolito. Formación de fases intermedias metaestables.

Entre los materiales estudiados, quizás los resultados más completos y prometedores se refieren a TiS_2. Para este compuesto laminar (figura 1.7) se ha realizado una caracterización lo suficientemente exhaustiva como para confirmar la intercalación reversible de 0.2 moles de Ca por fórmula unidad, lo que corresponde a una capacidad específica de ~50 mAh/g [37]. La intercalación ocurre a un potencial en torno a 1.2 V vs Ca^{2+}/Ca, resultando en una energía específica de ~80 mWh/g. A pesar de que estos valores están muy lejos de los máximos teóricos (C = 240 mAh/g , E = 408 mWh/g, tomando el

potencial de 1.7 V para el par Ti^{+4}/Ti^{+3} calculado en [54]), los resultados son prometedores, y el uso de TiS_2 como electrodo para baterías de calcio fue patentado en 2018 [54]. Estudios más recientes, utilizando diversos electrolitos, parecen apoyar la posibilidad de usar este material como electrodo, si bien las prestaciones siguen siendo muy mejorables [55].

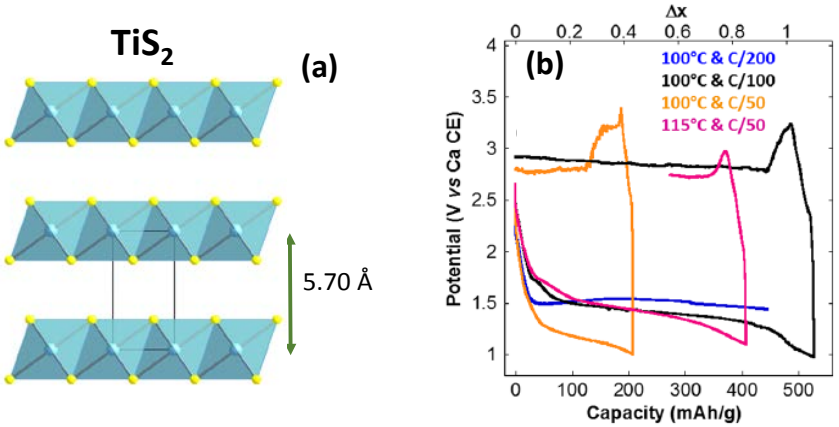

Figura 1.7. (a) Estructura cristalina de TiS_2, mostrando el espacio interlaminar disponible para la intercalación de calcio. (b) Primer ciclo descarga/carga de celdas $Ca/Ca(BF_4)$ en EC:PC/TiS_2 a distintas intensidades de corriente y temperaturas [37].

En conjunto, el estudio de materiales como electrodo para baterías de Ca realizado por diversos investigadores pone de manifiesto dos necesidades acuciantes. Por un lado, deben mejorarse los protocolos experimentales que atañen al diseño y componentes de las celdas de medida (dos *vs* tres electrodos, electrodo negativo, electrolitos, interfaces [17, 56]) y, por el otro, es imprescindible profundizar en el uso de técnicas de caracterización que permitan determinar la naturaleza y el mecanismo de las reacciones que ocurren en el electrodo positivo. En espera de estos avances experimentales, la búsqueda de materiales de electrodo positivo puede hacer uso de técnicas computacionales.

Existen múltiples técnicas computacionales que permiten simular distintos sistemas (moleculares, fluidos, sólidos, o incluso dispositivos) a escala macroscópica y/o microscópica. Para estudiar los materiales de intercalación a nivel “atómico”, se puede utilizar la metodología químico-cuántica denominada Teoría del Funcional de la Densidad (*Density Functional Theory*, DFT en la literatura inglesa). Los fundamentos de esta metodología de cálculo se exponen brevemente en el capítulo de metodología de esta

Tesis. A continuación, revisamos su aplicación en la investigación de los materiales de electrodo.

1.3. DFT Y LA BÚSQUEDA DE MATERIALES DE ELECTRODO

La búsqueda, o el diseño, de materiales de electrodo suele basarse en el "mapeo" de las relaciones composición-estructura-propiedad en diferentes familias de materiales. En las últimas tres décadas se ha adquirido un sólido conocimiento de dicha relación para los materiales de intercalación de iones de litio [11, 26, 29]. Sin embargo, se sabe poco sobre la química de intercalación de portadores multivalentes (Ca^{2+}, Mg^{2+}, Al^{3+}), si bien, es asumible que dada la distinta naturaleza de estos cationes, su química de intercalación debe diferir sustancialmente de la de Li. Por lo tanto, la búsqueda de materiales de Ca no puede realizarse tomando como partida los materiales de Li; aunque algunos materiales capaces de actuar como electrodo en baterías de Li pueden ser útiles también como electrodo de Ca (ej., TiS_2), otros deben descartarse completamente (ej., $LiFePO_4$) [17]. Descartada la selección de materiales por analogía con la química de intercalación del Li, la búsqueda de electrodos para baterías de Ca puede tomar como punto de partida un amplio cribado y mapeo de materiales. La selección y el mapeo de las relaciones composición-estructura-propiedades basadas en procedimientos experimentales que implican protocolos típicos de síntesis, caracterización estructural y caracterización electroquímica consume tiempo y/o trabajo. Además, como se ha comentado en la sección anterior, en el caso del Ca, las pruebas electroquímicas son complicadas debido a las numerosas limitaciones técnicas y problemas existentes relacionados con la compatibilidad de los electrolitos o la fiabilidad de los electrodos negativos [17]. En este marco, los cálculos DFT son un buen punto de inicio para seleccionar materiales de electrodo.

En un cálculo DFT, se parte de una estructura cristalina donde los átomos están ordenados y tienen una disposición determinada, es decir, se establece qué átomo ocupa cada posición del entramado cristalino. De esta forma, controlando la composición y la estructura, es posible predecir y entender muchas propiedades intrínsecas de los materiales de los electrodos, incluidos los voltajes, la estabilidad de la estructura o la movilidad iónica [57-60]. Como se expondrá en la sección de Metodología, estos métodos se basan únicamente en las leyes básicas de la Física, como la mecánica cuántica y la mecánica estadística y, por lo tanto, no requieren ningún aporte experimental más allá de la naturaleza de los elementos constituyentes (y en algunos casos la estructura). Esto permite acelerar la búsqueda de materiales y el mapeo de la relación estructura-

composición-propiedades. La metodología seguida para el estudio de materiales de electrodo se expone en el Capítulo 2 de esta Tesis.

Los primeros estudios de DFT en materiales para baterías de calcio datan de 2015, y tratan de materiales tipo espinela, $Ca_T[M_2]_oO_4$ M = metal de transición, donde el Ca ocupa las posiciones tetraédricas (T) de la estructura [61]. Debe señalarse que estos materiales son "virtuales", es decir, hasta la fecha no se han sintetizado. Como puede verse en la figura 1.8, los valores esperados de energía específica (800-1000 mWh/g) superan los de la tecnología de litio (600 mWh/g). No obstante, estos estudios de DFT en espinelas y otros en V_2O_5, olivinos y delafossitas, revelan que la dificultad para intercalar Ca radica en la baja movilidad del mismo en las estructuras, la cual está controlada por la topología local alrededor del ion que difunde [62, 63]. Investigaciones posteriores en perovskitas $CaMO_3$ [39] y polimorfos $CaMn_2O_4$ [33] demuestran, mediante la combinación de experimentos y DFT, que la baja difusión de los iones Ca en las estructuras (barreras de difusión > 1.2 eV) resulta en ausencia de actividad electroquímica. Según estos autores, las altas barreras de difusión calculadas se deben al efecto combinado de (i) el tamaño del Ca^{2+} que impide su paso a través de los caminos de difusión, (ii) las repulsiones/atracciones electrostáticas que experimenta el Ca^{2+} que difunde con los cationes/aniones presentes en la estructura cristalina. A partir de resultados DFT, varios autores señalan que la movilidad del Ca, en general, está favorecida en calcogenuros (barreras de difusión < 0.8 eV) lo que puede asociarse a una menor repulsión electrostática [37, 64-66].

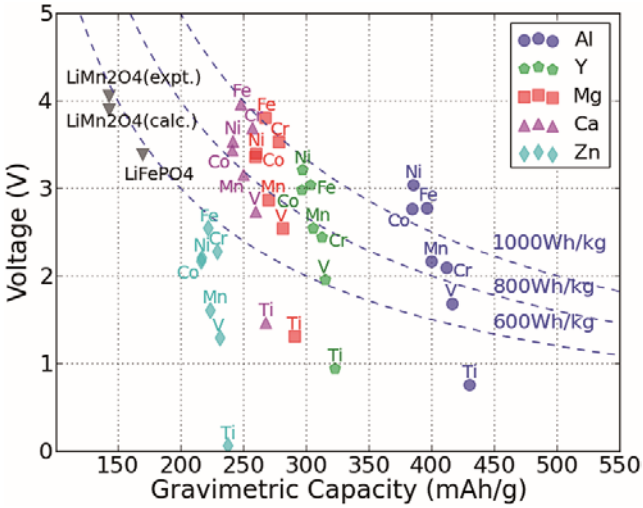

Figura 1.8. Voltaje calculado frente a capacidad específica para espinelas AM_2O_4 (A = Y, Al, Ca, Mg, Zn; M = Ti, V, Cr. Mn, Fe, Co, Ni). Tomada de [61]

Recientemente, Zhang y colaboradores [67] han realizado un cribado de materiales utilizando la base de datos Materials Project [68]. A partir de 4450 materiales iniciales -contenidos en la base de datos del Materials Project- los autores han seleccionado como más prometedores los recogidos en la tabla 1.2; puede comprobarse que las barreras de difusión son extremadamente altas, de acuerdo con las observaciones de los trabajos anteriores. No obstante, debe señalarse que en este trabajo la búsqueda de materiales está automatizada y se centra en una mera criba numérica a partir de los datos DFT calculados en el Materials Project.

Tabla 1.2. Materiales propuestos mediante un proceso de criba DFT [67].

Compuesto	Salto de banda	Capacidad Específica	Voltaje (V)	Cambio de volumen	Barerra difusión
Ti_4AlN_3	0.00	309	2.0	4.6	0.93
$Ca(BC)_2$	0.48	625	2.6	−7.9	2.19
$Ca(BeN)_2$	2.39	622	2.7	−19.7	1.47
$Ca(FeP)_2$	0.00	251	1.7	−12.8	3.68
$Ca(PRu)_2$	0.00	176	1.6	−10.1	3.53
Ca_2RuO_4	0.00	437	3.0	−10.1	1.49
Ca_2RuO_4	0.00	437	3.1	−5.3	1.56
$Ca_3(GaN_2)_2$	1.91	509	1.9	−15.0	0.82
$Ca_3Mn_2O_7$	0.48	470	3.1	16.7	1.76
$Ca_3Ru_2O_7$	0.00	370	2.8	−11.2	1.38
$Ca_4Mn_2O_7$	1.29	561	2.6	−6.4	1.60
$CaCu_2O_3$	0.00	249	3.4	−13.6	4.14
$CaMn_2O_4$	1.42	251	2.5	−4.1	2.22
$CaNb_2O_4$	1.28	185	2.8	−6.5	2.75
CaV_2O_5	1.89	241	2.5	−3.2	1.87
CaV_3O_7	2.44	176	2.5	−11.1	1.36
CaV_4O_9	2.49	138	2.6	−15.6	3.74

1.4. OBJETIVOS Y MATERIALES ESTUDIADOS

El objetivo final de este trabajo es encontrar materiales con utilidad como electrodo positivo para baterías recargables de calcio. Así mismo, teniendo en cuenta el escaso conocimiento de la química de intercalación del Ca, se plantea como objetivo paralelo ampliar el conocimiento fundamental de este tipo de reacciones, ahondando de manera sistemática en la relación entre estructura-composición-propiedades de electrodo de una serie de materiales. Para lanzar ambos objetivos (aplicado y fundamental), se realizarán cálculos DFT abordando los siguientes aspectos:

- Estudio de la variación de volumen asociada a la reacción de inserción
- Predicción de los voltajes de intercalación
- Estudio de la conductividad electrónica e iónica de los materiales

1.4.1. Materiales objeto del estudio

El calcio se encuentra en la corteza terrestre formando parte de diversos minerales principalmente sulfatos (como el yeso $CaSO_4 \cdot 2H_2O$) y carbonatos (como la calcita $CaCO_3$) .En el Capítulo 3 se evalúan como electrodo positivo minerales donde el calcio se combina con metales de transición y que pertenecen a los grupos del olivino ($CaFeSiO_4$; kirschsteinita), piroxenos ($CaFe/MnSi_2O_6$; hedenbergita y johannsenita, respectivamente), granates ($Ca_3Fe/Cr_2Si_3O_{12}$; andradita y uvarovita, respectivamente), anfíboles ($Ca_2Fe_5Si_8O_{22}(OH)_2$; ferroactinolita) y carbonatos dobles ($CaMn(CO_3)_2$; kutnahorita).

A partir de los óxidos estudiados con anterioridad a esta Tesis Doctoral (perovskitas $CaMO_3$ [39] y marokita-$CaMn_2O_4$ [33]) en este trabajo se plantea cómo afecta la presencia de vacantes de iones óxido o de iones calcio a las propiedades de electrodo. Para ello, en el Capítulo 4 se estudian los compuestos $CaFeO_{2.5}$, $CaMnO_{2.5}$ y $CaMn_4O_8$.

En el Capítulo 5 se aborda el estudio de tres óxidos de Co con distinta dimensionalidad: 3D-$CaCoO_{2.5}$, 2D- $Ca_3Co_4O_9$, y 1D-$Ca_3Co_2O_6$, asumiendo para todos ellos la desintercalación de Ca asociada al par redox Co^{4+}/Co^{3+}.

Finalmente, dada la abundancia, baja toxicidad y alto potencial de los pares redox Fe^{3+}/Fe^{2+} y $Fe4^{+}/Fe^{3+}$, en el Capítulo 6 se ha estudiado la familia $CaFe_{2+n}O_{4+n}$ ($0 < n < 3$). El

término n =0.25 reúne las características más interesantes, por lo que se ha realizado paralelamente la investigación experimental del material en el CSIC-Instituto de Ciencia de Materiales de Barcelona.

1.5. REFERENCIAS

[1] S. Chu, A. Majumdar, *Opportunities and challenges for a sustainable energy future*. Nature, 488 (**2012**) 294-303.

[2] N.S. Lewis, D.G. Nocera, *Powering the planet: Chemical challenges in solar energy utilization*. Proceedings of the National Academy of Sciences of the United States of America, 103 (**2006**) 15729-15735.

[3] M.S. Dresselhaus, I.L. Thomas, *Alternative energy technologies*. Nature, 414 (**2001**) 332-337.

[4] X. Luo, J. Wang, M. Dooner, J. Clarke, *Overview of current development in electrical energy storage technologies and the application potential in power system operation*. Applied Energy, 137 (**2015**) 511-536.

[5] H. Ibrahim, A. Ilinca, J. Perron, *Energy storage systems - characteristics and comparisons*. Renewable & Sustainable Energy Reviews, 12 (**2008**) 1221-1250.

[6] K.R. Bullock, *Lead-acid-batteries*. Journal of Power Sources, 51 (**1994**) 1-17.

[7] M. Broussely, Li-ion batteries for EV, HEV and other industrial applications, en Lithium batteries science and technology, Kluwer Academic Publishers 2004.

[8] K. Mizushima, P.C. Jones, P.J. Wiseman, J.B. Goodenough, *Li_xCoO_2 0 < x < 1 a new cathode material for batteries of high-energy density*. Materials Research Bulletin, 15 (**1980**) 783-789.

[9] B. Scrosati, J. Garche, *Lithium batteries: Status, prospects and future*. Journal of Power Sources, 195 (**2010**) 2419-2430.

[10] D. Larcher, J.M. Tarascon, *Towards greener and more sustainable batteries for electrical energy storage*. Nature Chemistry, 7 (**2015**) 19-29.

[11] J.B. Goodenough, K.-S. Park, *The Li-ion rechargeable battery: A perspective*. Journal of the American Chemical Society, 135 (**2013**) 1167-1176.

[12] B. Dunn, H. Kamath, J.-M. Tarascon, *Electrical energy storage for the grid: A battery of choices*. Science, 334 (**2011**) 928-935.

[13] J. Muldoon, C.B. Bucur, T. Gregory, *Quest for nonaqueous multivalent secondary batteries: Magnesium and beyond*. Chemical Reviews, 114 (**2014**) 11683-11720.

[14] M. Li, J. Lu, Z. Chen, K. Amine, *30 years of lithium-ion batteries*. Advanced Materials, 30 (**2018**) 1800561

[15] D. Kundu, E. Talaie, V. Duffort, L.F. Nazar, *The emerging chemistry of sodium ion batteries for electrochemical energy storage*. Angewandte Chemie-International Edition, 54 (**2015**) 3431-3448.

[16] Y. Kato, S. Hori, T. Saito, K. Suzuki, M. Hirayama, A. Mitsui, M. Yonemura, H. Iba, R. Kanno, *High-power all-solid-state batteries using sulfide superionic conductors*. Nature Energy, 1 (**2016**) 16030.

[17] M.E. Arroyo-de Dompablo, A. Ponrouch, P. Johansson, M.R. Palacin, *Achievements, challenges, and prospects of calcium batteries*. Chemical Reviews, (**2019**).

[18] T. Placke, R. Kloepsch, S. Duehnen, M. Winter, *Lithium ion, lithium metal, and alternative rechargeable battery technologies: The odyssey for high energy density*. Journal of Solid State Electrochemistry, 21 (**2017**) 1939-1964.

[19] P. Canepa, G.S. Gautam, D.C. Hannah, R. Malik, M. Liu, K.G. Gallagher, K.A. Persson, G. Ceder, *Odyssey of multivalent cathode materials: Open questions and future challenges*. Chemical Reviews, 117 (**2017**) 4287-4341.

[20] A. Ponrouch, C. Frontera, F. Barde, M.R. Palacin, *Towards a calcium-based rechargeable battery*. Nature Materials, 15 (**2016**) 169-172.

[21] D. Monti, A. Ponrouch, R.B. Araujo, F. Barde, P. Johansson, M.R. Palacin, *Multivalent batteries - prospects for high energy density: Ca batteries*. Frontiers in Chemistry, 7 (**2019**) 79.

[22] H.E. Haring, U.B. Thomas, *The electrochemical behavior of lead, lead-antimony and lead-calcium alloys in storage cells*. Transactions of The Electrochemical Society., 68 (**1935**) 293-307.

[23] D. Aurbach, R. Skaletsky, Y. Gofer, *The electrochemical-behavior of calcium electrodes in a few organic electrolytes*. Journal of the Electrochemical Society, 138 (**1991**) 3536-3545.

[24] Z. Li, O. Fuhr, M. Fichtner, Z. Zhao-Karger, *Towards stable and efficient electrolytes for room-temperature rechargeable calcium batteries*. Energy & Environmental Science, (**2019**) 3496-3501.

[25] A. Shyamsunder, L.E. Blanc, A. Assoud, L.F. Nazar, *Reversible calcium plating and stripping at room temperature using a borate salt*. ACS Energy Letters, 49 (**2019**) 2271-2276.

[26] A. Manthiram, Materials aspect: An overview, in Lithium batteries science and technology, Kluwer Academic Publishers 2004.

[27] D.W. Murphy, *Insertion reactions in electrode materials*. Solid State Ionics, 18-9 (**1986**) 847-851.

[28] M.S. Whittingham, *Chemistry of intercalation compounds - metal guests in chalcogenide hosts*. Progress in Solid State Chemistry, 12 (**1978**) 41-99.

[29] Y.S. Meng, M. Elena Arroyo-de Dompablo, *Recent advances in first principles computational research of cathode materials for lithium-ion batteries*. Accounts of Chemical Research, 46 (**2013**) 1171-1180.

[30] A.K. Padhi, K.S. Nanjundaswamy, C. Masquelier, J.B. Goodenough, *Mapping of transition metal redox energies in phosphates with nasicon structure by lithium intercalation*. Journal of the Electrochemical Society, 144 (**1997**) 2581-2586.

[31] G.G. Amatucci, F. Badway, A. Singhal, B. Beaudoin, G. Skandan, T. Bowmer, I. Plitza, N. Pereira, T. Chapman, R. Jaworski, *Investigation of yttrium and polyvalent ion intercalation into nanocrystalline vanadium oxide*. Journal of the Electrochemical Society, 148 (**2001**) A940-A950.

[32] J. Hyoung, J.W. Heo, S.-T. Hong, *Investigation of electrochemical calcium-ion energy storage mechanism in potassium birnessite*. Journal of Power Sources, 390 (**2018**) 127-133.

[33] M.E. Arroyo-de Dompablo, C. Krich, J. Nava-Avendano, N. Biskup, M. Rosa Palacin, F. Barde, *A joint computational and experimental evaluation of $CaMn_2O_4$ polymorphs as cathode materials for ca ion batteries*. Chemistry of Materials, 28 (**2016**) 6886-6893.

[34] M. Cabello, F. Nacimiento, J.R. González, G. Ortiz, R. Alcántara, P. Lavela, C. Pérez-Vicente, J.L. Tirado, *Advancing towards a veritable calcium-ion battery: $CaCo_2O_4$ positive electrode material* Electrochemistry Communications, 67 (**2016**) 59-64.

[35] D.S. Tchitchekova, C. Frontera, A. Ponrouch, C. Krich, F. Barde, M. Rosa Palacin, *Electrochemical calcium extraction from 1D-$Ca_3Co_2O_6$*. Dalton Transactions, 47 (**2018**) 11298-11302.

[36] R. Verelli, A.P. Black, C. Frontera, J. Oro-Sole, M.E. Arroyo de Dompablo, A. Fuertes, M.R. Palacin, *On the study of Ca and Mg deintercalation from ternary tantalum nitrides.* . ACS Omega, 4 (**2019**) 8943-8952

[37] D.S. Tchitchekova, A. Ponrouch, R. Verrelli, T. Broux, C. Frontera, A. Sorrentino, F. Barde, N. Biskup, M. Elena Arroyo-de Dompablo, M. Rosa Palacin, *Electrochemical intercalation of calcium and magnesium in TiS_2: Fundamental studies related to multivalent battery applications*. Chemistry of Materials, 30 (**2018**) 847-856.

[38] R. Verrelli, A.P. Black, C. Pattanathummasid, D.S. Tchitchekova, A. Ponrouch, J. Oro-Sole, C. Frontera, F. Barde, P. Rozier, M.R. Palacin, *On the strange case of divalent ions intercalation in V_2O_5*. Journal of Power Sources, 407 (**2018**) 162-172.

[39] M.E. Arroyo-de Dompablo, C. Krich, J. Nava-Avendano, M.R. Palacin, F. Barde, *In quest of cathode materials for ca ion batteries: The $CaMO_3$ perovskites (M = Mo, Cr, Mn, Fe, Co, and Ni)*. Physical Chemistry Chemical Physics, 18 (**2016**) 19966-19972.

[40] V. Thuan Ngoc, H. Kim, J. Hur, W. Choi, I.T. Kim, *Surfactant-assisted ammonium vanadium oxide as a superior cathode for calcium-ion batteries*. Journal of Materials Chemistry A, 6 (**2018**) 22645-22654.

[41] M. Bervas, L.C. Klein, G.G. Amatucci, *Vanadium oxide-propylene carbonate composite as a host for the intercalation of polyvalent cations*. Solid State Ionics, 176 (**2005**) 2735-2747.

[42] M. Hayashi, H. Arai, H. Ohtsuka, Y. Sakurai, *Electrochemical insertion/extraction of calcium ions using crystalline vanadium oxide*. Electrochemical and Solid State Letters, 7 (**2004**) A119-A121.

[43] M. Hayashi, H. Arai, H. Ohtsuka, Y. Sakurai, *Electrochemical characteristics of calcium in organic electrolyte solutions and vanadium oxides as calcium hosts*. Journal of Power Sources, 119 (**2003**) 617-620.

[44] Y. Murata, S. Takada, T. Obata, T. Tojo, R. Inada, Y. Sakurai, *Effect of water in electrolyte on the Ca^{2+} insertion/extraction properties of V_2O_5*. Electrochimica Acta, 294 (**2019**) 210-216.

[45] M. Cabello, F. Nacimiento, R. Alcantara, P. Lavela, C. Perez Vicente, J.L. Tirado, *Applicability of molybdite as an electrode material in calcium batteries: A structural study of layer-type Ca_xMoO_3*. Chemistry of Materials, 30 (**2018**) 5853-5861.

[46] T. Tojo, H. Tawa, N. Oshida, R. Inada, Y. Sakurai, *Electrochemical characterization of a layered alpha-MoO_3 as a new cathode material for calcium ion batteries*. Journal of Electroanalytical Chemistry, 825 (**2018**) 51-56.

[47] S. Suzuki, T. Kato, H. Kawabata, M. Miyayama, *Electrode properties of todorokite-type tunnel-structured manganese oxide for calcium secondary batteries*. Journal of New Materials for Electrochemical Systems, 19 (**2016**) 51-55.

[48] P. Padigi, N. Kuperman, J. Thiebes, G. Goncher, D. Evans, R. Solanki, *Calcium cobalt hexacyanoferrate cathodes for rechargeable divalent ion batteries*. Journal of New Materials for Electrochemical Systems, 19 (**2016**) 57-64.

[49] A.L. Lipson, B.F. Pan, S.H. Lapidus, C. Liao, J.T. Vaughey, B.J. Ingram, *Rechargeable ca-ion batteries: A new energy storage system*. Chemistry of Materials, 27 (**2015**) 8442-8447.

[50] T. Tojo, Y. Sugiura, R. Inada, Y. Sakurai, *Reversible calcium ion batteries using a dehydrated prussian blue analogue cathode*. Electrochimica Acta, 207 (**2016**) 22-27.

[51] A.L. Lipson, S. Kim, B. Pan, C. Liao, T.T. Fister, B.J. Ingram, *Calcium intercalation into layered fluorinated sodium iron phosphate*. Journal of Power Sources, 369 (**2017**) 133-137.

[52] J. Rogosic, *Towards the development of calcium ion batteries*, Department of Materials Science and Engineering, Massachusetts Institute of Technology (2014)

[53] K.A. See, J.A. Gerbec, Y.S. Jun, F. Wudl, G.D. Stucky, R. Seshadri, *A high capacity calcium primary cell based on the Ca-S system*. Advanced Energy Materials, 3 (**2013**) 1056-1061.

[54] F. Bardé, M.R. Palacin, D. Stoytcheva, A. Ponrouch, M.E. Arroyo de Dompablo, N. Biskup, Titanium-based positive electrode materials for rechargeable calcium batteries and cell comprising the same, WO2018197021 (A1), (2018)

[55] R. Verrelli, A. Black, R. Dugas, D. Tchitchekova, A. Ponrouch, M.R. Palacin, *Steps towards the use of TiS_2 electrodes in ca batteries*. Journal of the Electrochemical Society, 167 (**2020**) 070532.

[56] D.S. Tchitchekova, D. Monti, P. Johansson, F. Barde, A. Randon-Vitanova, M.R. Palacin, A. Ponrouch, *On the reliability of half-cell tests for monovalent (Li^+, Na^+) and divalent (Mg^{2+}, Ca^{2+}) cation based batteries*. Journal of the Electrochemical Society, 164 (**2017**) A1384-A1392.

[57] Y.S. Meng, M. Elena Arroyo-de Dompablo, *First principles computational materials design for energy storage materials in lithium ion batteries*. Energy & Environmental Science, 2 (**2009**) 589-609.

[58] F. Zhou, M. Cococcioni, C.A. Marianetti, D. Morgan, G. Ceder, *First-principles prediction of redox potentials in transition-metal compounds with LDA + U*. PHYSICAL REVIEW B, 70 (**2004**) 8.

[59] D. Morgan, A. Van der Ven, G. Ceder, *Li conductivity in Li_xMPO_4 (M = Mn, Fe, Co, Ni) olivine materials*. Electrochemical and Solid State Letters, 7 (**2004**) A30-A32.

[60] M.K. Aydinol, A.F. Kohan, G. Ceder, K. Cho, J. Joannopoulos, *Ab initio study of lithium intercalation in metal oxides and metal dichalcogenides*. Physical Review B, 56 (**1997**) 1354-1365.

[61] M. Liu, Z. Rong, R. Malik, P. Canepa, A. Jain, G. Ceder, K.A. Persson, *Spinel compounds as multivalent battery cathodes: A systematic evaluation based on ab initio calculations*. Energy & Environmental Science, 8 (**2015**) 964-974.

[62] Z. Rong, R. Malik, P. Canepa, G.S. Gautam, M. Liu, A. Jain, K. Persson, G. Ceder, *Materials design rules for multivalent ion mobility in intercalation structures*. Chemistry of Materials, 27 (**2015**) 6016-6021.

[63] G.S. Gautam, P. Canepa, R. Malik, M. Liu, K. Perssonb, G. Ceder, *First-principles evaluation of multi-valent cation insertion into orthorhombic V_2O_5*. Chemical Communications, 51 (**2015**) 13619-13622.

[64] T.R. Juran, M. Smeu, *$TiSe_2$ cathode for beyond li-ion batteries*. Journal of Power Sources, 436 (**2019**) 226813.

[65] T.R. Juran, M. Smeu, *Hybrid density functional theory modeling of Ca, Zn, and Al ion batteries using the chevrel phase Mo_6S_8 cathode*. Physical Chemistry Chemical Physics, 19 (**2017**) 20684-20690.

[66] M. Smeu, M.S. Hossain, Z. Wang, V. Timoshevskii, K.H. Bevan, K. Zaghib, *Theoretical investigation of chevrel phase materials for cathodes accommodating Ca^{2+} ions*. Journal of Power Sources, 306 (**2016**) 431-436.

[67] Z. Zhang, X. Zhang, X. Zhao, S. Yao, A. Chen, Z. Zhou, *Computational screening of layered materials for multivalent ion batteries*. ACS Omega, 4 (**2019**) 7822-7828.

[68] https://materialsproject.org/.

CAPÍTULO 2

METODOLOGÍA

2.1. CÁLCULO MECANO-CUÁNTICO

En este apartado se desarrollarán brevemente algunos de los formalismos teóricos en los que se basan los cálculos mecano-cuánticos. Dada la complejidad del tema, y puesto que este trabajo no se centra en desarrollar una metodología sino en su aplicación al estudio de materiales, se tratará de mostrar de forma sencilla el desarrollo teórico en el cual se basa la química computacional, la evolución que ha habido hasta la forma de trabajar actualmente y las diferentes contribuciones que han hecho falta para hacer de la Química Cuántica una herramienta relevante en el campo de la Química del Estado Sólido. Una descripción detallada de los métodos computacionales, y en concreto del método DFT, se encuentran por ejemplo en [1-8].

2.1.1. Ecuación de Schrödinger

La Química del Estado Sólido realiza una gran aportación al desarrollo tecnológico de materiales con diversas aplicaciones como catalizadores, dispositivos magnéticos, ópticos, paneles solares… o como el caso que a nosotros nos atañe, electrodos para baterías. Para estudiar computacionalmente un material y sus propiedades, debemos centrarnos en el estudio de los elementos que componen la estructura interna de estos sólidos, en decir, en sus átomos constituyentes (núcleos y electrones).

Uno de los principales objetivos de la Química es el estudio de los núcleos atómicos y la interacción entre estos, todo ello sujeto a las leyes de la Química Cuántica. Aunque con la mecánica cuántica no se puede saber dónde se encuentra un electrón (Principio de Incertidumbre de Heisenberg), en 1925 Schrödinger[9] propuso una función, llamada *función de ondas* o *de estado*, que permitía relacionar la función de onda (Ψ) del sistema con la energía del mismo (E):

$$\hat{H}\Psi(\vec{r},\vec{R}) = E\Psi(\vec{r},\vec{R}) \qquad (2.1)$$

donde $\vec{r}$ y $\vec{R}$ son las coordenadas electrónicas y nucleares respectivamente, $\hat{H}$ es el operador hamiltoniano del sistema, *E* es el autovalor del operador y simboliza la energía total del sistema y Ψ es la función de onda del sistema, función propia del operador hamiltoniano, que contiene toda la información del sistema.

Para un sistema con N núcleos y n electrones, el hamiltoniano en unidades atómicas se puede escribir como:

$$\widehat{\boldsymbol{H}} = \widehat{\boldsymbol{T}}_{\boldsymbol{e}} + \widehat{\boldsymbol{T}}_{\boldsymbol{N}} + \widehat{\boldsymbol{V}}_{\boldsymbol{eN}} + \widehat{\boldsymbol{V}}_{\boldsymbol{ee}} + \widehat{\boldsymbol{V}}_{\boldsymbol{NN}} \quad (2.2)$$

Se puede observar cómo dentro del operador hamiltoniano están incluidos los operadores de energía cinética y potencial respectivamente.

Toda la información de un sistema puede conocerse si se resuelve la ecuación de Schrödinger (2.1) con el hamiltoniano definido anteriormente (2.2) encontrando las funciones propias (Ψ) y los valores propios (*E*) que satisfacen la ecuación. No obstante, la resolución de esta ecuación diferencial no es trivial teniendo en cuenta que hablamos de sistemas del orden de 10^{23} partículas interaccionantes. Desgraciadamente, la ecuación de Schrödinger solo puede resolverse analíticamente para un sistema de dos partículas como el átomo de hidrógeno.

Gracias a la aproximación de Born-Oppenheimer [10], que tiene en cuenta que la relación de masas electrón-núcleo es aproximadamente 1-2000, se produce un desacoplamiento de los movimientos electrónico y nuclear, en el que se considera que los núcleos ven a los electrones como una distribución de carga y éstos, a su vez, ven a los núcleos como cargas estacionarias. Además, hay que tener en cuenta que el término de repulsión internuclear depende únicamente de las coordenadas, y como se consideran estacionarios, se convierte en constante. Esto permite definir una *ecuación de Schrödinger electrónica:*

$$\widehat{H}_e \boldsymbol{\Psi}_e(\vec{\boldsymbol{r}}, \vec{\boldsymbol{R}}) = \boldsymbol{E}_e \boldsymbol{\Psi}_e(\vec{\boldsymbol{r}}, \vec{\boldsymbol{R}}) \quad (2.3)$$

$$\widehat{\boldsymbol{H}}_{\boldsymbol{e}} = \widehat{\boldsymbol{T}}_{\boldsymbol{e}} + \widehat{\boldsymbol{V}}_{\boldsymbol{eN}} + \widehat{\boldsymbol{V}}_{\boldsymbol{ee}} \quad (2.4)$$

Este es el punto de partida para comenzar la simulación de materiales. Se pueden distinguir dos estrategias diferentes. La primera comprende los llamados *métodos basados en la función de onda* (métodos *ab initio*), que consisten en resolver de manera aproximada la ecuación 4, y permiten obtener de manera explícita, aunque no exacta la función $\boldsymbol{\Psi}_e$. La segunda estrategia está basada en la *Teoría del Funcional de la Densidad* (*Density Functional Theory,* **DFT**) y consiste en el estudio de las propiedades del sistema a través de su densidad

electrónica $\rho_{el}(\vec{r})$, evitando la determinación explícita de la función de onda electrónica Ψ_e.

2.1.2. Teoría del Funcional de la Densidad (DFT)

La Teoría del Funcional de la Densidad es una alternativa a las metodologías basadas en la función de onda como los métodos Hartree-Fock y post-Hartree-Fock (métodos *ab initio*). Ésta surgió con el propósito de poder estudiar las propiedades de sistemas polielectrónicos de forma más sencilla que empleando la función de onda.

En los años 20, Thomas y Fermi calcularon la energía de un átomo desarrollando un modelo en el cual la energía cinética podía ser representada como función de la densidad, usando las expresiones clásicas de interacciones electrón-electrón y electrón-núcleo. A mediados de los años 1960, Hohenberg, Kohn y Sham demostraron que el estado fundamental de un sistema con muchos electrones está completamente determinado por su densidad electrónica [11, 12]. La densidad electrónica se define como la siguiente integral múltiple que se extiende sobre las coordenadas de espín de todos los electrones del sistema y sobre todas las coordenadas espaciales menos una:

$$\boldsymbol{\rho(\vec{r}) = n \int \dots \int |\Psi(\vec{\chi}_1, \vec{\chi}_2, \dots, \vec{\chi}_n)|^2 \; d\vec{\chi}_1, d\vec{\chi}_2, \dots, d\vec{\chi}_n} \tag{2.5}$$

La densidad electrónica determina la probabilidad de encontrar un electrón cualquiera de los *n* electrones del sistema dentro de un elemento de volumen dr_1 con una coordenada de espín arbitraria, mientras que el resto de los *n*-1 electrones del sistema se encuentran en coordenadas espaciales y de espín arbitrarias en el estado representado por Ψ. Su integración extendida a todo el espacio tiene como resultado el número total de electrones del sistema.

$$\boldsymbol{\int \rho(\vec{r})\, d\vec{r} = n} \tag{2.6}$$

A partir de sus dos teoremas básicos, la DFT intenta conocer la forma funcional de la densidad electrónica a partir de la cual es posible obtener la energía y todas las demás propiedades del sistema. En 1964, Hohenberg y Khon demostraron en su primer teorema que cualquier observable de un estado estacionario fundamental no-degenerado puede ser calculado, en principio de forma exacta, a partir de la densidad electrónica de este estado

fundamental [12]. Es decir, la energía del estado fundamental, la función de onda y todas las demás propiedades electrónicas, están determinadas completamente por la densidad electrónica *ρ*. En particular, Hohenberg y Kohn mostraron que la energía es un funcional de la densidad a través de la relación:

$$\boldsymbol{E[\rho] = F[\rho] + \int dr \rho(r)\, v(r)} \tag{2.7}$$

donde $\mathrm{F}[\rho]$ representa al funcional universal que contiene a la energía cinética, $\boldsymbol{T[\rho]}$, y la interacción electrón-electrón, $\hat{\mathrm{V}}_{\mathrm{ee}}[\rho]$. Con un segundo teorema los mismos autores demostraron que la densidad electrónica del estado fundamental es aquella que minimiza al funcional de energía $\boldsymbol{E[\rho]}$. Por lo tanto, la densidad electrónica de un estado fundamental no-degenerado puede ser calculada, en principio de forma exacta, determinando aquella densidad que minimiza la energía del estado fundamental. Esto implica que dada una densidad de prueba se obtiene una energía mayor o igual que la energía exacta del estado fundamental, y que la densidad electrónica del estado fundamental no degenerado se puede calcular de forma exacta, encontrando aquella densidad que minimice la energía del estado fundamental.

La minimización del funcional de la energía respecto la densidad electrónica puede hacerse mediante el método de Kohn y Sham (KS). En 1965, estos investigadores llevaron a cabo otro desarrollo muy importante al presentar una forma de aproximar al funcional universal [11]. Consideraron un sistema ficticio de *n* electrones que no interactúan y que experimentan todos ellos la misma función de energía potencial, haciendo coincidir la densidad electrónica del sistema de referencia con la densidad electrónica exacta. La función de onda del estado fundamental del sistema de referencia es un determinante de Slater cuyos elementos son funciones que representan a cada uno de los electrones del sistema (orbitales). De esta manera, la energía cinética se puede desglosar como una suma de energías cinéticas individuales:

$$T_s[\rho] = \sum_{i=1}^{N} \int dr\, \boldsymbol{\Psi_i^*(r)}\left(-\frac{\hbar}{\boldsymbol{2m}}\nabla^2\right)\boldsymbol{\Psi(r)} \tag{2.8}$$

Y la densidad electrónica es igual a la suma de densidades orbitales

$$\rho(r) = \sum_{i=1}^{N} \rho_i(r) \sum_{i=1}^{N} \Psi_i^*(r)\Psi_i(r) \tag{2.9}$$

Otra ventaja en el modelo de KS es la aproximación a la interacción electrón-electrón, proponiendo la interacción coulombiana como parte principal en la misma, y quedando el funcional universal de la siguiente manera:

$$F[\rho] = T[\rho] + V_{ee}[\rho] = T[\rho] + J[\rho] + E_{xc}[\rho] \quad (2.10)$$

Por tanto, el funcional de intercambio y correlación, $E_{xc}[\rho]$, se define como:

$$E_{xc}[\rho] = T[\rho] - T_s[\rho] + V_{ee}[\rho] - J[\rho] \quad (2.11)$$

Los orbitales de Kohn y Sham permiten definir la función de onda como el determinante de Slater construido a partir de los orbitales que da la energía más baja para el problema de valores de ρ. Aunque las ecuaciones de Kohn-Sham se resuelven iterativamente y son muy similares al método de Hartree-Fock, el significado físico de ambos métodos es diferente ya que tienen asociados potenciales efectivos distintos.

Aun habiendo llegado a esta aproximación, no se conoce la forma exacta del funcional para las energías de intercambio y correlación, que corresponden a las interacciones cuánticas que existen entre los electrones, ya sean debidas al principio de exclusión de Pauli entre electrones de mismo spin o debido a la repulsión culombiana.

2.1.2.1. Aproximación de la densidad local (LDA)

La primera aproximación para este funcional se conoce como *Aproximación de Densidad Local (Local Density Approximation, LDA)* y consiste en suponer que la energía de intercambio y correlación de un punto se corresponde con la densidad electrónica en ese punto, suponiendo que los electrones forman una "nube electrónica uniforme".

$$E_{xc}[\rho(\vec{r})] = \int \varepsilon_{XC}^{LDA}[\rho(\vec{r})]d\vec{r} \quad (2.12)$$

donde ε_{xc}^{LDA} es la energía de intercambio-correlación por partícula de un sistema con densidad $\rho(\vec{r})$.

Las contribuciones del intercambio y de la correlación pueden tratarse independientemente, siendo ε_{xc}^{LDA} la suma de las dos:

$$\varepsilon_{XC}^{LDA}[\rho(\vec{r})] = \varepsilon_{X}^{LDA}[\rho(\vec{r})] + \varepsilon_{C}^{LDA}[\rho(\vec{r})] \quad (2.13)$$

Para el término de intercambio (ε_x) se usa el modelo de un gas de electrones homogéneo, mientras que para la energía de correlación por partícula (ε_c) se utilizan expresiones analíticas aproximadas y ajustadas a valores obtenidos mediante cálculos cuánticos de Monte Carlo. La expresión analítica más utilizada es la propuesta por Vosko, Wilk y Nusair (VWN) [13].

A pesar de la simplicidad de esta aproximación, se obtienen resultados bastante buenos a partir de cálculos LDA de algunas propiedades del estado fundamental para sistemas metálicos, y en menor medida para algunos sistemas iónicos y covalentes [3]. Pese a que la LDA sobreestima los valores de las energías de enlace y las barreras energéticas en sistemas con enlaces débiles, esta aproximación ayuda a predecir muchas propiedades electrónicas de gran utilidad como las densidades de carga, las frecuencias vibracionales y la geometría del sistema.

2.1.2.2. Aproximación del gradiente generalizado (GGA)

Los cálculos DFT ya eran muy utilizados en la década de 1970 para estudios de Física del Estado Sólido, pero por desgracia los funcionales LDA no eran suficientemente precisos para estudiar la mayoría de las aplicaciones de materiales. Pasaron casi 20 años hasta que se desarrollaron nuevos funcionales que pudieron usarse de manera efectiva para cálculos cuánticos. Para ello, se partió de la base no sólo de usar la densidad electrónica, sino también incluir información sobre el *gradiente de la densidad electrónica* ($\nabla\rho(\vec{r})$), para así poder tener en cuenta la variación de la densidad electrónica en cada punto, tratándose, por tanto, de una aproximación semilocal. A esta aproximación se la conoce como *Aproximación del Gradiente Generalizado (Generalized Gradient Approximation GGA)*.

$$\varepsilon_{XC}^{GGA}[\rho(\vec{\boldsymbol{r}})] = \int f\,(\rho,\rho)\nabla d\vec{\boldsymbol{r}} \qquad (2.14)$$

La introducción de los efectos de gradiente conduce a una mejora en las geometrías calculadas, las frecuencias y las densidades de carga, en comparación con la aproximación LDA. En referencia a análisis estructural, generalmente LDA subestima el volumen, pero sobreestima el módulo de compresibilidad y la energía de cohesión. Con GGA ocurre justo lo contrario [3]. No obstante, el principal argumento a favor del método GGA es la mejora en las energías totales obtenidas.

La mayoría de funcionales GGA contiene algún parámetro ajustable de forma que se reproduzcan las energías de una serie de átomos. De entre los funcionales GGA, el funcional PW91, desarrollado por Perdew [14, 15], es el único puramente *ab initio*, ya que fue construido utilizando datos del gas uniforme de electrones y condiciones exactas. Los principales problemas que presentaba el funcional PW91 son: a) la derivación es larga y depende de muchas variables; b) la función no es trivial y c) se sobrevalora; d) los parámetros no están debidamente correlacionados; e) la parametrización analítica no funciona correctamente en los límites de alta densidad.

En 1996, Perdew, Burke y Erzerhof [16] desarrollaron un nuevo funcional (PBE) basándose en la GGA y mejorando el funcional PW91. En este nuevo funcional se trató de mejorar la descripción de la nube electrónica, de corregir el comportamiento del mismo bajo un campo uniforme y usar un potencial más suave. En esta tesis se ha utilizado este funcional PBE.

2.1.3. Método DFT+ U

Una de las deficiencias de los funcionales LDA y GGA es la llamada autointeracción (*self-interaction*). Dentro del potencial coulombiano, existe una contribución correspondiente a la repulsión del electrón consigo mismo. En el método Hartree-Fock ese término es anulado con el término de intercambio. Sin embargo, debido a que el término de intercambio para la DFT es aproximado, la autointeracción no es completamente anulada. Esta deficiencia provoca que los orbitales de Kohn-Sham muy localizados sean desestabilizados. Por este motivo, los electrones desapareados tienden a deslocalizarse espacialmente para minimizar la autointeracción. Así, los métodos LDA y GGA proporcionan un tratamiento deficiente de la correlación electrónica para sistemas con estados muy localizados, ya que ambos están basados en la descripción de las interacciones electrónicas que ofrece el modelo de gas de electrones. Como ejemplo, el método GGA predice un comportamiento metálico o semiconductor para muchos óxidos de metales de transición, cuando experimentalmente éstos tienen un marcado carácter aislante. Es decir, las aproximaciones LDA y GGA no son capaces de describir correctamente la estructura electrónica de estos materiales altamente correlacionados, sobre todo el *gap* entre la banda de conducción y la de valencia.

Desarrollado en la década de 1990, el método DFT+U amplía el funcional de aproximación para hacer frente a las propias interacciones electrónicas [17, 18]. El nombre

DFT+U se utiliza para referirse al método en sí mismo, sin referencia explícita a LDA o GGA (LDA+U o GGA+U). Este método combina la alta eficiencia de LDA/GGA y un tratamiento explícito de correlación con un modelo similar a Hubbard para un subconjunto de estados en el sistema. Así, los electrones *d* y *f* (deslocalizados erróneamente por DFT) se tratan separadamente de los *s* y *p.* Para ello se aplica un término de interacción de tipo Hubbard E_{Hub} que corrige el funcional:

$$E_{LSDA+U}[\rho(r)] = E_{LSDA}[\rho(r)] + E_{Hub}[\{n_i^{\sigma}\}] - E_{DC}[\{n_i^{\sigma}\}] \quad (2.15)$$

donde ρ(r) es la densidad electrónica y ni^{σ} son las ocupaciones de los orbitales del átomo *i* con espín *σ* que experimenta el término de Hubbard. El último término es añadido para evitar contar por duplicado las interacciones contenidas en E_{Hub} y E_{LSDA} y depende de dos términos; el término de interacción de Coulomb (U) y el término de intercambio (J). Durante la realización de esta tesis, se ha utilizado el formalismo rotacionalmente invariable introducido por Dudarev *et al.* [19] tal y como ha sido implementado en el código VASP. En este formalismo, los parámetros *U* y *J* se combinan en un único parámetro efectivo U_{eff} que se define como U_{eff}=$U-J$.

El valor apropiado del parámetro *U* a utilizar en el cálculo depende de cada material [20] y se puede determinar a partir de propiedades determinadas experimentalmente: momentos magnéticos y band gaps [21], voltajes de inserción de litio [22], o entalpías de reacción [23]. Todos los materiales estudiados en esta Tesis poseen metales de transición (centros redox activos en la reacción de intercalación), por lo que la metodología DFT+U se ha utilizado tanto para el estudio de óxidos (capítulos 3.2, 3.3 y 3.4) como de compuestos basados en oxopolianiones (capítulo 3.1).

2.1.4. Funcionales híbridos

A pesar de los buenos resultados obtenidos con los funcionales GGA o GGA+U, el problema principal de estos funcionales es que no reproducen correctamente los efectos de intercambio. Este problema puede solventarse introduciendo la energía de intercambio exacto tal y como se calcula con la teoría de Hartree-Fock, donde la energía de intercambio exacto se obtiene calculando el determinante de Slater.

Se obtienen así los llamados *funcionales híbridos,* que se basan en la conexión adiabática [24]. Con esta contribución de energía exacta, se obtiene la siguiente energía de intercambio-correlación:

$$E_{xc} = \varepsilon_X^{HF} + \varepsilon_C^{KS} \quad (2.16)$$

donde E_x^{HF} es la energía de intercambio exacto Hartree-Fock y E_c^{KS} es la energía de correlación obtenida con los orbitales de Kohn-Sham.

Los funcionales híbridos son los únicos funcionales que son completamente no locales, es decir, que el intercambio exacto depende de la densidad electrónica en los puntos *r'* alrededor de *r*. Estos funcionales han proporcionado algunas de las energías y estructuras más precisas en la historia de la DFT [25-28]. Algunos de los funcionales híbridos más usados son B3LYP, B3PW91 o PBE0. A pesar del buen resultado obtenido con estos funcionales frente a los GGA o GGA+U (véase por ejemplo [29, 30]), debido a su alto coste computacional no se han utilizado en esta Tesis.

2.1.5. Incorporación de las fuerzas de dispersión

Las fuerzas de dispersión juegan un papel fundamental a la hora de calcular la estructura de ciertos sólidos cristalinos y las propiedades asociadas a los mismos. Uno de los problemas asociados a la Teoría del Funcional de la Densidad es que el coeficiente de intercambio y correlación no describe con "exactitud" la interacción que sufren los electrones entre sí mismos cuando están un poco más alejados, es lo que se conoce como *fuerzas de dispersión*. La fuerza de dispersión puede considerarse como una interacción atractiva que origina que cualquier fluctuación en la densidad de carga afecte en el sistema. Los funcionales de intercambio y correlación clásico, como funcionales de intercambio y correlación (LDA, GGA o híbridos), no tienen en cuenta estas dispersiones debido sobre todo a dos causas: las fluctuaciones no están consideradas y sólo tienen en cuenta las propiedades locales para calcular la energía.

Dentro de los materiales para baterías el tratamiento específico de las fuerzas de dispersión es esencial para el estudio de compuestos de intercalación laminares (TiS_2 [31, 32], V_2O_5 [33]). Para estos materiales las correcciones del funcional de intercambio y correlación introducidas por Klimes permiten una descripción más adecuada de las interacciones de Van der Waals [34-36]. El capítulo 3.2 (óxidos de cobalto) muestra los

resultados obtenidos al tratar específicamente este tipo de interacciones con la corrección optB86 [34, 35].

2.1.6. Sistemas periódicos.

2.1.6.1. Condiciones de periodicidad

Sin duda, una de las aproximaciones más útiles a la hora de trabajar en estado sólido sea la aportación del *teorema de Bloch* sobre condiciones de contorno periódicas. Debido al número infinito de electrones que puede existir en un sólido cristalino, las funciones de ondas de los mismos son también infinitas y, por tanto, también lo son las bases requeridas para los orbitales de Khon-Sham.

El teorema de Bloch se basa en tres hipótesis: 1) los átomos de un cristal están distribuidos de forma periódica en una red de Bravais; 2) debido a la estructura ordenada descrita en el punto 1), el potencial de un cristal es una función periódica que cumple que $|\varphi(r+R)|^2 = |\varphi(R)|^2$, donde r son las posiciones cristalinas de los átomos dentro de la red de Bravais y R el vector de traslación de la red asociado; 3) los electrones son independientes y no interactúan entre sí, por tanto, la solución de la ecuación de Schrödinger para la función de onda electrónica se denominan funciones de Bloch y son de la forma:

$$\varphi(x) = e^{ikx} u_k(x) \tag{2.17}$$

$$u_k(x) = u_k(x+r) \tag{2.18}$$

Cada onda de Bloch representa una onda plana con longitud de onda λ=2π/k y una función amplitud $u_k(x)$ de periodo *d* igual al de la red cristalina. En resumen, se trata el problema de las condiciones de contorno de un cristal como si un electrón al salirse del cristal entrara directamente por el otro lado. Dicho de manera técnica: las autofunciones de la ecuación de onda para un potencial cristalino periódico son el producto de una onda plana y otra función periódica con igual periodo que la red cristalina.

Es importante mencionar la zona de Brillouin, el espacio más cercano dentro de la red recíproca, pues define la zona de interés de estudio, donde se propagan las ondas descritas mediante el teorema de Bloch. En este trabajo, para muestrear la primera zona de Brillouin se han utilizado diferentes mallas de puntos *k* dependiendo del sistema considerado. La

malla concreta de puntos *k* usados se especifica al comienzo de cada sección. La selección de las mallas se ha hecho de forma que se garantiza la convergencia de los valores de las propiedades estudiadas

2.1.6.2. Base de ondas planas

Para la resolución de las ecuaciones de Kohn-Sham en sistemas periódicos, la función de onda debe satisfacer el teorema de Bloch, según el cual las funciones de ondas para cada punto k del espacio pueden ser representadas mediante un paquete de ondas planas discretas. Las bases de ondas planas son un conjunto completo de funciones matemáticas sencillas, no centradas en los átomos con las que se puede resolver la ecuación de K-S:

$$\sum_G{}' \left[\frac{\hbar^2}{2m}|k+G|^2\delta'_{GG} + V_{ion}(G-G') + V_H(G-G') + V_{XC}(G-G')\right] c_{i,k+G'} = \varepsilon_i c_{i,k+G} \quad (2.19)$$

De esta forma, la energía cinética es diagonal y los potenciales vienen descritos en términos de sus transformadas de Fourier. Para resolver la ecuación anterior, se realiza la diagonalización de la matriz hamiltoniana, cuyo tamaño viene dado por la energía del *cut-off*, $\frac{\hbar^2}{2\mathrm{m}}|\mathrm{k}+\mathrm{G}|^2$. La elección del parámetro de corte (cut-off) se hace en base al funcional utilizado y la optimización del tiempo de cálculo. En este trabajo, se ha utilizado típicamente un valor de 600 eV.

2.1.6.3. Pseudopotenciales

Aunque el teorema de Bloch resulta de gran utilidad ya que permite aplicar las condiciones de contorno a la hora de resolver las funciones de onda, para obtener un buen resultado para los electrones cercanos al núcleo necesitamos un número de ondas demasiado grande. En el caso de los sólidos, sus propiedades dependen mucho más de los electrones de valencia que de los electrones internos. Por ello, en lugar de la función de onda de todos los electrones, se definen unas pseudofunciones (figura 2.1). En la zona ocupada por los electrones más internos o más cercanos al núcleo, la función de onda de los electrones oscila rápidamente debido al potencial creado en esta región. Por ello, a esta zona donde se incluyen a los electrones más internos (*core*) se trata de suavizar el potencial y la función de onda mediante el uso de pseudopotenciales y pseudofunciones, y fuera de la región del *core* los potenciales y pseudopotenciales son iguales [37].

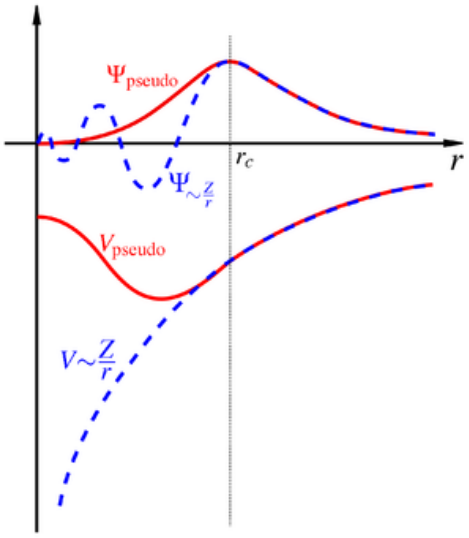

Figura 2.1. Representación esquemática de un potencial teniendo en cuenta todos los electrones (líneas continuas) y un pseudopotencial (líneas discontinuas) con sus respectivas funciones de onda. El radio en el que se igualan es el radio de corte r_c.

Los pseudopotenciales pueden ser empíricos o teóricos [38, 39], los teóricos son potenciales *ab initio*. La aproximación de pseudopotenciales no nos proporciona información directa de la función de onda, pero podemos obtener la densidad electrónica, lo que permite analizar gran parte de las propiedades del sólido.

En esta Tesis se ha utilizado el método del proyector de ondas aumentadas (PAW, de sus siglas en inglés "*Projector augmentes wave method")* donde se generalizan y aúnan los métodos de ondas planas aumentadas y los pseudopotenciales, permitiendo una mejoría en los resultados de los cálculos computacionales [40, 41].

2.2. DFT EN EL ESTUDIO DE MATERIALES PARA BATERÍAS

En este trabajo, el comportamiento electroquímico de los materiales ha sido evaluado atendiendo a tres aspectos: voltaje de intercalación medio, variaciones estructurales durante los ciclos carga/descarga de la batería y conductividad electrónica del material. Para ello consideramos una reacción de intercalación de Ca (electrodo negativo) en el material Ca_{x1}-Host (electrodo positivo):

$$(x_2\text{-}x_1)\ Ca(s) + Ca_{x1}Host \rightarrow Ca_{x2}Host \qquad \text{(reac. 2.1)}$$

Mediante los cálculos DFT pueden conocerse la energía total, la estructura cristalina y la estructura electrónica de los compuestos involucrados (fig. 2.2). Con este conocimiento, es posible predecir y entender las propiedades electroquímicas del sistema estudiado (Ca_xHost).

Como punto de partida, se necesita la estructura cristalina y la composición del material a estudiar. En este trabajo hemos partido de las estructuras cristalinas recogidas en la base de datos de ICSD (Inorganic Crystal Structure Database)[42]. Detalles concretos para cada material se aportan en el capítulo de resultados. Para una estructura dada, se puede realizar un cálculo DFT estático, o por el contrario se puede permitir la optimización geométrica de la estructura. En esta Tesis las estructuras han sido optimizadas permitiendo la relajación simultánea de los parámetros, forma y volumen de la celda unidad, y de las posiciones atómicas. Se ha considerado que la optimización geométrica ha finalizado cuando la diferencia de energías entre dos iteraciones sucesivas es más pequeña que 10^{-4} eV y la diferencia de energías entre cada paso iónico es también más pequeña que 10^{-3} eV. Teniendo en cuenta otros parámetros del cálculo, esto corresponde a una convergencia en la energía total del orden de 10 meV/ fórmula unidad.

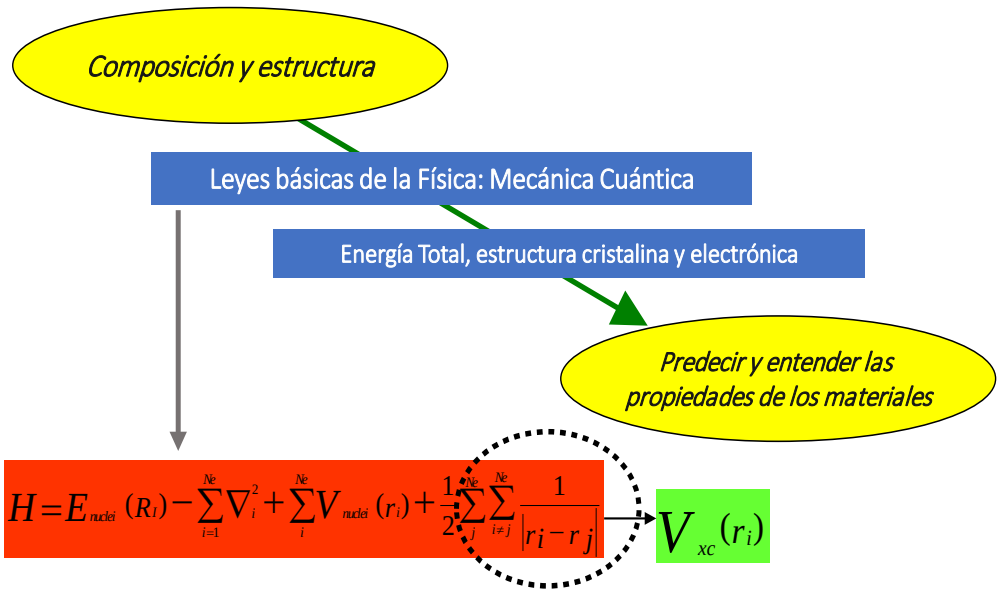

Figura 2.2. Esquema de la aplicación de DFT al estudio de materiales. Partiendo de la composición y estructura de un material (real o virtual) es posible conocer la energía total, estructura electrónica y estructura cristalina, lo que permite entender y predecir las propiedades.

2.2.1. Voltaje medio de intercalación

En los últimos años los cálculos a partir de primeros principios se han convertido en un método rápido y preciso para predecir voltajes de inserción de distintos iones (Li, Na, Ca, Mg...) en materiales inorgánicos [33, 43, 44]. Gracias a la introducción del tratamiento específico de la correlación electrónica en la teoría del funcional de la densidad (DFT + U) es posible predecir voltajes de intercalación que difieren de los experimentales en tan sólo 0.1 V [22, 45]. El voltaje medio de la reacción de intercalación de Calcio (rec. 2.1) puede expresarse como:

$$\overline{V}(x) = -\frac{\Delta Gr}{(x_2\text{-}x_1)zF} \tag{2.20}$$

donde z, número de electrones intercambiados, que es 2 para el Ca, y F es la constante de Faraday.

Por otro lado, la energía libre de la reacción de intercalación (rec. 2.1) es:

$$\Delta G_r = \Delta E_r + p\Delta V_r - T\Delta S_r \tag{2.21}$$

En estado sólido, el término entrópico y la variación de volumen son despreciables frente al término entálpico; el término ΔE_r de (2.21) es del orden de 2-3 eV, mientras que los términos $p\Delta V_r$ es del orden de 10^{-5} eV (a 0K). El término $T\Delta S_r$, es del orden de la energía térmica (a temperatura ambiente K_BT = 0.025 eV), es decir, mucho menor que ΔE_r. Así, la energía libre de la reacción puede aproximarse a la energía total de la reacción, es decir, se puede llevar a cabo la aproximación: $\Delta G_r \approx \Delta E_r$ [43]. Con esta aproximación, la estimación del voltaje de la reacción de intercalación puede hacerse obteniendo el término E_r según la expresión

$$E_r = E\,\text{total}\,(Ca_{x2}\text{Host}) - [(x2 - x1)\,E\,\text{total}\,(Ca) + E\,\text{total}\,(Ca_{x1}\text{Host})] \tag{2.22}$$

Puesto que las energías totales son un resultado directo del cálculo DFT, la estimación del voltaje de intercalación medio es una operación trivial. Debe notarse que el voltaje medio puede calcularse entre dos composiciones límites x_1 y x_2 cualesquiera. Para simular ciertas composiciones, intermedias entre la máxima y mínima ocupación de un sitio cristalográfico, es necesario crear modelos cristalográficos adecuados y es aquí dónde radica la complejidad del cálculo del voltaje medio. Un claro ejemplo es el estudio de los óxidos de

cobalto que se presenta en esta Tesis (capítulo 3.2). En esta Tesis se ha utilizado el programa CASM (Cluster Approach to Statistical Mechanics) [46] para generar superestructuras y configuraciones Ca/vacantes para las composiciones intermedias.

2.2.2. Variaciones estructurales asociadas a la reacción de intercalación

Los cambios que ocurren en la celda unidad de un material de intercalación en función de la cantidad de calcio pueden investigarse a partir de primeros principios. Además de la energía total, el cálculo proporciona las posiciones cristalinas que ocupan los átomos en la celda optimizada. Por lo tanto, es posible conocer cómo varían los parámetros de celda y el volumen al intercalar/desintercalar calcio en la estructura, y con ello estudiar la posibilidad de cambios estructurales drásticos que afectarían a la reversibilidad de la reacción de intercalación, y en última instancia a la vida media de la batería. Esto nos permitirá evaluar las prestaciones electroquímicas de los materiales estudiados atendiendo a criterios de estabilidad estructural.

2.2.3. Conductividad intrínseca del material: conductividad iónica

Como tercer punto para predecir las propiedades electroquímicas, nos centraremos en la conductividad eléctrica de los materiales estudiados. La conducción eléctrica ocurre por la migración, de electrones o iones, en distancias del orden del tamaño de los cristales. Un material de electrodo óptimo debe tener buena conducción electrónica e iónica. En una primera aproximación, se puede determinar si un sólido es un conductor electrónico inspeccionando la densidad de estados calculada (*Density of States*, DOS). Debe, no obstante, puntualizarse que el valor del band-gap no proporciona una información completa sobre la conductividad electrónica, ya que ésta puede deberse a contribuciones como el movimiento de polarones, como ocurre, por ejemplo, en el material de electrodo Li_xFePO_4 [47].

Los cálculos a partir de primeros principios pueden también suministrar información sobre la movilidad iónica, parámetro crucial en los electrodos para baterías de Ca. El coeficiente de difusión del Ca dentro del compuesto anfitrión se relaciona con la potencia de batería. Un coeficiente de difusión alto es condición necesaria -aunque no suficiente- para que la batería nos proporcione la energía “rápidamente”, siendo la ecuación que relaciona ambos conceptos:

$$L = \sqrt{D\tau} \tag{2.23}$$

donde L es la longitud de difusión de los portadores (Ca^{2+} en nuestro caso), que provee una medida de cuán lejos se propaga por difusión a un tiempo τ, siendo D el coeficiente de difusión. Por ejemplo, para una partícula micrométrica, para cargar la batería en 2 horas (rate C/2) se requeriría un coeficiente de difusión del orden de 1.4 10^{-12} cm^2/s.

El coeficiente de difusión puede conocerse mediante cálculos de dinámica molecular clásica –si se conoce el campo de fuerzas- o bien mediante dinámica molecular ab initio, cálculo extremadamente costoso e impracticable cuando la movilidad iónica es muy baja [48]. Un método razonablemente asequible (en términos de tiempo de cálculo) consiste en calcular la energía de la barrera de la difusión (E_{act}) en lugar del coeficiente de difusión. La relación entre ambos viene dada por:

$$D = a^2 v e^{-\frac{E_{act}}{K_B T}} \tag{2.24}$$

donde a es la distancia del salto entre la posición inicial y la final (del orden de 3 Å), v es la frecuencia (del orden de 10^{12} s), K_B es la constante de Boltzman y T la temperatura. Aplicando la ecuación (ec. 25) para un coeficiente D = 1.410^{-12} cm^2/s (ejemplo anterior, que corresponde a un C/2 y partícula micrométrica), la energía de activación del proceso de difusión a 298 K es 0. 5 eV. La tabla 2.1 muestra los valores de E_{act} calculada y la D estimada por Morgan y colaboradores [49] en el caso de los olivinos $LiMPO_4$ (el Li es la especie que difunde) y que indican que se trata de buenos conductores iónicos, independientemente del metal de transición y contenido en litio.

Tabla 2.1 Energía de activación calculada mediante DFT para compuestos Li_xMPO_4, y su correspondiente coeficiente de difusión estimado a partir de la ecuación 2.24. [49]

Cation M	$x \approx$	E_{Act} (meV)	D (cm^2/s)
Mn	0	330	10^{-9}
Mn	1	250	10^{-7}
Fe	0	200	10^{-7}
Fe	1	270	10^{-8}
Co	0	110	10^{-5}
Co	1	360	10^{-9}
Ni	0	120	10^{-5}
Ni	1	130	10^{-5}

A partir de las ecuaciones (2.23) y (2.24) se puede estimar la barrera tolerable para cargar/descargar la celda en un determinado tiempo. Estos límites para la barrera de difusión permiten evaluar si un material tiene potencial interés como electrodo positivo. La figura 2.3 muestra la relación entre el tiempo de carga de la batería, el tamaño de partícula y la barrera energética. Si la barrera energética es muy alta (superior a 1.2 eV), la difusión es nula, de forma que el material resulta inactivo, incluso a velocidades de ciclado extremadamente bajas (C/200).

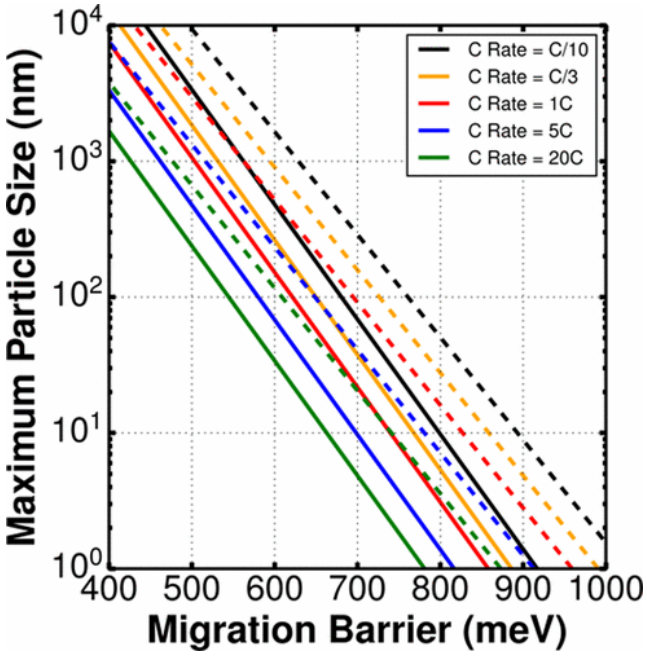

Figura 2.3. Relación entre la barrera de migración para iones Ca^{2+} y el tamaño de partícula para distintas velocidades de ciclado de una celda (C Rate). Líneas sólidas y punteadas corresponden a temperaturas de 298 K y 333 K, respectivamente. Tomada de [44].

Según lo anterior, en este trabajo para evaluar la movilidad de los iones Ca^{2+} en las estructuras estudiadas se ha calculado la barrera de la difusión mediante el método NEB (de sus siglas en inglés "*Nudged Elastic Band*"). Este es un método de interpolación, que aplica la teoría del estado de transición; el concepto básico es que la migración iónica ocurre por una sucesión de saltos desde un estado inicial a uno final mediante una serie de estados de transición. Los estados intermedios (imágenes) se generan por interpolación entre las dos posiciones atómicas (inicial y final) y se calcula la barrera energética como si todas las imágenes estuvieran unidas mediante una banda elástica de forma que todas van ajustándose a la vez [50, 51]. El método presenta distintas variantes [52-55]. La figura 2.4 muestra un ejemplo en una estructura tipo olivino (adaptado de [56]). El ión difunde desde

la posición octaédrica señalada en amarillo, hasta la posición octaédrica contigua que está vacante. Entre estas dos posiciones se interpolan cinco posiciones intermedias, que en este caso pasan por la cara del octaedro ocupado, el tetraedro intermedio y la cara del octaedro vacante.

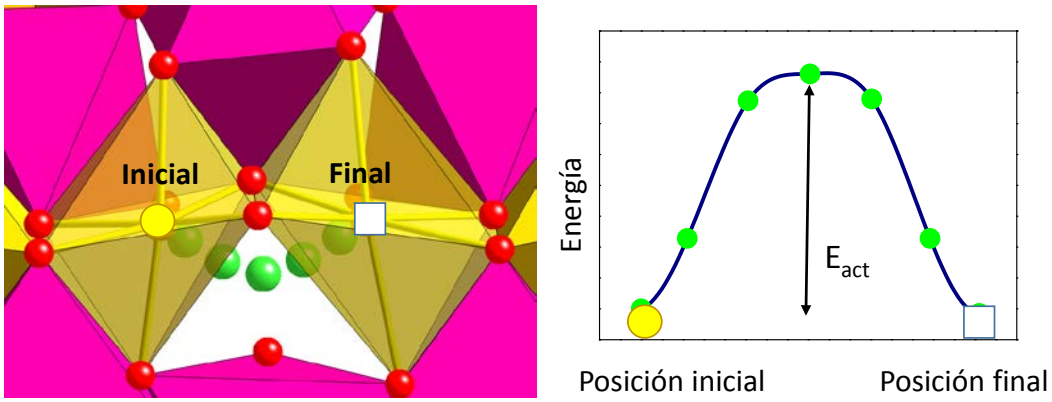

Figura 2.4. Difusión de un catión en la estructura tipo olivino mediante mecanismo de "hopping". El catión salta desde la posición inicial (en amarillo) a la posición final (en blanco). Adaptada de [56].

Para estudiar la difusión mediante la teoría del estado de transición, es necesario calcular las fuerzas que actúan sobre los átomos en las imágenes a lo largo del camino de difusión utilizando la mecánica cuántica. Es decir, se calcula el camino de mínima energía entre las configuraciones inicial y final, pasando por un número determinado de configuraciones de transición (imágenes, en verde en la figura 2.4). El método NEB implica que cada una de las imágenes intermedias tenga que relajarse (a volumen constante) atendiendo no sólo a su propia posición y entorno, sino también a cómo se relajen las imágenes que tenga a su lado, que a su vez se verán afectadas por las adyacentes. Por tanto, cada imagen simultáneamente está relajándose y obligando a relajarse a las demás. La máxima energía alcanzada en el camino inicial-transición-final determina la energía de activación asociada a la difusión).

Debe señalarse que el cálculo de barreras mediante el método NEB requiere que la interacción entre los defectos sea mínima. Por ello, para mecanismo más sencillo de hopping de la figura 2.4, sólo pueden calcularse las barreras en los límites composicionales diluidos lo que obliga a trabajar con superceldas. Por ejemplo, en el caso de olivino Li_xMPO_4 los límites diluidos son x ~0 y x ~1. Para alcanzar esas composiciones se toman superceldas, así, el límite diluido x ~1 puede simularse creando una vacante en una supercelda de orden 16

($Li_{16}M_{16}P_{16}O_{64}$), lo que corresponde a la composición $Li_{15}M_{16}P_{16}O_{64}$ o $Li_{0.9375}M_{16}P_{16}O_{64}$. Debe alcanzarse un compromiso entre el tamaño de la supercelda y el coste computacional; un buen criterio es tomar superceldas en las que los defectos (vacantes en el límite x ~ 1 o iones en el límite x~0) estén separadas en al menos 8 Å.

En este trabajo los cálculos NEB se han realizado utilizando funcionales GGA. Un cálculo NEB dentro de DFT + *U* es difícil de converger debido a la pronunciada metaestabilidad de los estados electrónicos a lo largo del camino de migración de iones [57]. Además, y al contrario de lo observado para la predicción de voltajes, no hay evidencias concluyentes en la literatura de que la inclusión del término *U* en el cálculo proporcione mejores resultados de energías de activación.

2.3. REFERENCIAS

[1] J. Amaya Suárez, *Propiedades optoelectrónicas de óxidos y sulfuros metálicos*. Tesis Doctoral, Departamento de Química Física, Universidad de Sevilla, (**2019**).

[2] W. Koch, M.C. Holthausen, A chemist´s guide to density functional theory, Wiley-VCH, Weinheim, 2000.

[3] R.M. Martin, Electronic structure: Basic theory and practical methods, Cambridge University Press, 2004.

[4] R.G. Parr, W. Yang, Density functional theory of atoms and molecules, Oxford University Press,, New York, 1989.

[5] G. Kresse, et al., *Programa vasp: Documentación y manual* https://www.vasp.at/wiki/index.php/The_VASP_Manual

[6] C. Arasa Cid, *Procesos químicos con oxígeno y nitrógeno sobre cristobalita: Estudio teórico desde primeros principios*, Tesis Doctoral, Departamento de Química Física, Universidad de Barcelona, 2007.

[7] D.S. Sholl, J.A. Steckel, Density functional theory: A practical introduction, Wiley, New Jersey, 2009.

[8] F. Giustino, Materials modelling using density functional theory: Properties and predictions, Oxford University Press, Oxford, 2014.

[9] E. Schröndinger, *An ondulatory theory of mechanics of atoms and molecules*. The Physical Review, 28 (**1926**) 1049-1070.

[10] M. Born, R. Oppenheimer, *Quantum theory of molecules*. Annalen Der Physik, 84 (**1927**) 0457-0484.

[11] W. Kohn, L.J. Sham, *Self-consistent equations including exchange and correlation effects*. Physical Review 140 (**1965**) A1133-A1138.

[12] P. Hohenberg, W. Kohn, *Inhomogeneous electron gas*. Phys. Rev. B, 136 (**1964**) B864–B871.

[13] S.H. Vosko, L. Wilk, M. Nusair, *Accurate spin-dependent electron liquid correlation energies for local spin-density calculations - a critical analysis*. Canadian Journal of Physics, 58 (**1980**) 1200-1211.

[14] J.P. Perdew, Y. Wang, *Accurate and simple analytic representation of the electron-gas correlation-energy*. Physical Review B, 45 (**1992**) 13244-13249.

[15] J.P. Perdew, J.A. Chevary, S.H. Vosko, K.A. Jackson, M.R. Pederson, D.J. Singh, C. Fiolhais, *Atoms, molecules, solids, and surfaces - applications of the generalized gradient approximation for exchange and correlation*. Physical Review B, 46 (**1992**) 6671-6687.

[16] J.P. Perdew, K. Burke, M. Ernzerhof, *Generalized gradient approximation made simple*. Physical Review Letters, 77 (**1996**) 3865-3868.

[17] V.I. Anisimov, I.V. Solovyev, M.A. Korotin, M.T. Czyzyk, G.A. Sawatzky, *Density-functional theory and NiO photoemission spectra*. Physical Review B, 48 (**1993**) 16929-16934.

[18] V.I. Anisimov, J. Zaanen, O.K. Andersen, *Band theory and Mott insulators - hubbard-U instead of stoner-I*. Physical Review B, 44 (**1991**) 943-954.

[19] S.L. Dudarev, G.A. Botton, S.Y. Savrasov, Z. Szotek, W.M. Temmerman, A.P. Sutton, *Electronic structure and elastic properties of strongly correlated metal oxides from first principles: LSDA+U, SIC-LSDA and EELS study of UO_2 and NiO*. Physica Status Solidi a-Applied Research, 166 (**1998**) 429-443.

[20] M. Cococcioni, S. de Gironcoli, *Linear response approach to the calculation of the effective interaction parameters in the LDA+U method*. Physical Review B, 71 (**2005**) 16.

[21] L. Li, W. Yu, C. Jin, *First-principles study of pressure-induced phase transition in the strongly correlated compound $YCrO_4$*. Physical Review B 73 (**2006**) 174115.

[22] F. Zhou, M. Cococcioni, C.A. Marianetti, D. Morgan, G. Ceder, *First-principles prediction of redox potentials in transition-metal compounds with LDA+U*. Physical Review B, 70 (**2004**) 8.

[23] L. Wang, T. Maxisch, G. Ceder, *Oxidation energies of transition metal oxides within the GGA+U framework*. Physical Review B, 73 (**2006**) 6.

[24] J.A. Harris, *Adiabatic-connection approach to Kohn-Sham theory.* Phys. Rev. A., 29 (**1984**) 1648-1659.

[25] J. Heyd, J.E. Peralta, G.E. Scuseria, R.L. Martin, *Energy band gaps and lattice parameters evaluated with the Heyd-Scuseria-Ernzerhof screened hybrid functional*. Journal of Chemical Physics, 123 (**2005**) 174101.

[26] J. Paier, M. Marsman, K. Hummer, G. Kresse, I.C. Gerber, J.G. Angyan, *Screened hybrid density functionals applied to solids*. Journal of Chemical Physics, 124 (**2006**) 154709.

[27] Y. Zhao, D.G. Truhlar, *Hybrid meta density functional theory methods for thermochemistry, thermochemical kinetics, and noncovalent interactions: The MPW1B95 and MPWB1K models and comparative assessments for hydrogen bonding and Van der Waals interactions*. Journal of Physical Chemistry A, 108 (**2004**) 6908-6918.

[28] Y. Zhao, D.G. Truhlar, *Density functionals with broad applicability in chemistry*. Accounts of Chemical Research, 41 (**2008**) 157-167.

[29] M.E. Arroyo-de Dompablo, A. Morales-Garcia, M. Taravillo, *DFT plus U calculations of crystal lattice, electronic structure, and phase stability under pressure of TiO_2 polymorphs*. Journal of Chemical Physics, 135 (**2011**) 054503.

[30] V.L. Chevrier, S.P. Ong, R. Armiento, M.K.Y. Chan, G. Ceder, *Hybrid density functional calculations of redox potentials and formation energies of transition metal compounds*. Physical Review B, 82 (**2010**) 075122.

[31] A. Emly, A. Van der Ven, *Mg intercalation in layered and spinel host crystal structures for Mg batteries*. Inorganic Chemistry, 54 (**2015**) 4394-4402.

[32] D.S. Tchitchekova, A. Ponrouch, R. Verrelli, T. Broux, C. Frontera, A. Sorrentino, F. Barde, N. Biskup, M. E. Arroyo-de Dompablo, M. Rosa Palacin, *Electrochemical intercalation of calcium and magnesium in TiS_2: Fundamental studies related to multivalent battery applications*. Chemistry of Materials, 30 (**2018**) 847-856.

[33] J. Carrasco, *Role of Van der Waals forces in thermodynamics and kinetics of layered transition metal oxide electrodes: Alkali and alkaline-earth ion insertion into V_2O_5.* Journal of Physical Chemistry C, 118 (**2014**) 19599-19607.

[34] J. Klimes, D.R. Bowler, A. Michaelides, *Chemical accuracy for the Van der Waals density functional*. Journal of Physics-Condensed Matter, 22 (**2010**) 022201.

[35] J. Klimes, D.R. Bowler, A. Michaelides, *Van der Waals density functionals applied to solids*. Physical Review B, 83 (**2011**) 195131.

[36] J. Klimes, A. Michaelides, *Perspective: Advances and challenges in treating Van der Waals dispersion forces in density functional theory*. Journal of Chemical Physics, 137 (**2012**) 120901.

[37] H. Hellman, *A new approximation method in the problem of many electrons*. The Journal of Chemical Physics, 3 (**1935**) 61.

[38] S.G. Louie, *Nonlinear ionic pseudopotentials in spin-density-functional calculations*. Physical Review B, 26 (**1982**) 1738-1742.

[39] C.L. Reis, J.M.P.L. Martins, *First-principles norm-conserving pseudopotential with explicit incorporation of semicore states*. Physical Review B, 68 (**2003**) 155111.

[40] M. Gajdos, K. Hummer, G. Kresse, J. Furthmuller, F. Bechstedt, *Linear optical properties in the projector-augmented wave methodology*. Physical Review B, 73 (**2006**) 045112.

[41] J.J. Mortensen, L.B. Hansen, K.W. Jacobsen, *Real-space grid implementation of the projector augmented wave method*. Physical Review B, 71 (**2005**) 035109.

[42] A. Belsky, M. Hellenbrandt, V.L. Karen, P. Luksch, *New developments in the inorganic crystal structure database (ICSD): Accessibility in support of materials research and design*. Acta Crystallographica Section B-Structural Science, 58 (**2002**) 364-369.

[43] M.K. Aydinol, A.F. Kohan, G. Ceder, K. Cho, J. Joannopoulos, *Ab initio study of lithium intercalation in metal oxides and metal dichalcogenides*. Physical Review B, 56 (**1997**) 1354-1365.

[44] P. Canepa, G.S. Gautam, D.C. Hannah, R. Malik, M. Liu, K.G. Gallagher, K.A. Persson, G. Ceder, *Odyssey of multivalent cathode materials: Open questions and future challenges*. Chem. Rev., 117 (**2017**) 4287-4341.

[45] Y.S. Meng, M. Elena Arroyo-de Dompablo, *First principles computational materials design for energy storage materials in lithium ion batteries*. Energy & Environmental Science, 2 (**2009**) 589-609.

[46] A. Van der Ven, J.C. Thomas, Q. Xu, B. Swoboda, J. Bhattacharga, *Linking the electronic structure of solids to their thermodynamic and kinetic properties*. Mathematical and Computers in Simulation, 80 (**2010**) 1393.

[47] T. Maxisch, F. Zhou, G. Ceder, *Ab initio study of the migration of small polarons in olivine Li_xFePO_4 and their association with lithium ions and vacancies*. Physical Review B, 73 (**2006**) 104301.

[48] Z. Deng, Y. Mo, S.P. Ong, *Computational studies of solid-state alkali conduction in rechargeable alkali-ion batteries*. Npg Asia Materials, 8 (**2016**) e254.

[49] D. Morgan, A. Van der Ven, G. Ceder, *Li conductivity in Li_xMPO_4 (M = Mn, Fe, Co, Ni) olivine materials*. Electrochemical and Solid State Letters, 7 (**2004**) A30-A32.

[50] G. Mills, H. Jonsson, G.K. Schenter, *Reversible work transition-state theory - application to dissociative adsorption of hydrogen*. Surface Science, 324 (**1995**) 305-337.

[51] G. Mills, G.K. Schenter, D.E. Makarov, H. Jonsson, *Generalized path integral based quantum transition state theory*. Chemical Physics Letters, 278 (**1997**) 91-96.

[52] G. Henkelman, B.P. Uberuaga, H. Jonsson, *A climbing image nudged elastic band method for finding saddle points and minimum energy paths*. Journal of Chemical Physics, 113 (**2000**) 9901-9904.

[53] D. Sheppard, R. Terrell, G. Henkelman, *Optimization methods for finding minimum energy paths*. Journal of Chemical Physics, 128 (**2008**) 134106.

[54] D. Sheppard, P. Xiao, W. Chemelewski, D.D. Johnson, G. Henkelman, *A generalized solid-state nudged elastic band method*. Journal of Chemical Physics, 136 (**2012**) 074103

[55] S.A. Trygubenko, D.J. Wales, *A doubly nudged elastic band method for finding transition states*. Journal of Chemical Physics, 120 (**2004**) 2082-2094.

[56] A. Torres, M.E. Arroyo-de Dompablo, *Comparative investigation of $MgMnSiO_4$ and olivine-type $MgMnSiS_4$ as cathode materials for mg batteries*. Journal of Physical Chemistry C, 122 (**2018**) 9356-9362.

[57] S.P. Ong, V.L. Chevrier, G. Hautier, A. Jain, C. Moore, S. Kim, X. Ma, G. Ceder, *Voltage, stability and diffusion barrier differences between sodium-ion and lithium-ion intercalation materials*. Energy & Environmental Science, 4 (**2011**) 3680-3688.

CAPÍTULO 3

ANÁLISIS DE MINERALES: CARBONATOS Y SILICATOS DE METALES DE TRANSICIÓN

www.nature.com/scientificreports

SCIENTIFIC REPORTS

OPEN

Analysis of Minerals as Electrode Materials for Ca-based Rechargeable Batteries

Received: 10 December 2018
Accepted: 18 June 2019
Published online: 04 July 2019

A. Torres[1], F. J. Luque[2,3], J. Tortajada[4] & M. E. Arroyo-de Dompablo[1]

Rechargeable lithium-ion batteries dominate the consumer electronics and electric vehicle markets. However, concerns on Li availability have prompted the development of alternative high energy density electrochemical energy storage systems. Rechargeable batteries based on a Ca metal anode can exhibit advantages in terms of energy density, safety and cost. The development of rechargeable Ca metal batteries requires the identification of suitable high specific energy cathode materials. This work focuses on Ca-bearing minerals because they represent stable and abundant compounds. Suitable minerals should contain a transition metal able of being reversibly reduced and oxidized, which points to several major classes of silicates and carbonates: olivine ($CaFeSiO_4$; kirschsteinite), pyroxene ($CaFe/MnSi_2O_6$; hedenbergite and johannsenite, respectively), garnet ($Ca_3Fe/Cr_2Si_3O_{12}$; andradite and uvarovite, respectively), amphibole ($Ca_2Fe_5Si_8O_{22}(OH)_2$; ferroactinolite) and double carbonates ($CaMn(CO_3)_2$; kutnahorite and $CaFe(CO_3)_2$; ankerite). This work discusses their electrode characteristics based on crystal chemistry analysis and density functional theory (DFT) calculations. The results indicate that upon Ca deintercalation, compounds such as pyroxene, garnet and double carbonate minerals could display high theoretical energy densities (ranging from 780 to 1500 Wh/kg) with moderate structural modifications. As a downside, DFT calculations indicate a hampered Ca mobility in their crystal structures. The overall analysis then disregards olivine, garnet, pyroxene, amphibole and double carbonates as structural types for future Ca-cathode materials design.

While the current state-of-the-art in rechargeable batteries is the Li-ion technology, research efforts are being intensified towards the development of alternative technologies to satisfy the ever-increasing demand for enhanced energy density and lower costs. This prompted the development of rechargeable batteries based on the more abundant and cheaper Ca, Mg and Al metals[1,2]. Like in the Li-ion technology, the operation of Ca or Mg batteries relies on a reversible intercalation reaction (see Fig. 1). During the discharge of the electrochemical cell, the mobile ion (Ca^{2+}/Mg^{2+}) moves from the metal anode and intercalates in the positive electrode, while the electrons flow across an external circuit (reduction of the cathode material). When charging the battery, the reactions are reversed as shown in Fig. 1. The energy density delivered by the electrochemical cell depends on both the electrochemical capacity and the operation potential. The capacity is governed by the ratio between the difference in inserted ion contents in the intercalated and deintercalated states of the positive electrode, and its overall formula weight. The operation potential depends on the nature of the redox centers (the intercalant ion and a transition metal element in the positive electrode). Batteries based on divalent charge carriers (Ca^{2+}, Mg^{2+}) can exhibit advantages in terms of energy density since for a certain amount of intercalated ions the expected capacity is doubled when compared to single valent carriers like Li^+ or Na^+. In addition, Ca offers a low reduction potential (only 0.3 V below Li), so operation voltages are similar in the Li and Ca intercalation chemistries.

Under the perspective of high specific energies (exceeding 600 Wh/kg positive electrode material), researchers from various disciplines have joined endeavors in the quest of suitable electrode and electrolytes for the emerging Ca technology. Although some promising results have been achieved, the identification of high specific energy

[1]Departamento de Química Inorgánica, Facultad de Cc. Químicas, Universidad Complutense de Madrid, 28040, Madrid, Spain. [2]Departamento de Mineralogía y Petrología, Facultad de Geología, Universidad Complutense de Madrid, 28040, Madrid, Spain. [3]Departamento Geomateriales, Instituto de Geociencias IGEO (CSIC, UCM), 28040, Madrid, Spain. [4]Departamento de Química Física, Facultad de Cc. Químicas, Universidad Complutense de Madrid, 28040, Madrid, Spain. Correspondence and requests for materials should be addressed to M.E.A. (email: e.arroyo@quim.ucm.es)

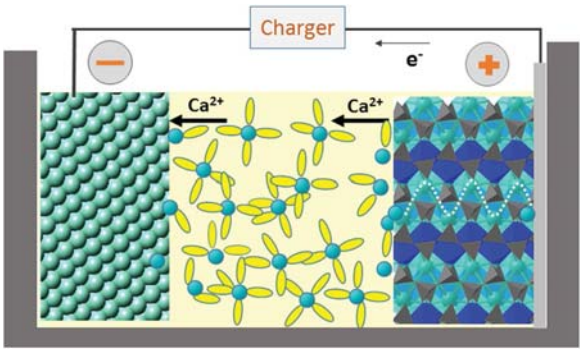

Figure 1. Scheme of a Ca-based battery using pyroxene as the positive electrode and Ca metal as the negative electrode. During the charge of the battery Ca ion are deinserted from the positive electrode and deposited in the Ca metal, and the electrons flow across the external circuit.

electrode materials remains a challenge[3–9]. Because minerals represent stable compounds in natural conditions, in this work we discuss the possible applications of Ca-bearing minerals as electrode materials for Ca-based batteries.

Calcium is the fifth element in abundance in the Earth's crust, representing around 3.65 wt.%[10]. This is therefore one of its main advantages respect to other elements (mainly Li) used in battery technology. In addition to plagioclase feldspars ($Na_{1-0}Ca_{0-1}Al_{1-2}Si_{3-2}O_8$), the most abundant calcium minerals are carbonates (calcite and aragonite, $CaCO_3$; dolomite, $CaMg(CO_3)_2$), that constitute about 2.5% of the crust[11], and sulfates (gypsum, $CaSO_4\,2H_2O$; anhydrite, $CaSO_4$). All these industrial minerals can be also used to obtain metallic calcium[12] which eventually forms the anode in the battery. The most common industrial procedure to obtain Ca metal is to treat the mineral with HCl to form $CaCl_2$ and a subsequent elecytrolisis process[13–15]. In addition, calcium metal is produced by an aluminothermic reduction process that begins with $CaCO_3$ calcined to form CaO[14,16,17]. It has been recently reported[18] that for a Li-ion battery the cost of elemental lithium (considering both the electrolyte and electrodes) is about 44 USD per kilowatt hour. This calculation was made according to the price of Li_2CO_3 in 2015 (about 6.5 USD/kg). The final price in the market for Ca metal in 2014 was about 4.3 USD/kg[14]. The current price of battery-grade Li_2CO_3 is close to 15 USD/kg, therefore much higher than the price of Ca metal. This supports the expected lower cost of the Ca-battery technology, assuming that all other components are equally affordable for both technologies. Additionally, the positive electrode material used in the highest energy density commercial Li-ion batteries contains nickel and cobalt (scarce metals), and this represents the major bottleneck for cost reduction. Reaching high energy densities utilizing Ni and Co free positive electrode materials is a key viewpoint in the calcium technology.

Minerals with potential application as positive electrode in the Ca-battery technology should contain a transition metal able of being reversibly reduced (cathode during the discharge of the cell) and oxidized (anode during the charge of the cell). Minerals containing both Ca and transition metals are by far less abundant than the above mentioned Ca-bearing minerals, and belong to the major classes of silicates and carbonates[19]. Due to size effects, Ca usually combines with Fe and Mn, and more rarely with Cr. Among the silicates, the interesting minerals would be within the olivine ($CaFeSiO_4$; kirschsteinite), pyroxene ($CaFe/MnSi_2O_6$; hedenbergite and johannsenite, respectively), garnet ($Ca_3Fe/Cr_2Si_3O_{12}$; andradite and uvarovite, respectively), and amphibole ($Ca_2Fe_5Si_8O_{22}(OH)_2$; ferroactinolite) groups. In addition to silicates, other minerals containing Ca and Mn/Fe are the dolomite-like structural counterparts kutnahorite ($CaMn(CO_3)_2$) and ankerite ($CaFe(CO_3)_2$). Along with intercalation voltage and specific capacity (which determine the specific energy), a good ionic diffusion ($D \sim 10^{-12}\,cm^2\,s^{-1}$) is a prerequisite for an electrode material. Indeed, one of the major concerns in the cathode design for the divalent battery technology is the limited mobility of Mg^{2+} and Ca^{2+} ions in inorganic structures. The migration energy barriers, which can be extracted from DFT calculations, provide an approximate estimate of the ionic diffusivity[20]. It has been estimated that for a reasonable cell power rate (discharging time 2 hours), the energy barriers for cation diffusion should be below 0.525 eV in micrometer particles and 0.625 eV in nanosized particles[3]. Previous computational works found appealing calculated energy barriers of 0.7 eV for some virtual CaM_2O_4 spinel with Ca occupying the tetrahedral sites[4]. Energy barriers above 1 eV are reported for perovskite and post-spinel transition metal oxides that actually resulted inactive as positive electrode in Ca cells[21,22]. Aiming to explore the potential of minerals as electrode material for Ca-batteries, after a rational pre-evaluation, we use DFT calculations to anticipate the relevant electrochemical characteristics of pyroxene, garnets and double carbonates.

Results

A simple analysis of chemical formulae and crystal structure serves to discard those minerals with low theoretical specific capacities or no pathways for Ca diffusion. So, a low specific capacity is expected for minerals of the amphibole group. The deintercalation of all Ca ions from this mineral structure would oxidize the Fe^{2+} ions to the formal oxidation state $Fe^{+2.8}$, according to the reaction:

$$Ca_2Fe_5Si_8O_{22}(OH)_2 \rightarrow 2\ Ca + Fe_5Si_8O_{22}(OH)_2 \quad (1)$$

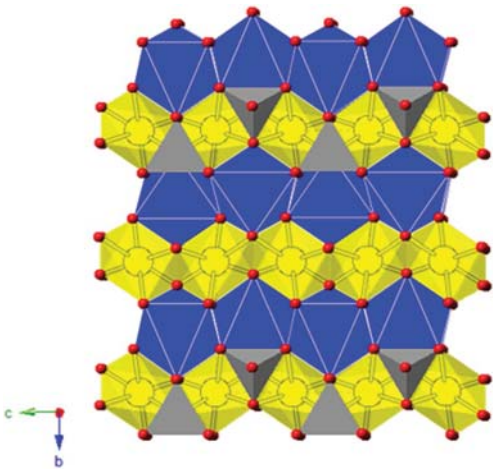

Figure 2. View of the olivine structure showing the octahedral M1 (in yellow) and M2 (in blue) sites, and tetrahedral Si (in grey). The M1 sites form channels for cation diffusion.

The expression for the maximum specific capacity delivered by the positive electrode material, can be written as:

$$C_s\left(\frac{mAh}{g}\right) = \frac{zyF}{3.6Wt} \quad (2)$$

where z is the charge of the intercalant ion (for Ca, z = 2), y the amount of inserted Ca (y = 2 for amphibole) and W_t is the formula weight of the mineral (801.6 g/mol in this case) Thus, the maximum theoretical capacity of $Ca_2Fe_5Si_8O_{22}(OH)_2$ is 133.7 mAh/g, by far too low for practical applications.

Olivine-$CaFeSiO_4$ would deliver a maximum theoretical capacity of 285 mAh/g upon Ca deintercalation (redox couple Fe^{2+}/Fe^{4+}). Noteworthy, olivine-type $LiFePO_4$ is currently used as positive electrode in commercial Li-ion batteries, and $MgMSiO_4$ (M = Fe, Mn) have been proposed as positive electrode for Mg batteries[20,23–25]. Figure 2 shows the crystal structure of olivine. It is usually described in terms of a hexagonal close-packing of oxygen with Mg and transition metal (Fe, Mn) ions located in half of the octahedral sites, and Si in one eight of the tetrahedral positions. The octahedral sites are further of two types, namely, M1 and M2. The M1 octahedron geometry is comparatively more distorted and smaller, whereas M2 octahedron is more regular and larger[26]. The M2 octahedra form a network of corner-sharing octahedra with low connectivity (in blue in Fig. 2). The M1 octahedra form edge-shared chains along the *c*-axis, providing a channel for cation diffusion (in yellow in Fig. 2). Contrary to the smaller Li and Mg ions, the Ca ions in kirschsteinite ($CaFeSiO_4$) occupy the M2 octahedral site[26,27]. With no diffusion pathways permitting Ca mobility, Ca-based olivines were discarded as electrode materials.

As detailed below, pyroxene, garnet and double carbonates have pathways for Ca diffusion and theoretical capacities exceeding 200 mAh/g. DFT provides a good description of their crystal structures with the differences between calculated and experimental lattice parameters being below 5% (see Table 1 in S.I.). The results for each mineral group are discussed below.

Pyroxene group. Most common natural pyroxenes are Fe/Mg-bearing silicates, with the general formula XYZ_2O_6. The Z cations correspond to Si^{4+}, with very minor substitution for Al^{3+}. Although pyroxene composition is quite variable (see Table 2 in S.I.), the most usual cations in natural pyroxenes are X = Mg^{2+}, Fe^{2+}, Ca^{2+}, Na^+ and Y = Mg^{2+}, Fe^{2+}, Al^{3+} [28,29]. The crystal structure of pyroxenes (Fig. 3) is characterized by single chains of $[SiO_4]^{4-}$ tetrahedra extending along the *c*-axis. In these chains, each tetrahedron shares two oxygens with their neighbours. As seen in the (001) projection of the structure (Fig. 3a), the chains are stacked atop each other in the *a*-axis direction in an alternating fashion, leading to two different sites: those located between the bases of tetrahedra (the M2 sites, in cyan) which contain the X cations in distorted 6-fold or 8-fold coordination, and those between unshared apical oxygens (the M1 octahedral sites occupied by the Y cations, in blue). The coordination of the M2 sites depends on how the chains are stacked and which cation occupies the site. When the cation is relatively small (e.g., Mg^{2+} or Fe^{2+}) the M2 site has octahedral coordination and the whole structure has orthorhombic symmetry (so, they are usually called orthopyroxenes). For larger cations (e. g., Ca^{2+}, Na^+) its coordination is 8-fold and the structure of the pyroxenes is monoclinic (clinopyroxenes). The M2 sites are interconnected forming a zig-zag channel for cation diffusion (Fig. 3b). Besides Fe, other transition metals (Mn, Ti) may occur in the M1 sites of natural pyroxenes in minor amounts. In addition, there are many reports on the preparation of a variety of synthetic pyroxenes with the general formula $CaM(SiO_3)_2$ (M = transition metal ion)[30–33].

The maximum theoretical capacity of $CaM(SiO_3)_2$ pyroxenes is around 215 mAh/g, following the full Ca deintercalation and concomitant oxidation of M^{2+} to M^{4+}. The average intercalation voltages of the Ca deintercalation

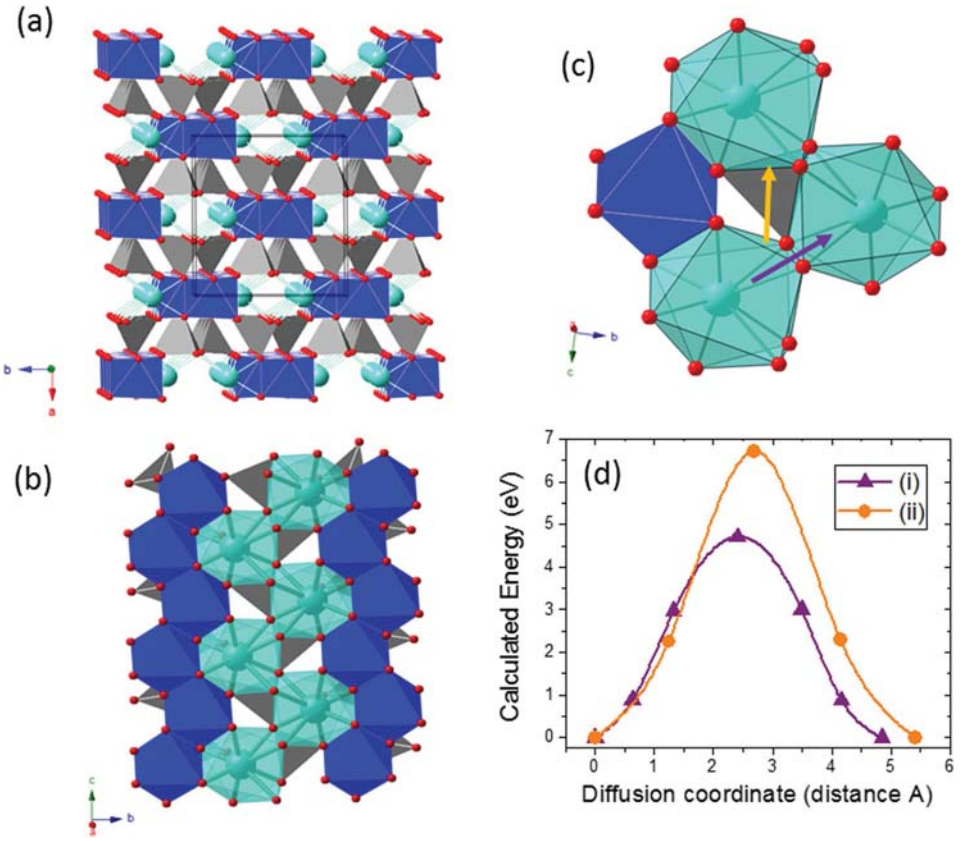

Figure 3. Analysis of the pyroxene minerals. (**a**,**b**) Crystal structure on (001) showing the chain arrangement and location of M1 sites (in dark blue) and M2 sites (in cyan). Note that both sites form rows of edge-sharing polyhedra along the c-axis. (**c**,**d**) Two possible pathways for Ca diffusion along the *c* axis in pyroxene $CaMn(SiO_3)_2$ and their corresponding calculated energy barriers. Color code: Ca cyan, Mn blue, Si grey, O red.

reaction can be obtained from the calculated total energy of the initial ($CaM(SiO_3)_2$ and deintercalated ($M(SiO_3)_2$) forms[34], according with equation (3):

$$V(V) = \frac{-E_{TOTAL}(Initial) + E_{TOTAL}(Deinterclated) + yE_{TOTAL}(Ca)}{2F} \quad (3)$$

Figure 4 compares the theoretical specific capacity, calculated volume variation, and intercalation voltage for various transition metals. Theoretical specific energies on the order of 800 mWh/g are expected for the pyroxene group. In addition, the deintercalation reaction cause limited changes in the crystal structure of Fe, Co and Ni pyroxenes (see Table 1 in S.I.), although sustainability and cost advocate the utilization of Mn.

Ca mobility in the pyroxene structure has been evaluated for $CaMn(SiO_3)_2$ using a $Ca_7Mn_8Si_{16}O_{48}$ supercell. The Ca ions in the rows of edge-sharing polyhedra along the *c*-axis are 5.3 Å apart. In the simplest hopping mechanism, a diffusing Ca ion can jump to a neighbouring vacant site by two different pathways: (i) across the common edge (purple arrow in Fig. 3c) and, (ii) across a triangular face via the occupation of a hexa-coordinated intermediate site (orange arrow, in Fig. 3c). The calculated energy barriers are, respectively, 4.6 eV and 6.8 eV. These large energy barriers are indicative of hindered Ca mobility. Figure 3d shows the energy landscapes associate to the hopping mechanism. The large energy barrier at the saddle point results from the very short cation-cation distances, this is to say, large electrostatic repulsions. In the intermediate site of path (i) the Ca^{2+}-Si^{4+} distance is of only 2.56 Å, to be compared with the initial Ca^{2+}-Si^{4+} distance of 3.12 Å. In path (ii) the intermediate hexa-coordinate site shares a face with the neighbouring Mn polyhedra (distance Ca^{2+}-Mn^{3+} = 2.54 Å), hence, a diffusing Ca ion occupying this site will suffer strong electrostatic repulsion.

Cation diffusion is primarily determined by the crystal structure. Previous computational investigations show that for a given family of compounds such as $LiMPO_4$, CaM_2O_4, MgM_2S_4 and so forth, the energy barrier expand in about 0.3 eV with the nature of the transition metal ion (M)[2,4,20,35]. Note that a 60 meV increase (decrease) in the migration energy corresponds to an order of magnitude decrease (increase) in diffusion coefficient[3]. Since the calculated energy barrier of $CaMn(SiO_3)_2$ is 4.6 eV, substitution of other transition metal for Mn is not expected

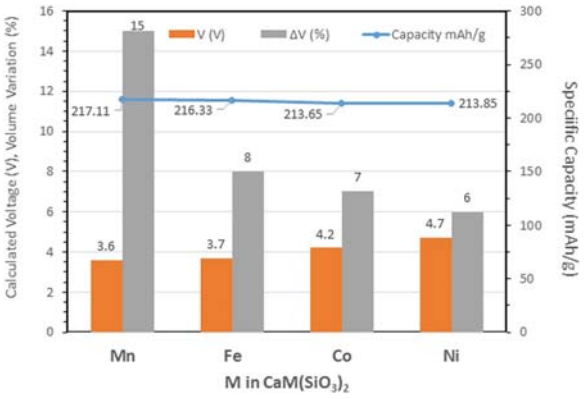

Figure 4. Calculated average voltage, volume variations and specific capacity associated within the pyroxene group. The volume variation is defined as $((V_{initial} - V_{deintercalated})/V_{initial}) * 100$.

to lower the energy barrier for Ca diffusion in pyroxenes below the acceptable threshold of 0.625 eV for nanosized particles to operate at C/2 rate.

Garnet group. The garnet group of rock-forming minerals can be defined as a multicomponent substitutional solid solution series of silicates with the general formula $X_3Y_2Si_3O_{12}$, where X is a divalent cation (Mg, Fe, Mn, and Ca, in the most common species) in 8-fold coordination and Y is a trivalent cation (Al, Fe, and Cr, in the most common species) in 6-fold coordination[36]. The structure of these silicate garnets (Fig. 5a) consists of isolated Si tetrahedra (in grey) sharing corners with the Y octahedra (in blue) to form chains along each of the *a* axes of a cubic cell. The spaces between chains are occupied by the X cations (in cyan) which are coordinated by eight oxygen atoms forming a triangular dodecahedron (i.e. distorted cube). Each dodecahedron is linked to other three forming a 3D network of sites in the structure (see Fig. 5b). In addition to these silicate garnets, the garnet supergroup[37] also includes minerals other than silicates and even those in which the anion is not oxygen (mainly OH^- groups or, more rarely, F^-). All these minerals, however, are isostructural with the most common rock-forming silicate garnets described above.

In the context of rechargeable batteries technologies it is important to note that some Li-bearing synthetic garnet-type oxides have received much attention in the last years[38–41]. In some cases, Li is in tetrahedral or octahedral coordination, but in other cases Li occupies additional crystallographic sites not available in the "standard" garnet structure[37,41]. Some of these "Li-stuffed" garnet-type oxides do not have cubic symmetry[41].

Regarding Ca-batteries, some garnets might be interesting as they contain transition elements in the octahedral and/or tetrahedral sites (Table 3 in S.I.), including both silicate garnets (of the schorlomite and garnet, s.s. groups) and oxide garnets (of the bitikleite group). Due to its relatively large ionic radius, Ca^{2+} is in the 8-fold coordination X site. Among the Ca-garnets, we have chosen uvarovite $Ca_3Cr_2(SiO_4)_3$ for which Ca deintercalation implies Cr^{3+} oxidation. For the Cr^{3+}/Cr^{6+} redox couple, the theoretical capacity is 321 mAh/g and the calculated average voltage 4.8 V. However, the instability of current electrolytes for Ca batteries beyond 4 V[7] limits the practical deliverable specific capacity of uvarovite.

The garnet structure possesses three-dimensional pathways for Ca diffusion; Fig. 5c shows a detail of three interconnected Ca sites. Figure 5d provides the calculated energy landscape for Ca ions hopping from one Ca site to the nearest one. A diffusing Ca ion must move from the initial site across a quadrangular face to fit in a trigonal prismatic (TP) site at the transition state. The calculated Ca-O distances in the quadrangular face and in the TP site range from 2.14 to 2.37 Å and from 2.13 to 2.51 Å, respectively. Having in mind the ionic radii, $r(Ca^{2+}) = 1.12$ Å and $r(O^{2-}) = 1.4$ Å, the Ca^{2+} ion seems too large for the size of the channel. Regarding the cationic repulsions, although the TP site shares a face with the octahedral chromium, the Ca-Cr^{3+} distance is 2.8 Å. This means that the cationic repulsion is lower than in the pyroxene structure, in agreement with its lower energy barrier of 2.07 eV (Fig. 5). However, this barrier is still too high for Ca mobility.

For the sake of completeness, we have calculated the energy barrier for migration in the garnet $Ca_3Mn_2(SiO_4)_3$ (theoretical capacity 105 mAh/g for the Mn^{3+}/Mn^{4+} redox couple). Compared to Cr^{3+}, the slightly larger and less polarizing High Spin-Mn^{3+} ($r(Mn^{3+})_{VI} = 0.645$ Å, $r(Cr^{3+})_{VI} = 0.615$ Å)[42] may diminish the electrostatic repulsion and expand the crystal structure to facilitate Ca diffusion (see Table 1 in S.I. for cell volume). Yet, the calculated energy is 2.09 eV. This corroborates the aforementioned observation of a subtle energy barrier variation with the nature of the transition metal.

Double carbonates. Natural carbonates with two cations (Ca + Mg/Fe/Mn/Zn) share a common structure type, usually defined as the dolomite ($CaMg(CO_3)_2$) structure. The dolomite structure may be considered to derive from that of calcite which, in turn, could be described as a derivative from the halite structure. Thus, compared to halite, in the calcite structure chlorine anions are substituted by the carbonate $(CO_3)^{2-}$ anionic groups and Na^+ cations by Ca^{2+}. The $(CO_3)^{2-}$ anionic groups form triangles in which each carbon is covalently bonded to three oxygens. Substitution of nearly-spherical chlorine anions by these planar groups results in a symmetry

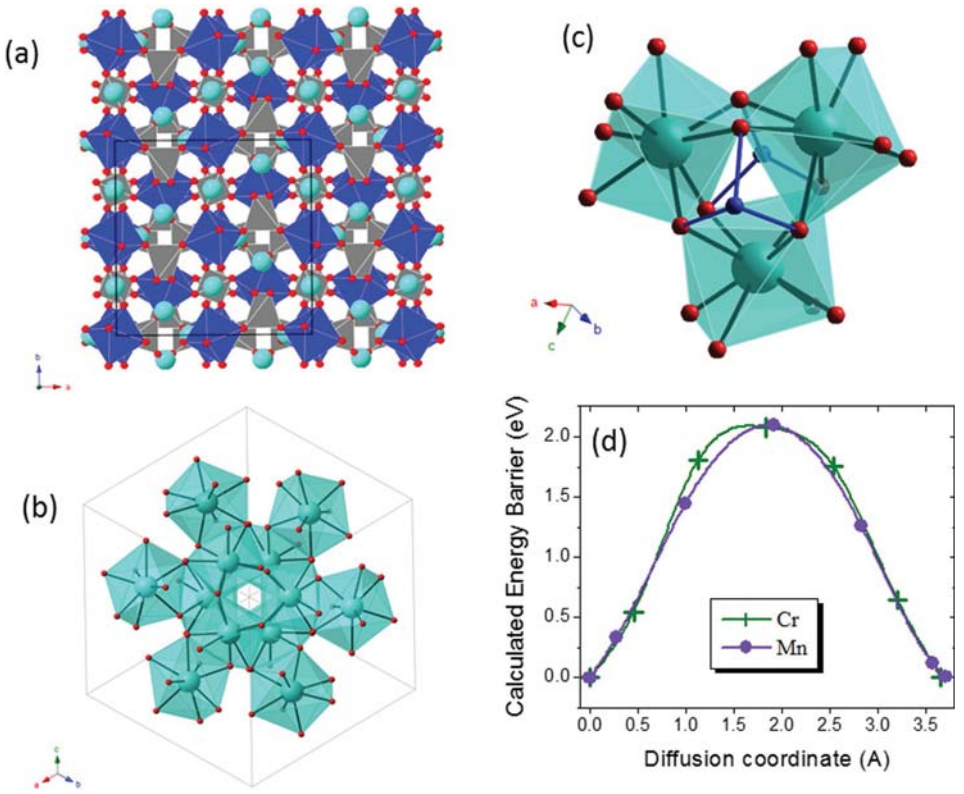

Figure 5. Analysis of garnet minerals. (**a**) The garnet structure along the [001] direction (**b**) Unit cell of the garnet structure showing the interconnected Ca sites forming a network for Ca diffusion. (**c**) Detail of the garnet structure showing three edge-sharing Ca dodecahedra. (**d**) Calculated energy barriers for Ca diffusion in garnet $Ca_3M_2(SiO_4)_3$ for M = Cr and Mn. Color code: Ca cyan, Cr/Mn blue, O red.

change from cubic to rhombohedral. This can be viewed as a shortening of the cubic cell along one of its largest diagonals (the 3-fold axis). Triangular $(CO_3)^{2-}$ groups are parallel and lie in horizontal layers perpendicular to this axis that becomes the *c*-axis; carbonate groups in adjacent layers, however, point in opposite directions. In the calcite structure, there are layers of $(CO_3)^{2-}$ groups and layers of Ca^{2+} cations which occupy 6-fold sites between the layers of the anionic groups. Compared to calcite structure, that of double carbonates shows an ordered arrangement of cations (Fig. 6a), because the structure must accommodate distinctly different-sized cations. In the idealized structure this is accomplished by having layers of Ca^{2+} alternating with layers of the smaller $(Mg/Fe/Mn/Zn)^{2+}$ cations. Such an ordered cation arrangement results in a symmetry reduction respect to that of the calcite structure.

Double-cation carbonate minerals correspond to dolomite ($CaMg(CO_3)_2$), ankerite ($CaFe(CO_3)_2$), kutnahorite ($CaMn(CO_3)_2$) and minrecordite ($CaZn(CO_3)_2$). Isomorphic replacement among cations other than Ca^{2+} is common in these minerals, especially in ankerite ($Ca(Fe,Mg)(CO_3)_2$) and kutnahorite ($Ca(Mn,Fe,Mg)(CO_3)_2$). In addition, disordered structures at low temperatures have also been reported (e.g., in kutnahorite[43]). These authors suggest that the large ionic radius of Mn^{2+} relative to Mg^{2+} in dolomite leads to coupled distortion of the Ca and Mn octahedra that may result in a low ordering potential.

Ankerite and kutnahorite are interesting minerals as electrode for Ca batteries. The present DFT results indicate that $CaMn(CO_3)_2$ reunites excellent electrode characteristics: theoretical specific capacity of 250 mAh/g, calculated average voltage of 3.8 V and volume variation of 13%.

A $Ca_{11}Mn_{12}C_{24}O_{72}$ supercell has been used to study Ca diffusion in kutnahorite. As seen in Fig. 6b, the calcium ions occupy octahedral sites with oxygen at a distance of 2.36 Å. In the *ab* plane, each Ca has six equivalent Ca-neighbours at a distance of 4.89 Å. Although the Ca-O polyhedra are not interconnected, the arrow in Fig. 6c indicates the possible pathway for in-plane conductivity. In this path, the Ca ion moves from its initial site across a triangular face to fit in the intermediate distorted octahedral site and then reach the final Ca site. Nudged Elastic Band method (NEB) calculations have been performed for this path considering 5 and 10 intermediate images (Fig. 6d). The Ca ions at the saddle point resides in four-coordinated site only 2.51 Å apart from the central C atom of the nearest carbonate groups. Unfortunately, the calculated energy barrier is 2.8 eV, excluding the potential interest of double carbonates as electrode materials for Ca batteries.

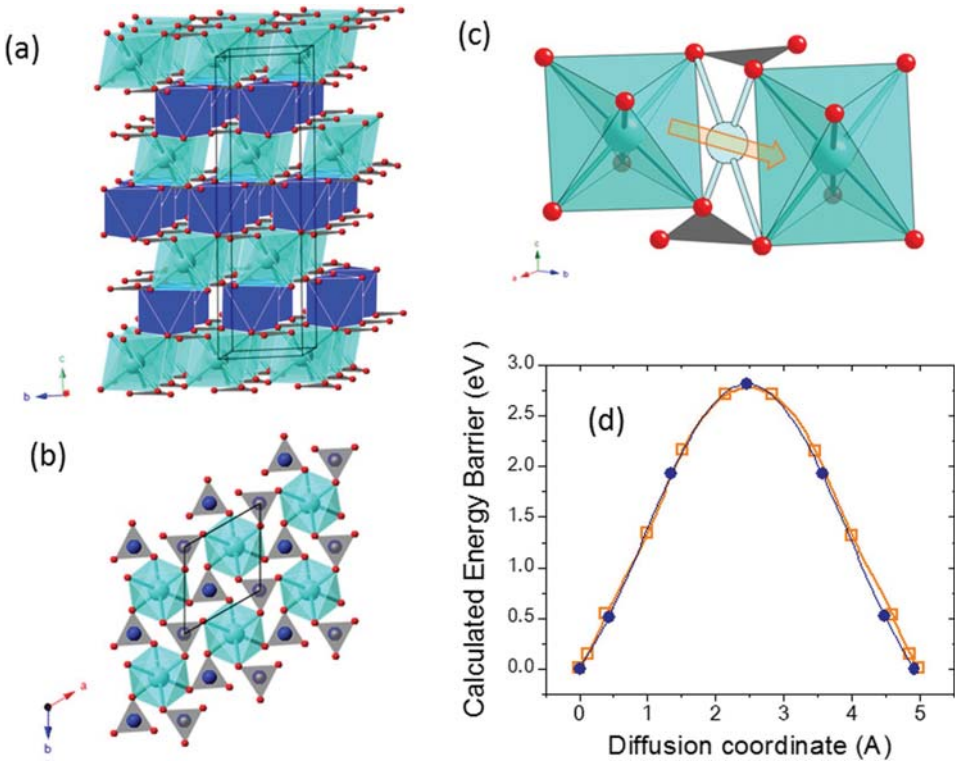

Figure 6. Analysis of double carbonates. (**a**) Crystal structure of $CaMn(CO_3)_2$ where M and Ca are ordered in alternate planes along the *c* axis of the hexagonal cell. (**b**) View of the Ca distribution in the *ab* plane. (**c**) Two neighbouring Ca sites in $CaMn(CO_3)_2$. The arrow indicates the pathway for Ca diffusion and the intermediate four-fold coordinated site. (**d**) Calculated energy barriers for Ca diffusion in kutnahorite with 5 and 10 intermediate images. Color code: Ca cyan, Mn blue, C grey, O red.

Discussion

Ca-bearing minerals combined with transition metals capable of being oxidized/reduced belong to various major mineral groups: olivine, amphibole, pyroxene, garnet and dolomite. Each mineral group has a chemical composition and crystal structure that determine the basic electrode characteristics, and eventually, the potential interest of these minerals as electrode materials for Ca batteries. Paradoxically, although one of the Li-cathode materials currently used in commercial batteries ($LiFePO_4$) has the olivine structure, such a structure is not suitable for the Ca intercalation chemistry. For the other mineral groups, the chemical composition and the nature of the transition metal ions dictate the specific capacity and control the intercalation voltage. With the exception of the amphibole group, large specific capacities and voltages are predicted for the above mentioned Ca transition metal-bearing minerals.

Table 1 summarizes the calculated electrode characteristics for representative pyroxene, garnet and double carbonates minerals: average intercalation voltages, volume variation, energies barriers for Ca diffusion and band-gap for electronic conductivity. Band-gaps are extracted from the calculated density of states (see Fig. 1 in S.I.). These minerals display high theoretical energy densities with predicted moderate structural modifications. Their low electrical conductivity (electronic and ionic) is the main concern in terms of applications, as the electrical conductivity will determine the power and rate capability of the Ca battery. Particle size minimization (nanosizing) and intimate carbon coating is a strategy to improve the electronic conductivity, a typical example being the insulating $LiFePO_4$ material (band-gap 3.5 eV)[20,44–47]. Nanostructuring is also a common route to mitigate poor ionic diffusion in electrodes[48–50]. Ceder *et al.* have estimated the relationship between the migration energy barrier and the maximum particle size permitting reasonable diffusivity in the context of battery performance[2,3]. For a given (dis)charge time, the cathode particle size will determine a maximum tolerable energy barrier for Ca migration. According to reference[2], for a low rate performance (large (dis)charging time of 10 h) the energy barrier can be at most ~0.6 meV when using a micron-sized particle and ~0.9 meV in a nanosized particle (at 298 K). While these values demonstrate the potential importance of nanosizing to enhance rate capability, they also indicate that materials with very low intrinsic Ca diffusivity (energy barriers exceeding 1 eV) are not viable as electrodes, even at the nanoscale. That is the case of the investigated minerals, whose energy barriers exceeding 2 eV exclude practical applications.

Factors controlling Ca diffusion depend on crystal structure. The garnet, pyroxene and dolomite mineral groups possess suitable Ca migration pathways within the structure, but the local topology hampers Ca mobility.

GROUP	Pyroxene	Garnet	Dolomite
COMPOSITION	$CaMn(SiO_3)_2$	$Ca_3Cr_2(SiO_4)_3$	$CaMn(CO_3)_2$
REDOX COUPLE	Mn^{2+}/Mn^{4+}	Cr^{3+}/Cr^{6+}	Mn^{2+}/Mn^{4+}
CAPACITY (mAh/g)	217	321	250
AVERAGE VOLTAGE (V)	3.6	4.8	3.8
ENERGY (mWh/g)	780	1540	950
VOLUME INCREMENT (%)	15	14	13
DIFFUSSION BARRIER (eV)	4.6	2.1	2.8
BAND GAP (eV)	3.4	3	3.8

Table 1. Computed properties (voltage, volume variation and energy barrier for Ca diffusion) of Ca-bearing transition metal minerals. The theoretical specific capacity for the corresponding redox couple is indicated.

The garnet structure is well known for fast Li ion conductors, yet we found the pathways are too narrow for the large Ca ion. A general observation is the strong electrostatic interactions between the diffusing Ca^{2+} and the other cations (transition metal and central atom of the polyanionic groups) in the lattice. Generally speaking, the calculated energy barriers for Ca diffusion in minerals are larger than those reported in transition metal oxides[21,22,51]. A possible reason is the higher concentration of cations in these polyanionic structures, arising from the transition metals and the silicate/carbonate groups. Under this assumption, not only existing minerals, but also synthetic materials that emulate their crystal structures are not appealing as electrode materials for Ca batteries.

Regardless the usefulness of Ca-bearing minerals as positive electrode for Ca batteries, we should underline the importance of the abundant sulfate and carbonate mineral groups as the primary source for the Ca metal anode, which in the end sustain the interest of this technology, cheaper than that based on the Li-ion. As for the cathode side, so far TiS_2 appears as a sustainable option (voltage ~1.8 V, specific capacity 240 mAh/g, energy barrier 0.7 eV)[8], and an intensive DFT scrutiny is underway to identify oxides based on abundant transition metal ions.

Methods

The calculations have been performed using the ab-initio total-energy and molecular dynamics program VASP (Vienna ab-initio simulation program) developed at the Universität Wien[52]. Total energy calculations based on DFT were performed within the General Gradient Approximation (GGA), with the exchange and correlation functional form developed by Perdew, Burke, and Ernzerhof (PBE)[53]. The interaction of core electrons with the nuclei is described by the Projector Augmented Wave (PAW) method[54]. The energy cut off for the plane wave basis set was kept fix at a constant value of 600 eV throughout the calculations. The integration in the Brillouin zone is done on an appropriate set of k-points determined by the Monkhorts-Pack scheme. A convergence of the total energy close to 10 meV per formula unit is achieved with such parameters. Spin polarized calculations were performed in all cases. Previous computational works demonstrate that accurate intercalation voltage prediction for polyoxoanionic compounds (silicates, phosphate, vanadates and so forth) requires introducing a Hubbard correction term in the calculation[55–57]. In this work, the total energies of the GGA-optimized compounds have been calculated using the GGA + U method, following the simplified rotationally invariant form of Dudarev *et al.*[58] with U effective values of 3.7 eV (Cr), 4 eV (Mn), 5.3 eV (Fe), 3 eV (Co) and 6.9 eV (Ni) for the d-states of transition metal ions. The crystal models for the deintercalated phases were constructed removing all the Ca ions from the optimized structure of the initial minerals ($CaMn(SiO_3)_2$[59], $Ca_3Cr_2(SiO_4)_3$[60], $Ca_3Mn_2(SiO_4)_3$[61], $CaMn(CO_3)_2$[43]). All crystal structures were fully relaxed (atomic positions, cell parameters and volume). The final energies of the optimized geometries were recalculated so as to correct the changes in the basis set of wave functions during relaxation.

Ca^{2+} mobility in selected minerals was investigated using the NEB method as implemented in VASP. NEB calculations have been carried out at the dilute limit x ~ 1, that is, the migration of a single vacancy in an otherwise fully inserted structure. To attain the dilute limit, we used superstructures of the unit cell that guarantees a minimum interaction between defects. Constant volume calculations were performed within the GGA approximation for five intermediate images initialized by linear interpolation between the two fully relaxed end points.

Data Availability

The data that support the findings of this study are available from the corresponding authors upon reasonable request.

References

1. Muldoon, J., Bucur, C. B. & Gregory, T. Quest for nonaqueous multivalent secondary batteries: Magnesium and beyond. *Chem. Rev.* **114**, 11683–11720 (2014).
2. Canepa, P. *et al.* Odyssey of multivalent cathode materials: Open questions and future challenges. *Chem. Rev.* **117**, 4287–4341 (2017).
3. Rong, Z. *et al.* Materials design rules for multivalent ion mobility in intercalation structures. *Chem. Mater.* **27**, 6016–6021 (2015).
4. Liu, M. *et al.* Spinel compounds as multivalent battery cathodes: A systematic evaluation based on ab initio calculations. *Energy Environ. Sci.* **8**, 964–974 (2015).
5. Cabello, M. *et al.* Advancing towards a veritable calcium-ion battery: $CaCo_2O_4$ positive electrode material. *Electrochem. Comm.* **67**, 59–64 (2016).

6. Cabello, M. *et al*. Applicability of molybdite as an electrode material in calcium batteries: A structural study of layer-type Ca_xMoO_3. *Chem. Mater.* **30**, 5853–5861 (2018).
7. Ponrouch, A., Frontera, C., Barde, F. & Palacin, M. R. Towards a calcium-based rechargeable battery. *Nat. Mater.* **15**, 169–172 (2015).
8. Tchitchekova, D. S. *et al*. Electrochemical intercalation of calcium and magnesium in TiS_2: Fundamental studies related to multivalent battery applications. *Chem. Mater.* **30**, 847–856 (2018).
9. Lipson, A. L. *et al*. Rechargable Ca-ion batteries; a new energy storage system. *Chem. Mater.* **27**, 8442–8447 (2015).
10. Dill, H. G. The "chessboard" classification scheme of mineral deposits: Mineralogy and geology from aluminum to zirconium. *Earth-Sci. Rev.* **100**, 1–420 (2010).
11. Wenk, H.-R. & Bulakh, A. Minerals. Their constitution and origin (Cambridge University Press, 2016).
12. Sokić, M. *et al*. The possibilities of obtaining metallic calcium from serbian carbonate mineral raw materials. *Chem. Ind. Chem. Eng. Q.* **20**, 397–405 (2014).
13. Lukasko, J. J. & Murphy, J. E. Electrolytic production of calcium metal. Report of investigations #9315, Bureau of Mines, United States Department of the Interior (1990).
14. Neelameggham, N. R., Brown, R. E. & Davis, B. R. Calcium reductants – a historical review in *Rare metal technology 2014* (ed. Neelameggham, N. R. *et al.*) 67–76 (John Willey & Sons, 2014).
15. Zaikov, Y. P., Batukhtin, V. P., Shurov, N. I., Ivanovskii, L. E. & Suzdaltsev, A. V. Calcium production by the electrolysis of molten $CaCl_2$— Part I. Interaction of calcium and copper-calcium alloy with electrolyte. *Metall. Mater. Trans. B* **45**, 961–967 (2014).
16. Loomis, C. C. The production of metallic calcium by thermal reduction. *J. Electrochem. Soc.* **89**, 207–216 (1946).
17. Hibbins, S. G. Calcium and calcium alloys in *Encyclopedia of chemical technology* (ed. Kirk-Othmer, R.E.), 777–786 (John Wiley & Sons, 1992).
18. Vaalma, C., Buchholz, D., Weil, M. & Passerini, S. A cost and resource analysis of sodium-ion batteries. *Nat. Rev. Mater.* **3**, 18013 (2018).
19. Deer, R. A., Howie, J. & Zussman, W. An introduction to the rock-forming minerals (Mineralogical Society of Great Britain and Ireland, 2013).
20. Morgan, D., Van der Ven, A. & Ceder, G. Li conductivity in Li_xMPO_4 (M = Mn, Fe, Co, Ni) olivine materials. *Electrochem. Solid State Lett.* **7**, A30–A32 (2004).
21. Arroyo-de Dompablo, M. E., Krich, C., Nava-Avendaño, J., Palacín, M. R. & Bardé, F. In quest of cathode materials for Ca-ion batteries: The $CaMO_3$ perovskites (M = Mo, Cr, Mn, Fe, Co, Ni). *Phys. Chem. Chem. Phys.* **18**, 19966–19972 (2016).
22. Arroyo-de Dompablo, M. E. *et al*. A joint computational and experimental evaluation of $CaMn_2O_4$ polymorphs as cathode materials for Ca-ion batteries. *Chem. Mater.* **28**, 6886–6893 (2016).
23. Ling, C., Banerjee, D., Song, W., Zhang, M. & Matsui, M. First-principles study of the magnesiation of olivines: Redox reaction mechanism, electrochemical and thermodynamic properties. *J. Mater. Chem.* **22**, 13517–13523 (2012).
24. Mori, T. *et al*. Anti-site mixing governs the electrochemical performances of olivine-type $MgMnSiO_4$ cathodes for rechargeable magnesium batteries. *Phys. Chem. Chem. Phys.* **18**, 13524–13529 (2016).
25. Torres, A. & Arroyo-de Dompablo, M. E. Comparative investigation of $MgMnSiO_4$ and olivine-type $MgMnSiS_4$ as cathode materials for Mg batteries. *J. Phys. Chem. C* **122**, 9356–9362 (2018).
26. Brown, G. E. Olivines and silicate spinels in *Orthosilicates, 2nd edn. (ed. Ribbe, P.H.). Rev. Mineral.* **5**, 275–381 (Mineralogical Society of America, 1980).
27. Folco, L. & Mellini, M. Crystal chemistry of meteoritic kirschsteinite. *Eur. J. Mineral.* **9**, 969–973 (1997).
28. Cameron, M. & Papike, J. J. Crystal chemistry of silicate pyroxenes in *Pyroxenes (ed. Prewitt, C. T.). Rev. Mineral.* **7**, 5–92 (Mineralogical Society of America, 1980).
29. Morimoto, N. *et al*. Nomenclature of pyroxenes. *Am. Mineral.* **73**, 1123–1133 (1988).
30. Mantovani, L., Tribaudino, M., Mezzadri, F., Calestani, G. & Bromiley, G. The structure of $(Ca,Co)CoSi_2O_6$ pyroxenes and the Ca-M^{2+} substitution in $(Ca,M^{2+})M^{2+}Si_2O_6$ pyroxenes (M^{2+} = Co, Fe, Mg). *Am. Mineral.* **98**, 1241–1252 (2013).
31. Mantovani, L., Tribaudino, M., Bertoni, G., Salviati, G. & Bromiley, G. Solid solutions and phase transitions in $(Ca,M^{2+})M^{2+}Si_2O_6$ pyroxenes (M^{2+} = Co, Fe, Mg). *Am. Mineral.* **99**, 704–711 (2014).
32. Durand, G., Vilminot, S., Rabu, P., Derory, A. & Lambour, J. P. Synthesis, structure, and magnetic properties of $CaMSi_2O_6$ (M = Co, Ni) compounds and their solid solutions. *J. Solid State Chem.* **124**, 374–380 (1996).
33. Raudsepp, M., Hawthorne, F. C. & Turnock, A. C. Crystal chemistry of synthetic pyroxenes on the join $CaNiSi_2O_6$-$CaMgSi_2O_6$ (diopside): A Rietveld refinement study. *Am. Mineral.* **75**, 1274–1281 (1990).
34. Aydinol, M. K., Kohan, A. F., Ceder, G., Cho, K. & Joannopoulos, J. Ab initio study of lithium intercalation in metal oxides and metal dichalcogenides. *Phys. Rev. B* **56**, 1354–1365 (1997).
35. Liu, M. *et al*. Evaluation of sulfur spinel compounds for multivalent battery cathode applications. *Energy Environ. Sci.* **9**, 3201–3209 (2016).
36. Meagher, E. P. Silicate garnets in *Orthosilicates* (*ed. Ribbe, P. H.*). *Rev. Mineral.* **5**, 25–66 (*Mineralogical Society of America,* 1980).
37. Grew, E. S. *et al*. Nomenclature of the garnet supergroup. *Am. Mineral.* **98**, 785–811 (2013).
38. Baxter, E. F., Caddick, M. J. & Ague, J. J. Garnet: Common mineral, uncommonly useful. *Elements* **9**, 415–419 (2013).
39. Geiger, C. A. *et al*. Crystal chemistry and stability of "$Li_7La_3Zr_2O_{12}$" garnet: A fast lithium ion conductor. *Inorg. Chem.* **50**, 1089–1097 (2011).
40. Geiger, C. A. Garnet: A key phase in nature, the laboratory, and technology. *Elements* **9**, 447–452 (2013).
41. Thangadurai, V., Narayanan, S. & Pinzaru, D. Garnet-type solid-state fast Li ion conductors for Li batteries: Critical review. *Chem. Soc. Rev.* **43**, 4714–4727 (2014).
42. Shannon, R. D. & Prewitt, C. T. Revised effective ionic radii in halides and chalcogenides. *Acta Cryst.* **32**, 751–767 (1976).
43. Peacor, D. R., Essene, E. J. & Gaines, A. M. Petrologic and crystal-chemical implications of cation order-disorder in kutnahorite $CaMn(CO_3)_2$. *Am. Mineral.* **72**, 319–328 (1987).
44. Zhou, F., Kang, K. S., Maxisch, T., Ceder, G. & Morgan, D. The electronic structure and band gap of $LiFePO_4$ and $LiMnPO_4$. *Solid State Commun.* **132**, 181–186 (2004).
45. Li, H. Q. & Zhou, H. S. Enhancing the performances of Li-ion batteries by carbon-coating: Present and future. *Chem. Commun.* **48**, 1201–1217 (2012).
46. Zhang, W.-M., Wu, X.-L., Hu, J.-S., Guo, Y.-G. & Wan, L.-J. Carbon coated Fe_3O_4 nanospindles as a superior anode material for lithium-ion batteries. *Adv. Funct. Mater.* **18**, 3941–3946 (2008).
47. Yuan, L.-X. *et al*. Development and challenges of $LiFePO_4$ cathode material for lithium-ion batteries. *Energy Environ. Sci.* **4**, 269–284 (2011).
48. Yu, X. *et al*. A size-dependent sodium storage mechanism in $Li_4Ti_5O_{12}$ investigated by,a novel characterization technique combining *in situ* x-ray diffraction and chemical sodiation. *Nano Lett.* **13**, 4721–4727 (2013).
49. Wagemaker, M. *et al*. The influence of size on phase morphology and Li-ion mobility in nanosized lithiated anatase TiO_2. *Chem. - Eur. J.* **13**, 2023–2028 (2007).
50. Okubo, M. *et al*. Nanosize effect on high-rate Li-ion intercalation in $LiCoO_2$ electrode. *J. Am. Chem. Soc.* **129**, 7444–7452 (2007).
51. Gautam, G. S. *et al*. First-principles evaluation of multi-valent cation insertion into orthorhombic V_2O_5. *Chem. Commun.* **51**, 13619–13622 (2015).

52. Kresse, G. & Furthmuller, J. Efficient iterative schemes for ab initio total-energy calculations using a plane-wave basis set. *Phys. Rev. B* **54**, 11169 (1996).
53. Perdew, J. P., Burke, K. & Ernzerhof, M. Generalized gradient approximation made simple. *Phys. Rev. Lett.* **77**, 3865–3868 (1996).
54. Blöch, P. E. Projector augmented-wave method. *Phys. Rev. B* **50**, 17953 (1994).
55. Arroyo-de Dompablo, M. E., Rozier, P., Morcrette, M. & Tarascon, J. M. Electrochemical data transferability within Li_yVOXO_4 (X = Si, $Ge_{0.5}Si_{0.5}$, Ge, $Si_{0.5}As_{0.5}$, $Si_{0.5}P_{0.5}$, As, P) polyoxyanionic compounds. *Chem. Mater.* **19**, 2411–2422 (2007).
56. Meng, Y. S. & Arroyo-de Dompablo, M. E. Recent advances in first principles computational research of cathode materials for lithium-ion batteries. *Accounts Chem. Res.* **46**, 1171–1180 (2013).
57. Zhou, F., Cococcioni, M., Marianetti, C. A., Morgan, D. & Ceder, G. First-principles prediction of redox potentials in transition-metal compounds with LDA + *U*. *Phys. Rev. B* **70,** 235121 (2004).
58. Dudarev, S. L. *et al*. Electronic structure and elastic properties of strongly correlated metal oxides from first principles: LSDA + *U*, SIC-LSDA and EELS study of UO_2 and NiO. *Phys. Status Solidi A* **166**, 429–443 (1998).
59. Nestola, F., Ballaran, T. B., Angel, R. J., Zhao, J. & Ohashi, H. High-pressure behavior of Ca/Na clinopyroxenes: The effect of divalent and trivalent 3d-transition elements. *Am. Mineral.* **95**, 832–838 (2010).
60. Menzer, G. The crystal structure of garnets. *Z. Kristallogr.* **69**, 300–396 (1928).
61. Novak, G. A. & Gibbs, G. V. The crystal chemistry of the silicate garnets. *Am. Mineral.* **56**, 791–823 (1971).

Acknowledgements

Funding from the European Union's Horizon 2020 research and innovation programme H2020 FETOPEN-1-2016-2017 (CARBAT, grant agreement no. 766617) is acknowledged. The authors are grateful for access to the computational facilities from Universidad de Oviedo (MALTA-Consolider cluster).

Author Contributions

A. Torres and M.E. Arroyo-de Dompablo performed the DFT calculations, analysed the data and elaborated the results. F. J. Luque contributed to organize the crystallographic information and guided the mineral search. J. Tortajada conducted the development of computational tools and assisted in data analysis. All authors contributed to writing the article.

Additional Information

Supplementary information accompanies this paper at https://doi.org/10.1038/s41598-019-46002-4.

Competing Interests: The authors declare no competing interests.

Publisher's note: Springer Nature remains neutral with regard to jurisdictional claims in published maps and institutional affiliations.

Supplementary Information

Analysis of Minerals as Electrode Materials for Ca-based Rechargeable Batteries

A. Torres[1], F. J. Luque[2,3], J. Tortajada[4] and M. E. Arroyo-de Dompablo[1*]

1 Departamento de Química Inorgánica, Universidad Complutense de Madrid, 28040 Madrid (Spain).

2 Dpto. de Mineralogía y Petrología, Facultad de Geología, Universidad Complutense de Madrid, 28040 Madrid (Spain).

3 Dpto. Geomateriales, Instituto de Geociencias IGEO (CSIC, UCM), 28040 Madrid (Spain).

4 Departamento de Química Física, Universidad Complutense de Madrid, 28040 Madrid (Spain).

*Corresponding author: e.arroyo@quim.ucm.es

Table 1. Calculated lattice parameters and comparison with available experimental values

COMPOSITION	*a* (Å)	*b* (Å)	*c* (Å)	β / γ (º)	Volume (Å^3)
PYROXENE					
$CaMn(SiO_3)_2$	10.058	9.242	5.343	105.299	479.19
Experimental[1]	9.9227(3)	9.1416(3)	5.2745(2)	105.087(3)	461.96
$Mn(SiO_3)_2$	9.502	8.559	5.327	110.443	406.02
$CaFe(SiO_3)_2$	10.035	9.043	5.329	105.183	466.74
Experimental[2]	9.845(1)	9.024(1)	5.245(1)	104.74(1)	450.64
$Fe(SiO_3)_2$	9.678	8.738	5.352	109.084	427.74
$CaCo(SiO_3)_2$	9.930	9.034	5.316	105.910	458.66
Experimental[3]	9.7970(4)	8.9577(4)	5.2445(2)	105.513(3)	443.48
$Co(SiO_3)_2$	9.671	8.710	5.349	109.430	424.90
$CaNi(SiO_3)_2$	9.864	8.959	5.294	106.231	449.22
Experimental[4]	9.7359(4)	8.8932(4)	5.2284(3)	105.803(3)	435.52
$Ni(SiO_3)_2$	9.891	8.708	5.285	111.620	423.25
GARNET					
$Ca_3Cr_2(SiO_4)_3$	12.153	12.153	12.153		1795.27
Experimental[5]	11.950(3)	11.95	11.95		1706.49
$Cr_2(SiO_4)_3$	11.576	11.576	11.576		1551.44
$Ca_3Mn_2(SiO_4)_3$	12.228	12.228	12.228		1828.55
Experimental[6]	12.07	12.07	12.07		1758.42
DOLOMITE					
$CaMn(CO_3)_2$	4.936	4.936	16.544	120	349.14
Experimental[7]	4.894	4.894	16.500	120	342.25
$Mn(CO_3)_2$	4.668	4.668	16.142	120	304.61

Table 2. Cation occupancy of structural sites in pyroxene minerals[8]

Group	***X cations (M2)***	***Y cations (M1)***	***Z cations***	***Symmetry***
Magnesium-iron	Mg^{2+}, Fe^{2+}	Mg^{2+}, Fe^{2+}	Si^{4+}	Orthorhombic
Calcium	Ca^{2+}, (Mg^{2+}, Fe^{2+})	Mg^{2+}, Fe^{2+}, Al^{3+}	Si^{4+}, Al^{3+}	Monoclinic
Calcium-sodium	Ca^{2+}, Na^{+}	Mg^{2+}, Fe^{2+}, Al^{3+}, Fe^{3+}	Si^{4+}	
Sodium	Na^{+}	Al^{3+}, Fe^{3+}	Si^{4+}	
Lithium	Li^{+}	Al^{3+}	Si^{4+}	

Table 3. Ca-bearing garnets (adapted from [9] and AMCSD data base)

Group	***Class***	***Mineral***
BITIKLEITE	Oxide	Bitikleite $Ca_3\ Sb^{5+}Sn^{4+}\ Al_3\ O_{12}$
		Usturite $Ca_3\ Sb^{5+}Zr\ Fe^{3+}{}_3\ O_{12}$
		Dzhuluite $Ca_3\ Sb^{5+}Sn^{4+}\ Fe^{3+}{}_3\ O_{12}$
		Elbrusite $Ca_3\ U^{6+}{}_{0.5}Zr_{1.5}\ Fe^{3+}{}_3\ O_{12}$
SCHORLOMITE	Silicate	Schorlomite $Ca_3\ Ti_2\ SiFe^{3+}{}_2\ O_{12}$
		Irinarassite $Ca_3\ Sn^{4+}{}_2\ SiAl_2\ O_{12}$
		Toturite $Ca_3\ Sn^{4+}{}_2\ SiFe^{3+}{}_2\ O_{12}$
GARNET	Silicate	Andradite $Ca_3\ Fe^{3+}{}_2\ Si_3\ O_{12}$
		Uvarovite $Ca_3\ Cr^{3+}{}_2\ Si_3\ O_{12}$
		Goldmanite $Ca_3\ V^{3+}{}_2\ Si_3\ O_{12}$
		Morimotoite $Ca_3\ TiFe^{2+}\ Si_3\ O_{12}$

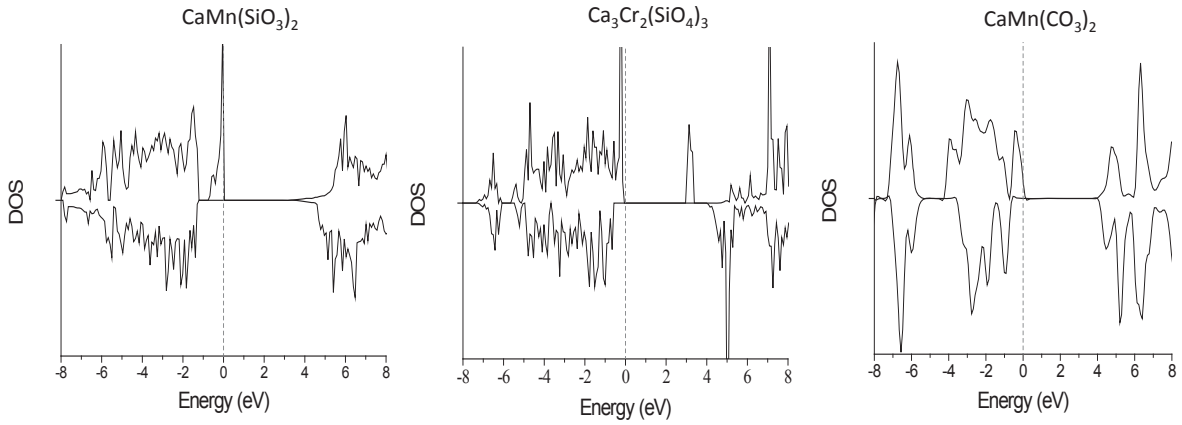

Figure 1. Calculated density of states (DOS) for representative pyroxene, garnet and dolomite-like minerals. The Fermi level is set as the zero of energy.

References

1 Nestola, F., Ballaran, T. B., Angel, R. J., Zhao, J. & Ohashi, H. High-pressure behavior of Ca/Na clinopyroxenes: The effect of divalent and trivalent 3d-transition elements. *American Mineralogist* **95**, 832-838 (2010).

2 Cameron, M., Sueno, S., Prewitt, C. T. & Papike, J. J. High-temperature crystal chemistry of acmite, diopside, hedenbergite, jadeite, spodumene, and ureyite. *American Mineralogist* **58**, 594-618 (1973).

3 Durand, G., Vilminot, S., Rabu, P., Derory, A. & Lambour, J. P. Synthesis, structure, and magnetic properties of $CaMSi_2O_6$ (M = Co, Ni) compounds and their solid solutions. *Journal of Solid State Chemistry* **124**, 374-380 (1996).

4 Raudsepp, M., Hawthorne, F. C. & Turnock, A. C. Crystal chemistry of synthetic pyroxenes on the join $CaNiSi_2O_6$-$CaMgSi_2O_6$ (diopside): A Rietveld refinement study. *American Mineralogist* **75**, 1274-1281 (1990).

5 Menzer, G. The crystal structure of garnets. *Zeitschrift Fur Kristallographie* **69**, 300-396 (1928).

6 Novak, G. A. & Gibbs, G. V. The crystal chemistry of the silicate garnets. *American Mineralogist* **56**, 791-823 (1971).

7 Peacor, D. R., Essene, E. J. & Gaines, A. M. Petrologic and crystal-chemical implications of cation order-disorder in kutnahorite $CaMn(CO_3)_2$. *American Mineralogist* **72**, 319-328 (1987).

8 Cameron, M. & Papike, J. J. Structural and chemical variations in pyroxenes. *American Mineralogist* **66**, 1-50 (1981).

9 Grew, E. S. *et al.* Nomenclature of the garnet supergroup. *American Mineralogist* **98**, 785-811 (2013).

CAPÍTULO 4

MOVILIDAD DEL Ca^{2+} EN ÓXIDOS DERIVADOS DE LA PERVOSKITA Y LA MAROKITA

Energy Storage Materials 21 (2019) 354–360

Contents lists available at ScienceDirect

Energy Storage Materials

journal homepage: www.elsevier.com/locate/ensm

DFT investigation of Ca mobility in reduced-perovskite and oxidized-marokite oxides

A. Torres [a], F.J. Luque [b,c], J. Tortajada [d], M.E. Arroyo-de Dompablo [a,*]

[a] Departamento de Química Inorgánica, Facultad de Ciencias Químicas, Universidad Complutense de Madrid, 28040, Madrid, Spain
[b] Dpto. de Mineralogía y Petrología, Facultad de Geología, Universidad Complutense de Madrid, 28040 Madrid, Spain
[c] Dpto. Geomateriales, Instituto de Geociencias IGEO (CSIC, UCM), 28040, Madrid, Spain
[d] Departamento de Química Física, Facultad de Ciencias Químicas, Universidad Complutense de Madrid, 28040, Madrid, Spain

ARTICLE INFO

Keywords:
$CaMn_4O_8$
$Ca_2Fe_2O_5$
$Ca_2Mn_2O_5$
Post-spinel
Calcium batteries

ABSTRACT

Progress in the development of rechargeable Ca-ion batteries demands the discovery of potential cathode materials. Transition metal oxides are interesting candidates due to their theoretical high energy densities, but with the drawback of a low Ca mobility. Previous computational/experimental investigations associate the electrochemical inactivity of various oxides ($CaMO_3$-perovskite, $CaMn_2O_4$-post-spinel and CaV_2O_5) to high energy barriers for Ca migration. The introduction of oxygen and/or Ca vacancies in ternary transition metal oxides is a likely way to reshape the local topology and hence improve the Ca diffusivity. In this work, the energy barriers for Ca migration are calculated and discussed for (i) oxygen-deficient perovskites within the related $Ca_2Fe_2O_5$-brownmillerite and $Ca_2Mn_2O_5$ structures, and (ii) tunnel $CaMn_4O_8$, a derivative of the $CaMn_2O_4$-marokite with Ca vacancies.

1. Introduction

High energy density electrochemical energy storage systems are urgently needed to satisfy the increasing demand for energy and power at lower costs. Rechargeable batteries based on the intercalation reaction of divalent cations (Ca^{2+}, Mg^{2+}) have been proposed as promising alternatives to Li-ion batteries [1,2]. Theoretically, rechargeable batteries based on a Ca metal anode could exhibit advantages in terms of energy density, safety and cost. In practice, however, the design of such batteries is difficulted by the lack of competitive electrode materials and electrolytes [3,4]. While recent research advances have shown that calcium can be plated and stripped in organic electrolytes [5,6], the identification of suitable cathode material is so far a pending issue [3,4,7]. Limited reversible electrochemical Ca intercalation has been reported for a handful of compounds (TiS_2 [8], MoO_3 [9], $Ca_{0.5}CoO_2$ [10], manganese hexacyanoferrate [2]), all of them showing poor cycling capability. The discovery of electrode materials can be accelerated using computational techniques. In particular, the utility of Density Functional Theory (DFT) methods to screen for potentially interesting positive electrode materials has been widely proven in the last two decades (see for instance Ref. [11] and references therein).

The relevant electrochemical characteristics of several ternary oxides as cathode materials for rechargeable Ca batteries have been foreseen using DFT calculations [12–17]. The $[Ca]_T[Mn_2]_OO_4$ spinel and the δ-$Ca_xV_2O_5$ phases appear as promising electrode materials in terms of voltage, specific capacity and ionic diffusion [12,16,17]. However, these compounds can be regarded as virtual materials since they have never been obtained experimentally. In their crystal structures the Ca-sites have unusually low coordination with oxygen ions, and hence they are metastable compared to the known polymorphs where the Ca ions present the more stable eight-fold coordination (marokite-$CaMn_2O_4$ and α-$Ca_xV_2O_5$) [14,18]. Despite the interest of these virtual oxides, for the existing oxides $CaMn_2O_4$, $CaMO_3$, α-V_2O_5 and Ca-Co-O phases, parallel experimental-computational researches establish a link between the lack of reversible electrochemical activity (experimentally observable) and a limited Ca diffusion (computational prediction) [14,15,17,19,20]. Indeed, one of the major concerns in the cathode design for the divalent battery technology is the limited mobility of Mg^{2+} and Ca^{2+} ions in inorganic structures. The migration energy barriers, which can be extracted from DFT calculations, provide an approximate indication of the ionic diffusivity [21]. It has been estimated that for a reasonable cell power rate (discharging time 2 h) the energy barriers for cation diffusion should be below 0.525 eV in micrometer particles and 0.625 eV in nanosized-particles [16,17].

* Corresponding author.
E-mail address: e.arroyo@quim.ucm.es (M.E. Arroyo-de Dompablo).

https://doi.org/10.1016/j.ensm.2019.06.002
Received 31 December 2018; Received in revised form 31 March 2019; Accepted 2 June 2019
Available online 4 June 2019

Factors controlling diffusion are based on crystal chemistry [16]. The existence of interconnected Ca sites forming migration pathways within the structure is a pre-requisite. The pathways should be wide enough for the Ca ion, and with a favorable topology to diminish the electrostatic interactions between the diffusing Ca^{2+} cation and the rest of chemical components in the structure. Therefore, compared to Li^{+} diffusion, the handicap for Ca mobility resides in the larger size of Ca^{2+} ions on one hand, and its divalent charge on the other that increases the electrostatic repulsion/attraction with the neighbouring cations/anions in the structure. Although decoupling both factors unambiguously is not plausible, signatures of either charge- or size-driven limiting mobility can be inferred for some materials. For the size-effect, previous investigations found that the larger size of Ca ions is the bottleneck for diffusion in structures that otherwise allow the diffusion of the smaller Li and Mg ions. Good examples are the post-spinel phases AMn_2O_4 (A = Li, Na, Mg, Ca) [14,22]. In other structural types, the dominant factor seems to be the coulombic repulsion between the Ca^{2+} cations and the other cations in the structure. That is the case of the perovskite structure, where a high energy barrier for Ca mobility (2 eV) arises from the face-sharing between the transition metal (TM) octahedra and the empty sites available for Ca diffusion [7,15].

The ability of transition metal ions to adopt different oxidations states and coordination environments plays in favor of a "topology based design". The local topology of many oxides changes in the related oxidized/reduced phases, and consequently introducing oxygen and/or Ca vacancies in ternary transition metal oxides may be a key factor for enhanced Ca mobility. To explore this possibility, this work presents a DFT investigation of Ca mobility in reduced-perovskite and oxidized-marokite structures. The energy barriers for Ca migration are calculated and discussed for (i) oxygen-deficient perovskites within the related brownmillerite and $Ca_2Mn_2O_5$ structures, and (ii) tunnel $CaMn_4O_8$, a derivative of the marokite $Ca_2Mn_2O_4$ with a lower Ca/Mn ratio. We will show that the incorporation of oxygen vacancies may substantially modify the electrode characteristics of the materials. In a wider context, this is in line with the enhanced electrochemical properties of oxygen-deficient perovskites (see for instance Refs. [23–28]).

2. Structures

Fig. 1a shows the ideal perovskite structure of $CaMO_3$ where M denotes the transition metal cation; it is built up from corner-sharing MO_6 octahedra and the Ca ions are twelve-fold coordinated by oxygen. Oxygen vacancies in the perovskite structure lead to the brownmillerite-type structure (Fig. 1b) with the general formula $A_2M_2O_5$. It can be described as an oxygen-deficient perovskite, where the oxygen vacancies are fully ordered, resulting in alternate layers of corner-sharing octahedra and tetrahedra parallel to (010) (Space Group *Pnma*) [29]. A transition to a cubic perovskite might occur at higher temperatures, in which vacancies become disordered [30]. The Ca ions are in irregular eight-corner polyhedra, with ten triangular and one quadrangular faces. While $Ca_2Fe_2O_5$ crystallizes in the brownmillerite structure, reduction of $CaMnO_3$ results in a different ordered oxygen deficient perovskite, $Ca_2Mn_2O_5$, in which each octahedron turns into a square-base pyramid [31,32]. Thus, the crystal structure of $Ca_2Mn_2O_5$ is built up by chains of five-coordinated Mn^{3+} cations with nearly square pyramidal coordination, forming a 3D framework (Fig. 1c) [33]. The manganese polyhedra form rings of six [MnO_5] units in the *ab* plane linked to other rings by corner sharing. The Ca atoms fit in a ten-fold polyhedron with eight triangular faces and four quadrangular faces.

The structure of post-spinel (or marokite) $CaMn_2O_4$ is built up from

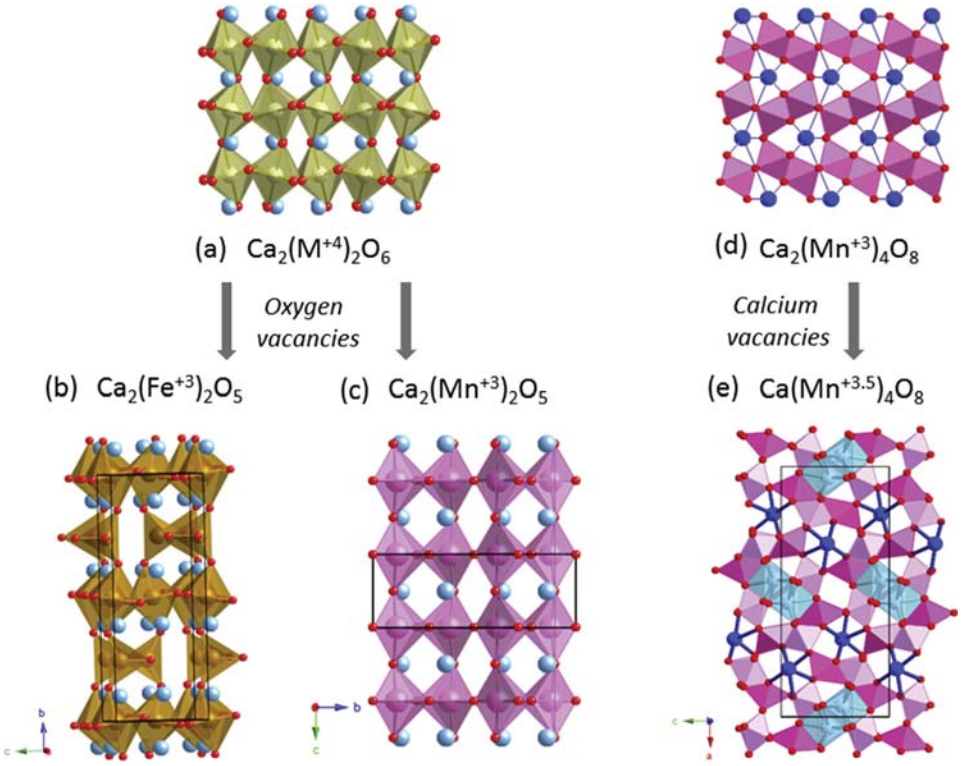

Fig. 1. Crystal structures of the investigated oxides. (a) perovskite $CaMO_3$, (b) brownmillerite $Ca_2Fe_2O_5$, (c) $Ca_2Mn_2O_5$, (d) marokite-$CaMn_2O_4$ and (e) $CaMn_4O_8$. Color code: Ca in blue, M (transition metal) in pale green, Fe in brown, Mn^{3+} in dark pink, Mn^{4+} in light pink, O in red. (For interpretation of the references to colour in this figure legend, the reader is referred to the Web version of this article.)

edge-sharing chains of MnO_6 octahedra, forming double rutile chains [34]. Each double-rutile chain is connected to two adjacent chains through edge-sharing oxygen and to another two chains through corner-sharing oxygen (see Fig. 1d). As a result, tunnels appear in the framework, where Ca ions occupy triangular prismatic sites with capped rectangular faces and Ca–O distances in the range 2.28–2.65 Å. The MnO_6 octahedron in the structure is distorted by the Jahn-Teller effect of octahedral Mn^{3+} in high spin configuration. Several authors have reported synthesis approaches to decrease the Ca concentration of marokite $CaMn_2O_4$, leading to mixed Mn^{4+}/Mn^{3+} oxides exhibiting interesting properties [35–37]. For a Ca:Mn atomic ratio equal to 1:4 ($CaMn_4O_8$) a tunnel structure is stabilized. The tunnel structure of $CaMn_4O_8$ can be at first described as a pure octahedral structure, with single and triple chains of edge-sharing MnO_6 octahedra, interconnected through the corners [38]. However, as illustrated in Fig. 1e, charge ordering produce a differentiation between half of the Mn ions in slightly distorted octahedra (Mn^{4+}, d^3 configuration) and half in a nearly five-fold coordination (Mn^{3+}, d^4 configuration). The $[Mn_4O_8]$ framework gives rise to three types of tunnels: empty rutile-like tunnels, six-sided (as those in the marokite) and eight-sided tunnels. The Ca^{2+} ions are situated in the six- and eight-sided tunnels, with half of the Ca sites being vacant. The Ca(1) ions (dark blue in Fig. 1e) inside the six-sided tunnels fit in a polyhedron similar to that in the marokite structure, with Ca(1)-O distances in the range 2.25–2.84 Å. The Ca(2) ions (light blue in Fig. 1e), located in the eight-sided tunnels, are surrounded by seven oxygen atoms forming a mono-capped triangular prismatic environment. The Ca(2)-O distances range from 2.15 to 2.55 Å.

3. Methodology

The calculations have been carried out using the ab-initio total-energy and molecular dynamics program VASP (Vienna ab-initio simulation program) developed at the Universität Wien [39]. Total energy calculations based on Density Functional Theory (DFT) were performed within the General Gradient Approximation (GGA), with the exchange and correlation functional form developed by Perdew, Burke and Ernzerhof (PBE) [40]. The interaction of core electrons with the nuclei is described by the Projector Augmented Wave (PAW) method [41]. The energy cut off for the plane wave basis set fix at a constant value of 600 eV throughout the calculations. The integration in the Brillouin zone is done on an appropriate set of *k*-points determined by the Monkhorts-Pack scheme. A convergence of the total energy close to 10 meV per formula unit is achieved with such parameters. A ferromagnetic configuration was selected in all cases. All crystal structures were fully relaxed (atomic positions, cell parameters and volume). The final energies of the optimized geometries were recalculated to correct the changes in the basis set of wave functions during relaxation. The initial atomic positions are taken from the reported structures of $Ca_2Fe_2O_5$ [29], $Ca_2Mn_2O_5$ [33] and $CaMn_4O_8$ [38]. In the latter, Ca occupied and vacant sites alternate in the tunnels.

Calcium mobility is investigated using the Nudged Elastic Band method (NEB) as implemented in VASP. To study diffusion, a vacancy is created in the structural model of the stoichiometric oxides and a simply jumping mechanism from an occupied position to the vacant site is considered. We used superstructures of the unit cells that guarantee a minimum interaction between defects: $Ca_{31}Fe_{32}O_{80}$ ($2 \times 1 \times 2$ of the unit cell), $Ca_{23}Mn_{24}O_{60}$ ($2 \times 1 \times 3$ of the unit cell) and $Ca_{15}Mn_{64}O_{128}$ ($1 \times 2 \times 1$ of the unit cell). Constant volume calculations were performed within the GGA approximation for three or five intermediate images initialized by linear interpolation between the two fully relaxed end-points. To converge the minimum energy path in the NEB procedure, the convergence threshold of the total energy of each image was set to 1×10^{-4} eV, with a residual force threshold of 0.01 eV/Å. To calculate the energy at the saddle point, cubic splines were fit through the relaxed images along each hop.

Average voltage for Ca deinsertion from $Ca_2Fe_2O_5$ (Fe^{3+}/Fe^{4+} redox couple) was calculated within the GGA + U method, following the methodology described by Aydinol et al. [42]. For consistency with the literature on this topic [12,15,16,43], the effective U value for the Fe-*d* orbitals where set to 5 eV (J = 1eV).

4. Results

$Ca_2Fe_2O_5$. In the brownmillerite structure, the interconnected Ca sites form a channel along the *b*-axis (see Fig. 1b). The calculated energy barrier along this channel is 2.3 eV (Fig. 2a), similar to the predicted for the perovskite structure (around 2 eV) [15]. This is not surprising, since diffusion along this pathway involves Ca jumps between sites with the same topology than in the perovskite structure. Diffusion in the *ac* plane, consisting of tetrahedral $[FeO_4]$ units, is possible along the pathway shown in Fig. 2b: the oxygen vacancies respective to the perovskite structure create a zigzag path for potential Ca motion. As shown in Fig. 2b and c the initial and final Ca sites share triangular faces, being connected through an interstitial site that does not share any face with the FeO polyhedra. This contrasts with the perovskite structure, where the interstitial site shares faces with the FeO octahedra. The direct interpolation of three images between the relaxed end-points favors the path out from the Ca-Ca shared triangular face, slightly above the O-O dumbbell bond (see Fig. 2c). At the saddle point, the Ca^{2+} adopts a three-fold coordination with Ca-O distances 2.22–2.31 Å to the O-O dumbbell and the apical oxygen. The Ca-Fe distances are 2.84 Å and 3.01 Å to the two adjacent Fe ions in tetrahedral coordination, and 3.10 Å to the two Fe ions in octahedral coordination in the plane below. Note that migration across the interstitial site avoiding the O-O dumbbell would result in too short Ca-tetrahedral Fe distances. The calculated energy barrier along this path is 1 eV; the transition state in the browmillerite seems stabilized respecting the perovskite.

$Ca_2Mn_2O_5$. Fig. 3 shows the analysis of the Ca diffusion pathways in the $Ca_2Mn_2O_5$ structure. Along the *c*-axis, the neighbouring Ca ions share a triangular face forming a tunnel of interconnected Ca ions (Fig. 3a). The small size of the triangular face precludes Ca diffusion (Ca-O distances at the saddle point are 2.12, 2.18 and 2.22 Å). Consequently, the calculated energy barrier is 2.6 eV (Fig. 3b, pathway 1). In the *ab* plane, there are two different pathways (Fig. 3c). Along the pathway labelled as 2, the adjacent Ca sites share an edge, with the intermediate eight-fold coordination site sharing faces with the Mn-O polyhedra. If the Ca ion hops from the equilibrium position to this site, a large Coulombic repulsion is generated, because of the short distance between Ca^{2+} and Mn^{3+} ions. Therefore, the Ca ion is pushed to jump across the common edge between the two neighbouring CaO polyhedra (Ca–O distance 2.22 Å). The calculated energy migration barrier is 2.2 eV. The pathway denoted as 3 in Fig. 3c and d implicates inter-connected Ca sites sharing a quadrangular face. In the diffusion along this channel, the Ca ion passes across the square face with Ca-O distances of 1.95–2.26 Å. At the saddle point the Ca ion is in the middle of a square face sharing edges with the four Mn-O polyhedra (see Fig. 3d), with Ca-Mn distances 2.79 Å x 2 and 2.88 Å x 2. The calculated energy barrier is 1.8 eV.

$CaMn_4O_8$. Fig. 1 shows the two types of Ca ions in this structure: Ca(1) in the six-sized tunnels and Ca(2) in eight-sized tunnel. The calculated energy differences to create a vacancy in the Ca(1) *vs* the Ca(2) sites (0.77 eV for $Ca_7Mn_{32}O_{64}$ and for 0.52 eV for $Ca_{15}Mn_{64}O_{128}$) suggest that Ca ions will preferably deintercalate from the Ca(2) sites in the eight-sized tunnels. In these tunnels, there are two possible diffusion pathways labelled as 1 and 2 in Fig. 4a. The topology of pathway 1 is similar to that in the marokite structure: a tunnel formed by triangular-face sharing interconnected Ca sites. In $CaMn_4O_8$ the distance between Ca ions is 5.78 Å, as there is a vacant Ca site in between. The Ca ion passes across a triangular face of the polyhedra to the intermediate vacant site that represents a local minimum in the energy landscape (Fig. 4b). The Ca-O distance in the triangular window are too short (Ca-O distances are 2.09, 2.20 and 2.25 Å), as also found in the marokite structure [14], and accordingly, the calculated energy barrier is similarly high (2.2 eV). In

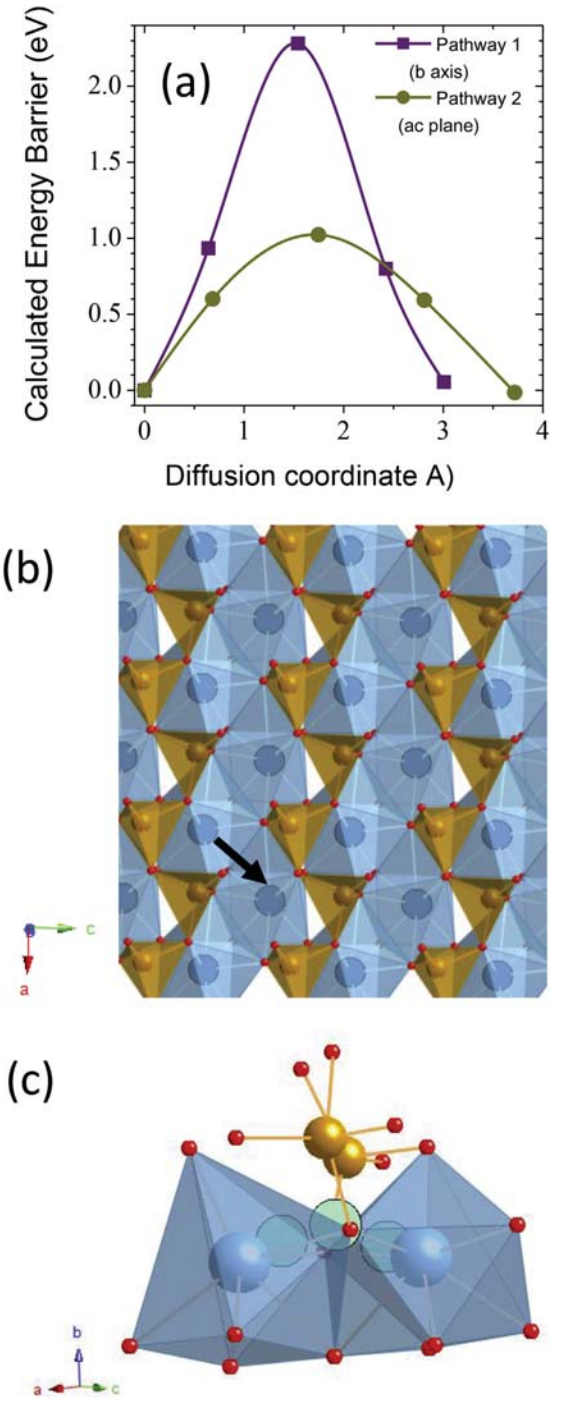

Fig. 2. (a) Calculated energy barrier for Ca diffusion in $Ca_2Fe_2O_5$. (b) Pathway along the *ac* plane. The arrow indicates the hopping mechanism from the occupied to the empty Ca sites. (c) Detail of the intermediate site along the diffusion pathway. Color code: Ca light blue, diffusing Ca in cyan, Fe brown, O red. (For interpretation of the references to colour in this figure legend, the reader is referred to the Web version of this article.)

pathway 2, the direct interpolation of three images between the relaxed end-points favors the path across the shared-edge of the two neighbouring Ca sites separated by 3.14 Å. In the transition state, the Ca^{2+} fits in the edge midway the O-O dumbbell (Ca–O distance 2.05 Å), but with sufficiently large Ca–Mn distances of 3.31, 3.34 (x2) and 3.38 Å. Therefore, the high calculated energy barrier of 1.7 eV seems to be more related to size than to charge effects. This energy landscape is slightly asymmetric, with the energy of the start and end points differing in 0.17 eV. The orbital and Mn^{3+}/Mn^{4+} charge ordering in $CaMn_4O_8$ [38] is disrupted due to the vacancy incorporation and such a complex electronic structure is difficult to capture with DFT approximations.

5. Discussion

The results for $CaMn_4O_8$ (path 1) indicate that the large size of Ca ions is an obstacle for Ca diffusion in marokite-related structures. Interestingly, tunnels of Ca ions sharing triangular faces exist in other structural types. Table 1 lists the calculated energy barriers for selected examples. In all cases, the migration barriers exceed 1.5 eV, independently on the Ca occupation of the tunnel; for a given tunnel, the incorporation of Ca vacancies does not lower the energy barriers (compare CaV_2O_5/α-V_2O_5 and $CaMn_2O_4/CaMn_4O_8$). These results suggest that triangular-face tunnels are unfavorable for Ca^{2+} diffusion. This contrasts with the predicted diffusivity of Li^+, Na^+ and Mg^{2+} in those tunnels (see Table 1). Importantly, the calculated energy barriers of Table 1 follow the order $Li^+ < Mg^{2+} < Na^+ < Ca^{2+}$, in consonance with both the ionic radii ($r_{(VI)} = 0.76$ Å (Li^+), 0.72 Å (Mg^{2+}), 1.02 Å (Na^+), and 1.0 Å (Ca^{2+}) [44]) and the ionic charge. Since Ca^{2+} and Na^+ ions have comparable ionic radii, the larger barrier of the former calls for a size-charge join effect. In addition to the marokite structure (or CM) Table 1 lists the calculated energies for a second $CaMn_2O_4$ polymorph (denoted as CF). The CF and CM forms are known as post-spinel phases; they show very similar structures based on double-rutile chains, interconnected by vertex and edge sharing oxygen in CM but only through vertex sharing oxygen in CF. Noteworthy, the calculated energy barriers for the CF polymorph are substantially lower than those for the CM-polymorph (marokite). This reinforce the role of the electrostatic interactions in the energy barriers.

Standing on size arguments, structures with Ca-diffusion pathways consisting of triangular faces of low-coordination polyhedra, or quadrangular windows of large-coordination polyhedra, seem more adequate for Ca mobility. In the lowest energy pathway of the $Ca_2Mn_2O_5$ structure (pathway 2 in Fig. 4), the adjacent Ca sites share a quadrangular face of the ten-fold polyhedra. The larger size of this face favors Ca mobility. Nevertheless, at the transition state the channel shares the four edges with the surrounding Mn polyhedra, with the electrostatic repulsions raising the energy of the intermediate site to 1.8 eV. This points out to the energy landscape for Ca motion being rather charge-than size-limited, similarly to the case of the perovskite structure.

In the brownmillerite structure of $Ca_2Fe_2O_5$, the oxygen vacancies create a new pathway, with the diffusing Ca ion hopping slightly above the O-O dumbbell of the edge-shared between adjacent Ca sites. Hence, there is a size-penalty, with the energy of the first image from the pathway being quite high (0.6 eV). In turn, at the transition state, the Ca ion has no face-sharing with the Fe polyhedra, being the closer Fe ions at distances of around 3 Å. The weaker electrostatic repulsions in brownmillerite, compared to the perovskite structure or the $CaMn_2O_5$ structures, lowers the calculate energy barrier down to 1 eV. The substantial dropping from 2 eV in the perovskite to 1 eV in the browmillerite is not enough to propose the latter as electrode material. For completeness, we have calculated the average voltage for Ca deinsertion according with the reaction:

$$Ca_2Fe_2O_5 \rightarrow CaFe_2O_5 + Ca \quad (1)$$

Ca deinsertion involves the Fe^{3+}/Fe^{4+} couple, with a theoretical specific capacity of 198 mAh/g. The predicted voltage (4.16 V) is beyond

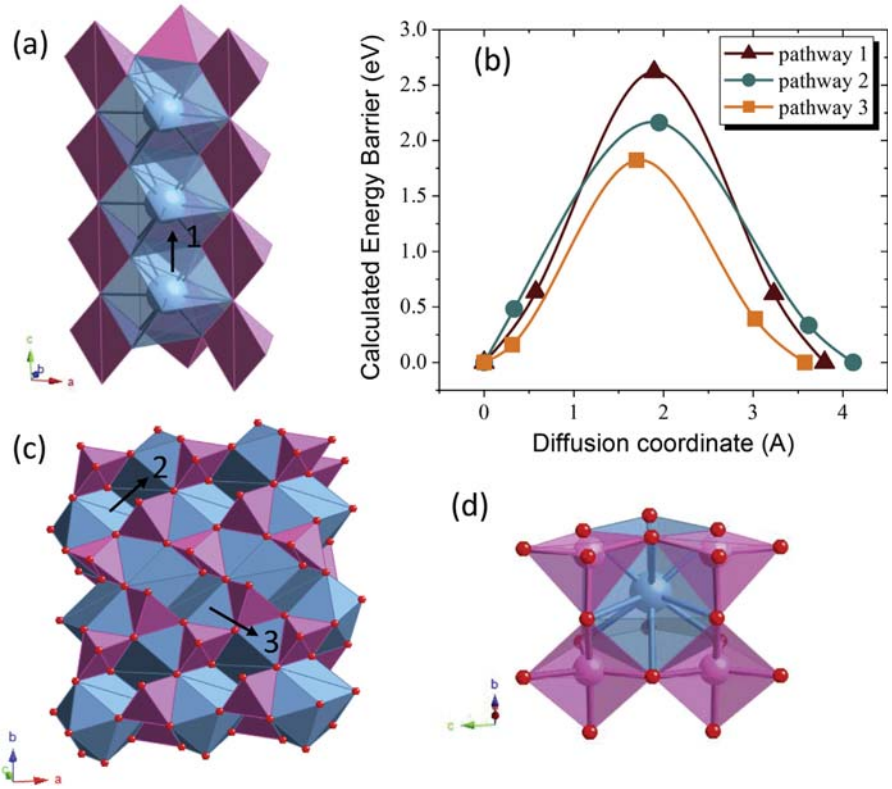

Fig. 3. Analysis of Ca mobility in $Ca_2Mn_2O_5$. (a) View of the pathway along the *c* axis. (b) Calculated energy barriers for paths 1–3. (c) The two possible pathways in the *ab* plane. (d) View of the most favorable pathway 3, showing the quadrangular window at the transition state. Color code: Ca in blue, Mn in pink, O in red. (For interpretation of the references to colour in this figure legend, the reader is referred to the Web version of this article.)

the stability window of the current electrolytes [5,7], making inviable the experimental investigation of $Ca_2Fe_2O_4$ as cathode material at the current state of the Ca batteries technology.

Enhancing the Ca mobility in oxides is a tricky crystal design challenge. Anion-deficient oxides occur commonly and, in cases where the anions are ordered, a variety of complex structures with reduced TM coordination number are generated. As a rule of thumb, creating a sufficient amount of ordered oxygen vacancies assists to reduce the face-sharing polyhedra between the Ca and TM sublattices. Even though this route allows weakening the Coulombic interactions, the aforementioned size issue constrains the candidate structures to those with Ca ions in polyhedra entailing large faces. Actually, a low Ca energy barrier (0.5 eV) has been reported for the virtual and metaestable spinel $Ca_T[Mn_2]_OO_4$ [12], in which Ca ions occupies tetrahedral sites that have larger triangular faces than higher-coordination number polyhedra. The alternatives are stable structures based on Ca-highly coordinated oxygen polyhedra, but possessing quadrangular faces. Structures of reduced perovskites, such as $Sr_4Fe_4O_{11}$ might fulfill these requirements [45]. Ca-exchanged layered-perovskites belonging to the Ruddlesden-Popper and the Dion-Jacobson series are other interesting oxides to explore [46].

Note that in this work the barriers for Ca migration were assessed in the low-vacancy regime, since the investigated materials are synthesizable in their discharged state. The concentration of Ca in the host material varies along the charge of the cell, thereby affecting the migration barriers. Table 1 listed some example of materials with a subtle implication of Ca concentration in the energy barriers, as the main bottleneck in these structures is the narrow size of the tunnel for Ca diffusion. It should however be highlighted that this is not a general rule. Ca deinterclataion might enhance the electrostatic repulsions (more oxidized TM cations), raising the energy barriers for Ca migration. This effect is more significant for the multivalent ions. For instance, the calculated energy barrier for Mg migration in olivine-Mg_xMnSiO_4 spans in a 0.7 eV range (0.8 eV at x = 1, 1.5 eV at x = 0.5 and 1.3 eV at x = 0) [43], whereas the variation in olivine-Li_xMnPO_4 is only 0.08 eV (0.25 eV at x = 1 and 0.33 eV at x = 0) [21]. In this regard, additional DFT investigation and parallel experimental research in electrochemically active Ca cathodes (such as TiS_2 [8], MoO_3 [9] or $Ca_3Co_2O_6$ [20]) are necessary to advance in the field.

6. Conclusions

Transition metal oxides are a major class of compounds displaying a variety of crystal structures. By tuning the oxidation state of the transition metal, related structural types based on different TM polyhedra, or polyhedra arrangements, are accessible. The DFT results evidence that for some of these oxidized/reduced oxides the Ca mobility is equally hampered than in the parent oxides (i.e. $CaMn_4O_8$ or $Ca_2Mn_2O_5$), due to the occurrence of Ca sites with small triangular faces. A second key factor is to forestall the face sharing between the TM polyhedra and the Ca-intermediate site. DFT results reveal that this can be accomplished in some reduced oxides (i.e. $Ca_2Fe_2O_5$ *versus* $CaFeO_3$). Computational research is ongoing to pinpoint structures satisfying the topological criteria for Ca mobility. Oxygen-deficient oxides of the abundant and affordable Mn and Fe ions are worthy of attention.

It should be underlined that, despite the effectiveness of using DFT methods as a constructive instrument in the quest for Ca ion conducting materials, experimental advances concerning electrolytes and testing protocols are critical to confirm the suitability of DFT-proposed materials

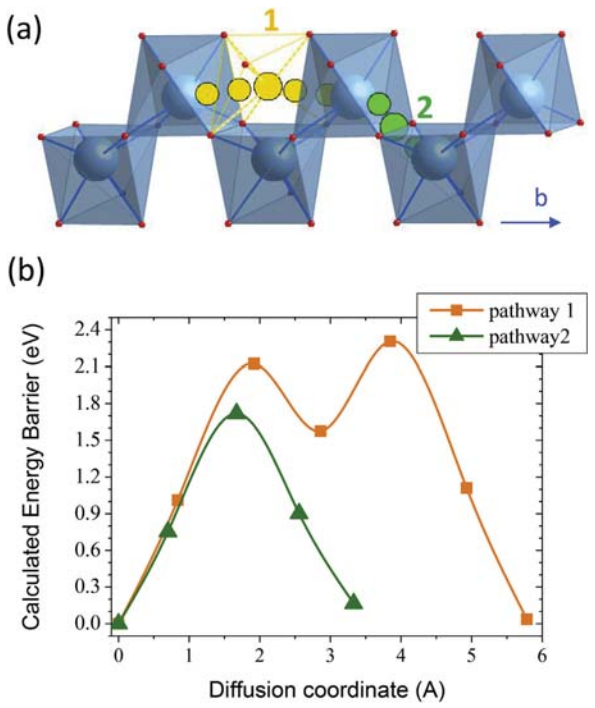

Fig. 4. (a) View of the Ca diffusion pathways in the eight-sided channels of $CaMn_4O_8$. (b) Calculated energy barriers for Ca diffusion in $CaMn_4O_8$.

Table 1
Calculated energy barriers for Ca diffusion in tunnels formed by triangular face sharing sites. For comparison, the calculated energy barriers for other intercalant are listed when available.

Compound	n-fold of the Ca polyhedra	Ca occupancy	Calculated Ca energy barrier (eV)	Calculated energy barriers for other intercalants (eV)
Marokite-$CaMn_2O_4$ (CM structure)	8	1	1.8 [14]	Li: 0.3 [22] Na: 1 [22] Mg: 0.75 [22]
$CaMn_4O_8$ (eight sided-tunnel)	7	1/2	1.7 [this work]	
$CaMn_2O_4$ (CF structure)	8	1	1.3 [14]	Li: 0.1 [22] Na: 0.38 [22] Mg: 0.4 [22]
CaV_2O_5	8	1	1.6 [this work] 1.9 [17]	
α-V_2O_5	8	0	1.7 [17] 1.8 [47]	Li: 0.31 [47], 0.3 [17] Na: 1.16 [47] Mg: 0.97 [47], 0.9 [17]
$Ca_2Mn_5O_5$	10	1	2.6 [this work]	

(for instance $Ca_2Fe_2O_5$ in this work) as cathodes in Ca-based batteries.

Acknowledgments

Funding from the European Union's Horizon 2020 research and innovation programme H2020 FETOPEN-1-2016-2017 (CARBAT, grant agreement no. 766617) is acknowledged. The authors are grateful for access to the computational facilities from Universidad de Oviedo (MALTA-Consolider cluster) and the Spanish.

References

[1] J. Muldoon, C.B. Bucur, T. Gregory, Quest for nonaqueous multivalent secondary batteries: magnesium and beyond, Chem. Rev. 114 (2014) 11683–11720.
[2] A.L. Lipson, B. Pan, S.H. Lapidus, C. Liao, J.Y. Vaughey, B.J. Ingram, Rechargable Ca-ion batteries: a new energy storage system, Chem. Mater. 27 (2015) 8442–8447.
[3] R.J. Gummow, G. Vamvounis, M.B. Kannan, Y. He, Calcium-ion batteries: current state-of-the-art and future perspectives, Adv. Mater. 30 (2018), e1801702.
[4] A. Ponrouch, M.R. Palacin, On the road toward calcium-based batteries, Curr. Opin. Electrochem. 9 (2018) 1–7.
[5] A. Ponrouch, C. Frontera, F. Barde, M.R. Palacin, Towards a calcium-based rechargeable battery, Nat. Mater. 15 (2015) 169–172.
[6] D. Wang, X. Gao, Y. Chen, L. Jin, C. Kuss, P.G. Bruce, Plating and stripping calcium in an organic electrolyte, Nat. Mater. 17 (2018) 16–20.
[7] P. Canepa, G.S. Gautam, D.C. Hannah, R. Malik, M. Liu, K.G. Gallagher, K.A. Persson, G. Ceder, Odyssey of multivalent cathode materials: open questions and future challenges, Chem. Rev. 117 (2017) 4287–4341.
[8] D.S. Tchitchekova, A. Ponrouch, R. Verrelli, T. Broux, C. Frontera, A. Sorrentino, F. Barde, N. Biskup, M.E. Arroyo-de Dompablo, M.R. Palacin, Electrochemical intercalation of calcium and magnesium in TiS_2: fundamental studies related to multivalent battery applications, Chem. Mater. 30 (2018) 847–856.
[9] M. Cabello, F. Nacimiento, R. Alcantara, P. Lavela, C. Pérez-Vicente, J.L. Tirado, Applicability of molybdite as an electrode material in calcium batteries: a structural study of layer-type Ca_xMoO_3, Chem. Mater. 30 (2018) 5853–5861.
[10] M. Cabello, F. Nacimiento, J.R. González, G. Ortiz, R. Alcántara, P. Lavela, C. Pérez-Vicente, J.L. Tirado, Advancing towards a veritable calcium-ion battery: $CaCo_2O_4$ positive electrode material, Electrochim. Commun. 67 (2016) 59–64.
[11] Y.S. Meng, M.E. Arroyo-de Dompablo, Recent advances in first principles computational research of cathode materials for lithium-ion batteries, Accounts Chem. Res. 46 (2013) 1171–1180.
[12] M. Liu, Z. Rong, R. Malik, P. Canepa, A. Jain, G. Ceder, K.A. Persson, Spinel compounds as multivalent battery cathodes: a systematic evaluation based on *ab initio* calculations, Energy Environ. Sci. 8 (2015) 964–974.
[13] M. Liu, A. Jain, Z. Rong, X. Qu, P. Canepa, R. Malik, G. Ceder, K.A. Persson, Evaluation of sulfur spinel compounds for multivalent battery cathode applications, Energy Environ. Sci. 9 (2016) 3201–3209.
[14] M.E. Arroyo-de Dompablo, C. Krich, J. Nava-Avendano, N. Biskup, M. Rosa Palacin, F. Barde, A joint computational and experimental evaluation of $CaMn_2O_4$ polymorphs as cathode materials for Ca ion batteries, Chem. Mater. 28 (2016) 6886–6893.
[15] M.E. Arroyo-de Dompablo, C. Krich, J. Nava-Avendaño, M.R. Palacín, F. Bardé, In quest of cathode materials for ca ion batteries: the $CaMO_3$ perovskites (M = Mo, Cr, Mn, Fe, Co, Ni), Phys. Chem. Chem. Phys. 18 (2016) 19966–19972.
[16] Z. Rong, R. Malik, P. Canepa, G.S. Gautam, M. Liu, A. Jain, K. Persson, G. Ceder, Materials design rules for multivalent ion mobility in intercalation structures, Chem. Mater. 27 (2015) 6016–6021.
[17] G.S. Gautam, P. Canepa, R. Malik, M. Liu, K. Perssonb, G. Ceder, First-principles evaluation of multi-valent cation insertion into orthorhombic V_2O_5, Chem. Commun. 51 (2015) 13619–13622.
[18] P. Millet, C. Satto, P. Sciau, J. Galy, MgV_2O_5 and $\delta Li_xV_2O_5$: a comparative structural investigation, J. Solid State Chem. 136 (1998) 56–62.
[19] R. Verrelli, A.P. Black, C. Pattanathummasid, D.S. Tchitchekova, A. Ponrouch, J. Oro-Sole, C. Frontera, F. Barde, P. Rozier, M.R. Palacin, On the strange case of divalent ions intercalation in V_2O_5, J. Power Sources 407 (2018) 162–172.
[20] D.S. Tchitchekova, C. Frontera, A. Ponrouch, C. Krich, F. Barde, M.R. Palacin, Electrochemical calcium extraction from 1D-$Ca_3Co_2O_6$, Dalton Trans. 47 (2018) 11298–11302.
[21] D. Morgan, A. Van der Ven, G. Ceder, Li conductivity in Li_xMPO_4 (M = Mn, Fe, Co, Ni) olivine materials, Electrochem. Solid State Lett. 7 (2004) A30–A32.
[22] C. Ling, F. Mizuno, Phase stability of post-spinel compound AMn_2O_4 (A = Li, Na, or Mg) and its application as a rechargeable battery cathode, Chem. Mater. 25 (2013) 3062–3071.
[23] J. Kim, X. Yin, K.C. Tsao, S. Fang, H. Yang, $Ca_2Mn_2O_5$ as oxygen-deficient perovskite electrocatalyst for oxygen evolution reaction, J. Am. Chem. Soc. 136 (2014) 14646–14649.
[24] J.R. Petrie, H. Jeen, S.C. Barron, T.L. Meyer, H.N. Lee, Enhancing perovskite electrocatalysis through strain tuning of the oxygen deficiency, J. Am. Chem. Soc. 138 (2016) 7252–7255.
[25] Y. Zhu, W. Zhou, J. Yu, Y. Chen, M. Liu, Z. Shao, Enhancing electrocatalytic activity of perovskite oxides by tuning cation deficiency for oxygen reduction and evolution reactions, Chem. Mater. 28 (2016) 1691–1697.
[26] N. Tyminska, G. Wu, M. Dupuis, Water oxidation on oxygen-deficient barium titanate: a first-principles study, J. Phys. Chem. C 121 (2017) 8378–8389.
[27] C.A.J. Fisher, M.S. Islam, Defect, protons and conductivity in brownmillerite-structured $Ba_2In_2O_5$, Solid State Ionics 118 (1999) 355–363.
[28] N. Sharma, K.M. Shaju, G.V. Subba Rao, B.V.R. Chowdari, Mixed oxides $Ca_2Fe_2O_5$ and $Ca_2Co_2O_5$ as anode materials for Li-ion batteries, Electrochim. Acta 49 (2014) 1035–1043.
[29] J. Berggren, Refinement of crystal structure of dicalcium ferrite, $Ca_2Fe_2O_5$, Acta Chem. Scand. 25 (1971) 3616–3624.
[30] P. Berastegui, S.G. Eriksson, S. Hull, A neutron diffraction study of the temperature dependence of $Ca_2Fe_2O_5$, Mater. Res. Bull. 34 (1999) 303–314.

[31] K.R. Poeppelmeier, M.E. Leonowicz, J.M. Longo, $CaMnO_{2.5}$ and $Ca_2MnO_{3.5}$: new oxygen-defect perovskite-type oxides, J. Solid State Chem. 44 (1982) 89–98.
[32] M.T. Anderson, J.T. Vaughey, K.R. Poeppelmeier, Structural similarities among oxygen-deficient perovskites, Chem. Mater. 5 (1993) 151–165.
[33] K.R. Poeppelmeier, M.E. Leonowicz, J.C. Scanlon, J.M. Longo, W.B. Yelon, Structure determination of $CaMnO_3$ and $CaMnO_{2.5}$ by x-ray and neutron methods, J. Solild State Chem. 45 (1982) 71–79.
[34] C.D. Ling, J.J. Neumeier, D.N. Argyriou, Observation of antiferromagnetism in marokite $CaMn_2O_4$, J. Solild State Chem. 160 (2001) 167–173.
[35] J. Hadermann, A.M. Abakumov, L.J. Gillie, C. Martin, M. Hervieu, Coupled cation and charge ordering in the $CaMn_3O_6$ tunnel structure, Chem. Mater. 18 (2006) 5530–5536.
[36] M.M. Najafpour, D.J. Sedigh, Water oxidation by manganese oxides, a new step towards a complete picture: simplicity is the ultimate sophistication, Dalton Trans. 42 (2013) 12173–12178.
[37] W.S. Glaunsinger, H.S. Horowitz, J.M. Longo, A. Chang, Magnetic-properties of the mixed-valence compounds $CaMn_3O_6$ and $CaMn_4O_8$, J. Solid State Chem. 35 (1980) 187–191.
[38] N. Barrier, C. Michel, A. Maignan, M. Hervieu, B. Raveau, $CaMn_4O_8$, a mixed valence manganite with an original tunnel structure, J. Mater. Chem. 15 (2005) 386–393.
[39] G. Kresse, J. Furthmuller, Efficient iterative schemes for *ab initio* total-energy calculations using a plane-wave basis set, Phys. Rev. B 54 (1996) 11169.
[40] J.P. Perdew, K. Burke, M. Ernzerhof, Generalized gradient approximation made simple, Phys. Rev. Lett. 77 (1996) 3865–3868.
[41] P.E. Bloch, Projector augmented-wave method, Phys. Rev. B 50 (1994) 17953.
[42] M.K. Aydinol, A.F. Kohan, G. Ceder, K. Cho, J. Joannopoulos, *Ab initio* study of lithium intercalation in metal oxides and metal dichalcogenides, Phys. Rev. B 56 (1997) 1354–1365.
[43] A. Torres, M.E. Arroyo-de Dompablo, Comparative investigation of $MgMnSiO_4$ and olivine-type $MgMnSiS_4$ as cathode materials for Mg batteries, J. Phys. Chem. C 122 (2018) 9356–9362.
[44] R.D. Shannon, C.T. Prewitt, Revised effective ionic radii in halides and chalcogenides, Acta Crystallogr. 32 (1976) 751–767.
[45] J.P. Hodges, S. Short, J.D. Jorgensen, X. Xiong, B. Dabrowski, S.M. Mini, C.W. Kimball, Evolution of oxygen-vacancy ordered crystal structures in the perovskite series $Sr_nFe_nO_{3n-1}$ (n=2, 4, 8, and infinity), and the relationship to electronic and magnetic properties, J. Solid State Chem. 151 (2000) 190–209.
[46] R.E. Schaak, T.E. Mallouk, Perovskites by design: a toolbox of solid-state reactions, Chem. Mater. 14 (2002) 1455–1471.
[47] J. Carrasco, Role of Van der Waals forces in thermodynamics and kinetics of layered transition metal oxide electrodes: alkali and alkaline-earth ion insertion into V_2O_5, J. Phys. Chem. C 118 (2014) 19599–19607.

CAPÍTULO 5

EVALUACIÓN DE LAS PRESTACIONES DE ALGUNOS ÓXIDOS DE COBALTO

Solid State Ionics 340 (2019) 115004

Contents lists available at ScienceDirect

Solid State Ionics

journal homepage: www.elsevier.com/locate/ssi

Evaluation of cobalt oxides for calcium battery cathode applications

A. Torres[a], F. Bardé[b], M.E. Arroyo-de Dompablo[a,*]

[a] Departamento de Química Inorgánica, Facultad de Ciencias Químicas, Universidad Complutense de Madrid, 28040 Madrid, Spain
[b] Toyota Motor Europe, Research & Development, Advanced Material Research, Battery & FC, Technical Centre, Hoge Wei 33 B, B-1930 Zaventem, Belgium

ARTICLE INFO

JEL classification:
A60
A70
A80

Keywords:
Calcium battery
Intercalation
$Ca_2Co_2O_5$
$Ca_3Co_4O_9$
$Ca_3Co_2O_6$

ABSTRACT

The identification of potential cathode materials is a requirement for the development of a rechargeable calcium based battery technology. In this work, we use Density Functional Theory (DFT) calculations to explore the electrode characteristics of three ternary calcium cobalt oxides with distinct Co−O dimensionality: 3D-$Ca_2Co_2O_5$ (brownmillerite type structure), 2D-$Ca_3Co_4O_9$ (a misfit compound) and 1D-$Ca_3Co_2O_6$ (K_4CdCl_6 structural type). For the three compounds calculations predict Co^{3+}/Co^{4+} voltages in the 3–4 V range, with a volume variation below 8% upon Ca deinsertion. Further Co^{4+} oxidation is predicted at too high voltages not reachable in practice. The maximum specific capacities are therefore 192 mAh/g ($Ca_2Co_2O_5$), 165 mAh/g ($Ca_3Co_4O_9$) and 160 mAh/g ($Ca_3Co_2O_6$). The potential application of $Ca_2Co_2O_5$ is discarded based on a large energy barrier for Ca diffusion (1.3 eV). With energy barriers for Ca diffusion of 0.9 eV, the 2D and 1D oxides are appealing as low rate cathode materials. To complete a previous experimental investigation, we have analyzed the reversibility of the Ca deinterclation reaction of 1D-$Ca_3Co_2O_6$. It is found that a phase transformation takes place upon decalciation driven by the change in the electronic configuration of Co ions (from High Spin-trigonal prismatic Co^{3+} to octahedral Low Spin-Co^{4+}) and involving the Ca diffusion pathways.

1. Introduction

Lithium-ion batteries (LIB) are a key component for portable electronic devices, more importantly, they may offer a possible near-term solution for environment-friendly transportation and energy storage for renewable energies source such as solar and wind. Although LIB offer higher energy density and a longer cycle life than other battery technologies, to meet the increasing energy and power demand at lower cost, advances in electrochemical energy storage systems are urgently needed. An attractive longer term alternative is to combine sustainability with prospects of high energy density and develop metal anode technologies based on multivalent abundant elements such as Ca or Mg [1]. Calcium is an attractive candidate due to its low cost, natural abundance and low reduction potential [2–4]. At this very early stage of the Ca-based technology, critical technical advancements are necessary towards overcoming the existing hurdles [5]. Among them, developing cathode materials enabling effective diffusion of Ca^{2+} ions is far from being evident [6]. Several compounds (oxides, sulphides and phosphates) have been investigated as cathode intercalation materials for Ca batteries. Recent reviews summarize the main results [2,4,5]. A specific capacity around 200 mAh/g at 2 V is attainable for the classical intercalation material TiS_2 [7], with other chalcogenides offering interesting prospects in terms of Ca diffusion although with a penalty in voltage [8,9]. The more sluggish kinetics of Ca^{2+} diffusion in oxides is a handicap to develop high energy density cathode materials [4,10–12]. The local topology is a critical factor for Ca^{2+} mobility [6,10,12], and fundamental research is needed to identify propitious crystal chemistries.

The high redox potential of the Co^{4+}/Co^{3+} couple makes cobalt oxides an interesting class of materials to investigate. In addition, calcium cobalt oxides crystallize in a variety of structural types, allowing to map fundamental cathode properties-structure relationship. Preliminary work suggests reversible electrochemical activity for layered-$CaCo_2O_4$ (a form without stability field in the P-T Ca-Co-O phase diagram) in electrochemical cells bearing V_2O_5 as the anode [13]. Irreversible calcium extraction has been proven for $Ca_3Co_2O_6$ at 3.5 V vs the Ca electrode [14]. In addition good electrochemical properties are predicted for the virtual spinel $CaCo_2O_4$ [15]. These promising results encourage the investigation of other calcium cobalt oxides. Two ternary oxides appear in the CaO-CoO phase diagram: $Ca_3Co_2O_6$ and $Ca_9Co_{12}O_{28}$ (normally expressed as $Ca_3Co_4O_9$) [16–18]. Another ternary oxide with the brownmillerite structure ($Ca_2Co_2O_5$) has been reported [19,20]. From the crystal dimensionality point of view, the Co−O arrangements in these oxides provide a 3D (brownmillerite), 2D

* Corresponding author.
E-mail address: e.arroyo@quim.ucm.es (M.E. Arroyo-de Dompablo).

https://doi.org/10.1016/j.ssi.2019.115004
Received 19 January 2019; Received in revised form 6 June 2019; Accepted 13 June 2019
Available online 11 July 2019

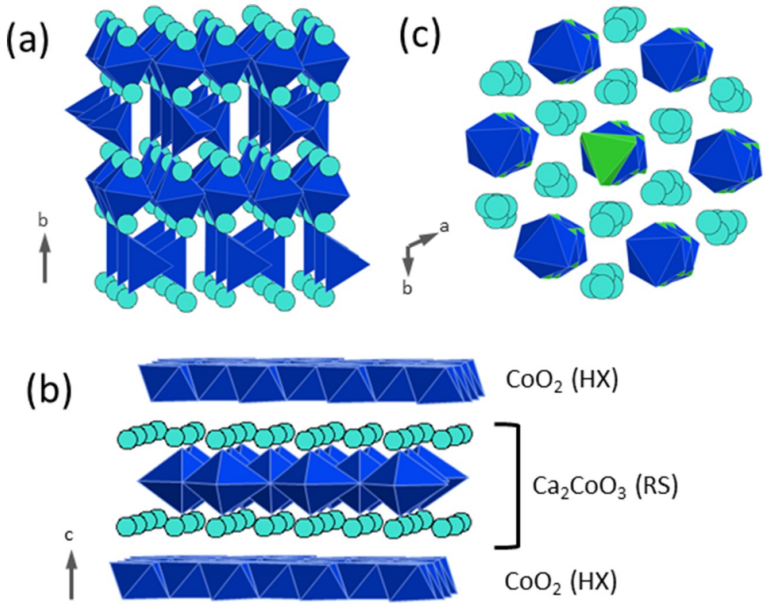

Fig. 1. Crystal structure of (a) 3D-$Ca_2Co_2O_5$ (b) 2D-$Ca_3Co_4O_9$ and (c) 1D-$Ca_3Co_2O_6$. Note the 3D, 2D and 1D character of the Co−O skeleton in these structures. Color code: Ca light blue, octahedral Co dark blue, trigonal prismatic Co green. RS and HX denote the Rock-Salt and Hexagonal subsystems, respectively. (For interpretation of the references to color in this figure legend, the reader is referred to the web version of this article.)

($Ca_3Co_4O_9$) and 1D ($Ca_3Co_2O_6$) skeleton for Ca diffusion (see Fig. 1).

In the present work, we utilize first principles calculations at the Density Functional Theory (DFT) level to sketch the voltage-composition profile of $Ca_3Co_2O_6$, $Ca_3Co_4O_9$ and $Ca_2Co_2O_5$ and evaluate their maximum specific capacities. Ca diffusion in the 1D, 2D and 3D-cobalt oxides is estimated thorough the computation of the energy migration barriers. The DFT-extracted energy barriers are rationalized focussing in the crystal dimensionality and the topology around the diffusing Ca ions. Finally, the reversibility of the deintercalation reaction from the most promising oxide $Ca_3Co_2O_6$ is investigated in depth.

1.1. Structures

The brownmillerite structure (Fig. 1a), of general formula $A_2B_2O_5$, can be described as an oxygen-deficient perovskite, where the oxygen vacancies are fully ordered, resulting in layers alternating between corner-sharing octahedra and tetrahedral along the *b* axis of the structure (Space Group *Pnma*). A transition to a cubic perovskite might occur at higher temperatures, in which vacancies become disordered. While the interesting magnetic and electronic properties of calcium ferrite $Ca_2Fe_2O_5$ have motivated a considerable amount of research, investigations on the isostructural $Ca_2Co_2O_5$ has been more limited due to the difficult synthesis of the material [21–23]. To calculate the total energy of $Ca_2Co_2O_5$ we have considered the atomic positions from those reported for $Ca_2Fe_2O_5$ (unit cell $Ca_8Co_8O_{20}$) [24].

Monoclinic $Ca_3Co_4O_9$ (Fig. 1b) is a misfit compound built up from layers of rocksalt Ca_2CoO_3 (RS) and hexagonal CoO_2 (HX). The periodicities of the RS-Ca_2CoO_3 and HX-CoO_2 subsystems along the *b* direction are incommensurate with each other. As a result, $Ca_3Co_4O_9$ can be stoichiometrically expressed as $(Ca_2CoO_3)(CoO_2)_{b1/b2}$, where *b*1 and *b*2 correspond to the periodicities of the RS and HX subsystems along the incommensurate *b* direction, respectively [25]. Thus $Ca_3Co_4O_9$, can be formulated as $(Ca_2CoO_3)(CoO_2)_{1.62}$. Note that the formal Co oxidation state is +3. Calculations of such misfit compound would require a very large cell to be simulated, thereby a convenient route is utilizing an approximation to the $(Ca_2CoO_3)(CoO_2)_{1.62}$ formulae. Asahi et al. carried out the first ab initio calculations on $Ca_3Co_4O_9$ within the framework of density functional theory (DFT) [26]. Using an approximate unit cell of composition $(Ca_2CoO_3)(CoO_2)_{1.5}$ they performed a comprehensive study of the structural, electronic, magnetic, and thermoelectric properties of $Ca_3Co_4O_9$. More recently Rébola et al. [27] extended this investigation using the GGA + *U* approximation and considering four consecutive $(Ca_2CoO_3)(CoO_2)_{b1/b2}$ approximants of increasing supercell sizes (namely, the 3/2, 5/3, 8/5, and 13/8) the smallest of which is the one considered by Asahi et al.; $(Ca_2CoO_3)(CoO_2)_{1.5}$. They found that the size of the rational approximant as a structural model for the incommensurate $Ca_3Co_4O_9$ plays a minor role in the calculated results. In particular, even a relatively small 3/2 approximant does a good job in modelling the essential electronic properties of $Ca_3Co_4O_9$. In this work we have investigated the electrochemical properties of $Ca_3Co_4O_9$ considering the approximate $(Ca_2CoO_3)(CoO_2)_{1.5}$ composition with the cell used by Ashai et al. which contains four formula units: $(Ca_2CoO_3)_4(CoO_2)_6$. Thus, the formulae of this crystal cell can be written as $Ca_8Co_{10}O_{24}$ (or $Ca_4Co_5O_{12}$ where Co is in a formal oxidation state of +3.2).

The monodimensional structure of $Ca_3Co_2O_6$ (Fig. 1c) crystallizes in K_4CdCl_6-type structure (S.G. *R*-3*c*). The Co−O atoms form chains of alternating face-sharing CoO_6 octahedra (Oh) and CoO_6 trigonal prisms (TP) along the hexagonal c axis. The chains are separated by eight coordinated calcium atoms. The resulting short metal-metal intra-chain distance (2.59 Å) compared to the inter-chain distance (5.24 Å) reinforces the 1D character of the structure. Along the c axis each Co chain is surrounded by six chains constituting a hexagonal pattern in the basal plane. $Ca_3Co_2O_6$ belongs to the homologous series of monodimensional oxides with general formula $Ca_{n+2}CoCo'_nO_{3n+3}$, with Co and Co′ corresponding to ions in prismatic and octahedral coordination, respectively [28,29]. The initial atomic positions for $Ca_3Co_2O_6$ were taken from [30]; the cell comprises two unit formulae ($Ca_6Co_4O_{12}$).

2. Methodology

The calculations have been performed using the ab-initio total-energy and molecular dynamics program VASP (Vienna ab-initio simulation program) developed at the Universität Wien [31]. Total energy calculations based on Density Functional Theory (DFT) were performed within the General Gradient Approximation (GGA), with the exchange and correlation functional form developed by Perdew, Burke, and Ernzerhof (PBE) [32]. The interaction of core electrons with the nuclei is described by the Projector Augmented Wave (PAW) method [33]. The O ($2s^2$, $2p^4$), Ca ($3p^6$ $4s^2$) and Co ($3d^7$ $4s^2$) are taken as valence

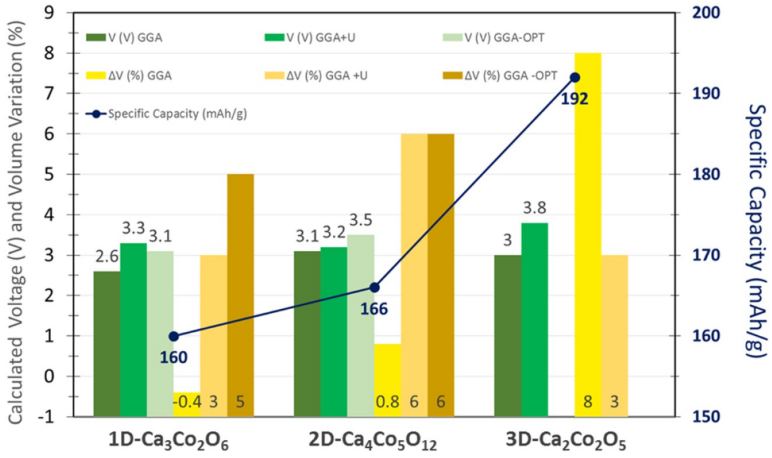

Fig. 2. Calculated average voltage, volume variations and specific capacity associated with the reactions (1)–(3). The volume variation is defined as (($V_{initial} - V_{Co}^{4+}$ phase) / $V_{initial}$) × 100.

states. The energy cut off for the plane wave basis set was kept fix at a constant value of 600 eV throughout the calculations. The integration in the Brillouin zone is done on an appropriate set of k-points determined by the Monkhorts-Pack scheme to ensure a numerical convergence error of < 10 meV/f.u. All crystal structures were fully relaxed (atomic positions, cell parameters and volume) within a force convergence criterion of 0.02 eV/Å. Spin polarized calculations were performed in all cases. The formal oxidation state of transition-metal ions can be determined by integrating the spin-polarization density in a sphere around the ion [34]. The final energies of the optimized geometries were recalculated to correct the changes in the basis set of wave functions during relaxation.

Calcium cobalt-oxides materials display complex magnetic, optical and electronic properties, which are difficult to capture with DFT methods. Previous computational works suggest that strong electron-electron correlation plays an important role in $Ca_3Co_2O_6$ and $Ca_4Co_3O_9$ materials, and the performance of GGA/GGA + *U*/hybrid functional methods has been matter of debate [26,27,35–41]. Most of the results support that the necessary ingredient for obtaining agreement with photoemission experiments, magnetic and electrical measurements is to take the correlations into account. It should be however underlined that other reports advice that the GGA is a better approximation than the GGA + U for some Co-oxides such as layered M_xCoO_2 (M = Li, Na [42], Mg, Ca) [43] and $Ca_3Co_2O_6$ [36,38]. In this work the total energies of the GGA-optimized compounds have been calculated using the GGA + *U* method, following the simplified rotationally invariant form of Dudarev et al. [44] with $U = 4$ eV and $J = 1$ eV for the Co-*d* states. This choice of $U_{eff} = 3$ eV is consistent with previous works in Co-oxides [35,36,45,46]. For a better description of the van der Waals interactions, additional calculations for the 1D and 2D systems were also performed using the optB86b-vdW exchange-correlation functional (hereafter GGA-OPT) [47].

The crystal models for the fully deintercalated phases were constructed removing all the Ca ions from the relaxed structures of the initial oxides. To simulate the crystal structure of the possible half-deinserted compounds it is necessary to establish and ordered pattern within Ca ions and vacancies. We created 14 and 10 Ca-vacancy arrangements for half-decalciated 3D-$CaCo_2O_5$ and 2D-$Ca_4Co_5O_{12}$, respectively, using the CASM software package [48,49]. To simulate the intermediate phases $Ca_{3x}Co_2O_6$ ($0 < x < 0.5$) we have constructed Ca/vacancies configurations within the unit cell of $Ca_3Co_2O_6$. The three possible models for x = 0.5 ($Ca_{1.5}Co_2O_6$) and x = 0.6667 ($Ca_2Co_2O_6$), and the one for x = 0.833 ($Ca_{2.5}Co_2O_6$) have been computed. In addition we have calculated the total energy of $Ca_2Co_2O_6$ within the crystal structure of 1D-$BaCoO_3$, which is the structure of the n = ∞ member of the $Ca_{n+2}CoCo'_nO_{3n+3}$ family [50].

The Ca^{2+} mobility in the three cobalt oxides is investigated using the Nudged Elastic Band method (NEB) as implemented in VASP [51]. NEB calculations have been carried out at the dilute limit x ~ 1, that is, the migration of a single vacancy in an otherwise fully inserted structure. To attain the dilute limit, we used superstructures of the unit cells that guarantee a minimum interaction between defects: 3D-$Ca_{31}Co_{32}O_{80}$ (2 × 1 × 2 of the unit cell), 2D-$Ca_{23}Co_{30}O_{72}$ (3 × 1 × 1 of the unit cell) and 1D-$Ca_{17}Co_{12}O_{36}$ (unit cell in hexagonal setting). Constant volume calculations were performed within the GGA approximation for five intermediate images initialized by linear interpolation between the two fully relaxed end-points. To calculate the energy at the saddle point, cubic splines were fit through the relaxed images along each hop.

3. Results and discussion

a) Voltage-composition curves of Co compounds vs Ca

For all the initial phases the GGA, GGA + U and GGA-OPT approximations yield lattice parameters differing with the experimental in < 5% (see tables in S.I.). The formal oxidation state of Co ions is +3 in $Ca_3Co_2O_6$ and $Ca_2Co_2O_5$, and +3.2 in $Ca_4Co_5O_{12}$, therefore Ca deintercalation from these phases implies the oxidation to Co^{4+} according with the reactions:

3D structure: $Ca_2Co_2O_5 \rightarrow CaCo_2O_5 + Ca$ (1)

2D structure: $Ca_4Co_5O_{12} \rightarrow Ca_2Co_5O_{12} + 2Ca$ (2)

1D structure: $Ca_3Co_2O_6 \rightarrow Ca_2Co_2O_6 + Ca$ (3)

As described in the Methodology section, several crystallographic models for the Co^{4+} phases have been investigated for each system (see S.I. for more details). The calculated average voltages for Ca deinsertion considering the most stable configuration found out of these Co^{4+} models are given in Fig. 2. Regardless the expected GGA vs. GGA + U differences, the potentials for Co^{3+} oxidation to Co^{4+} fall in the range 3–4 V. Palacín et al. demonstrated that Ca ions can be irreversibly extracted from $Ca_3Co_2O_6$ at c.a. 3.5 V, however, comparison with the computed voltage is biased by the large and undetermined overpotential of the electrochemical cells [14]. Fig. 2 also shows the specific capacity and volume variations associated to reactions (1)–(3). Importantly, the volume variation is quite small for the three oxides (maximum 8%), and much below the prediction for other materials, such as spinels [52] or perovskites [11]. It follows the trend of volume

reduction as Ca ions are removed from the structure.

Further Ca deinterclation beyond the oxidation to Co^{4+} is predicted at too high operating voltages (above 3.8 V, see Fig. S.1.) exceeding the stability limit of the reported electrolytes allowing reversible calcium plating/stripping [53,54]. Therefore, the oxidation state of Co ions, and not the amount of Ca ions in the compounds, limits the practical specific capacity of these materials.

b) Calcium diffusion

Cation diffusion in the active material is a necessary pre-requisite for electrochemical activity. Factors controlling diffusion are based on crystal chemistry: the existence of suitable Ca migration pathways within the structure, the topology around the diffusing ion, and the electrostatic interactions between the diffusing cation and the lattice constituents. The migration energy barriers, which can be extracted from DFT calculations, provide an approximate estimate of the ionic diffusivity. For an optimum electrode performance (C/2 rate) the migration barriers should be below 0.5 eV for micrometer particles and 0.625 eV for nanosized particles [4,6].

3D-$Ca_2Co_2O_5$. In a previous investigation we found calculated energy barriers exceeding 2 eV for Ca diffusion in perovskite materials [11]. Fig. 3a depicts possible Ca pathways in the brownmillerite structure. In the *b* axis, interconnect Ca sites form a channel where Ca diffusion would require the combination of two hops labelled as 1 and 2. Several calculation attempts failed to reach convergence for path 2. For path 1 the calculated energy barrier is 2.3 eV, which is not surprising since the path's topology is equivalent to that in the perovskite structure. This large barrier impedes Ca diffusion along this channel.

Diffusion in the *ac* plane, consisting of tetrahedral [CoO_4] units, might occur along jumps 3, 4 (arrows in Fig. 3a) and their combination. Pathway 4 is particularly interesting; the oxygen vacancies respective to the perovskite structure condense creating a zig-zag channel for potential Ca motion (red dashed line in Fig. 3a). The calculated energy barrier for path 3 (2 eV) is or the same order than in the perovskite. Noteworthy, the barrier lowers to 1.3 eV for pathway 4 (see Fig. 3b). In this pathway the initial and final Ca sites share edges, being connected through a site that does not share any face with the Co—O polyhedra. This contrasts with the perovskite structure, where the intermediate site shares a face with the transition metal octahedral, resulting in high electrostatic Ca-transition metal repulsions [11]. Therefore, the oxygen vacancies in the brownmillerite structure produce a more favourable topology around the diffusing Ca ion thereby reducing the migration barrier from 2 eV to 1.3 eV.

2D-$Ca_4Co_5O_{12}$ ($Ca_3Co_4O_9$). Fig. 4a displays the two-dimensional pathway for Ca diffusion in the *ab* plane, projected on the Co—O layers above and below the Ca—O layer. Because of the mismatch between the RS and HX subsystems, the initial Ca ion (in pink) is displaced from the tetrahedral site of the HX-layer. This produces an energy difference of 0.4 eV between the initial and final Ca sites. To the best of our knowledge, this is the first time that ionic diffusion in a misfit compound is investigated by DFT methods, and the significance of the cell approximant necessitates a profound analysis, which is out of the scope of the present investigation. With the approximant utilized in this work, the calculated energy landscape (Fig. 4b) displays a minima in between the two Ca-sites with an overall barrier of 0.9 eV. Additional calculations using the climbing image nudged elastic band method [55,56] give equivalent results (blue circles in Fig. 4b). Although this energy barrier is substantially below those reported for other oxides, it exceeds the aforementioned tolerable limit for high rate cathode performance [4]. More computational and experimental work is needed to either discard or confirm the suitability of $Ca_3Co_4O_9$ as low-rate cathode material.

1D-$Ca_3Co_2O_6$. In this structure, the Ca ions form an interconnected 3D network. We have calculated the barrier for Ca^{2+} diffusion along the three possible directions, considering the simplest Ca^{2+} diffusion mechanism where a Ca^{2+} ion jumps to an empty neighboring site (see Fig. 5a). Paths 1 and 2 have calculated energy barriers of 0.9 eV (Fig. 5b), while mobility in path 3 in prohibited by an energy barrier exceeding 3 eV. Fig. 5c sketches the different topology of each path, highlighting the common feature of a TP-Co sharing a face with the intermediate available site in all paths. The energy barriers can be explained considering the factors previously discussed: (i) the electrostatic repulsion with the nearest Co^{3+} ions that may penalize the occupation of the intermediate site and (ii) the large barriers associated with short Ca—O distances along the diffusion path. Path 1 connects Ca ions along the *c* axis: the diffusing Ca^{2+} ions can pass across a quadrangular face with Ca—O distances in the range 2.16–2.34 Å to occupy the intermediate six-coordination site. In path 2 the Ca also cross a face with Ca—O distances of 2.12–2.32 Å. In path 3 the proximity of the Co

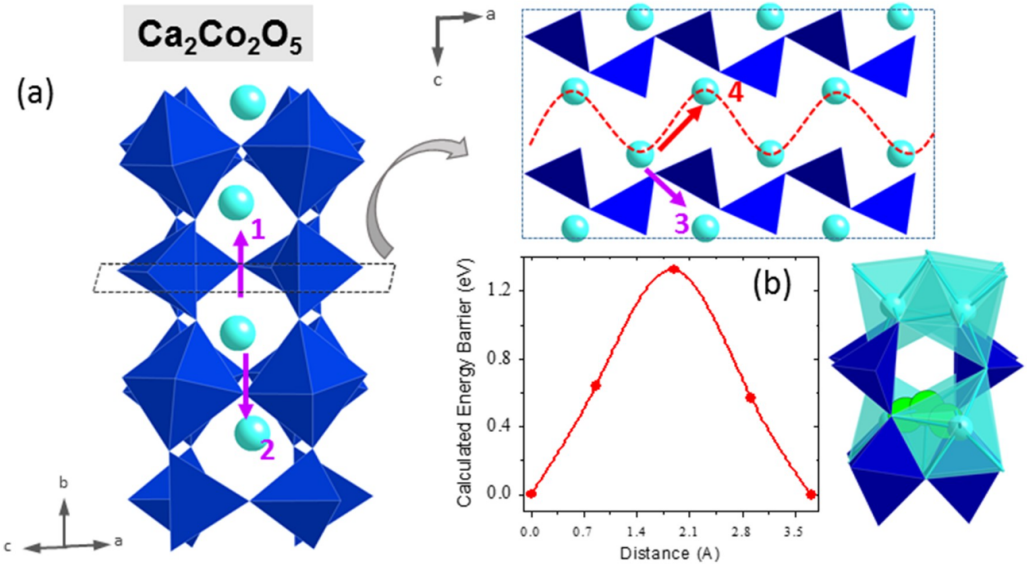

Fig. 3. (a) Pathways for Ca diffusion in $Ca_2Co_2O_5$ structure along the *b* axis and in the *ac* plane. The arrows indicate possible hopping mechanism from occupied to empty Ca sites (b) Calculated energy barrier for pathway 4. Color code: Ca light blue, Co dark blue. (For interpretation of the references to color in this figure legend, the reader is referred to the web version of this article.)

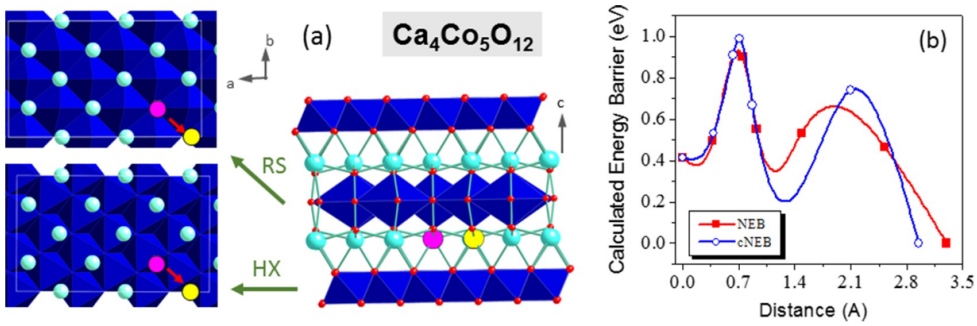

Fig. 4. (a) Pathway for Ca diffusion in the $Ca_4Co_5O_{12}$ structure, projected on the Co−O planes of the rocksalt (RS) and hexagonal (HX) subsystems. Color code: Ca light blue, Co dark blue. The red arrow indicates the hop from an occupied Ca site (in pink) to a vacant Ca site (in yellow) (b) Calculated energy barrier migration for a Ca ion at the dilute limit in a $Ca_{23}Co_{30}O_{72}$ supercell, within the NEB method (red squares) and the cNEB method (blue circles). (For interpretation of the references to color in this figure legend, the reader is referred to the web version of this article.)

ions forces the diffusing Ca to move across the oxygen-oxygen dumbbell (with very short Ca−O distances of 2.02 Å) hence raising the energy barrier.

c) Calcium de-insertion from $Ca_3Co_2O_6$

A recent experimental work [14] proves that the deinsertion of c.a. 1 mol Ca ions from $Ca_3Co_2O_6$ produces a modulated structure of composition $Ca_{2.3}Co_2O_6$ member of the homologous series $Ca_{n+2}CoCo'_nO_{3n+3}$, (Co and Co′ occupying, respectively, prismatic and octahedral sites). The simulation of this complex modulated structure is out the scope of this work. Thus, to gain some insights to the

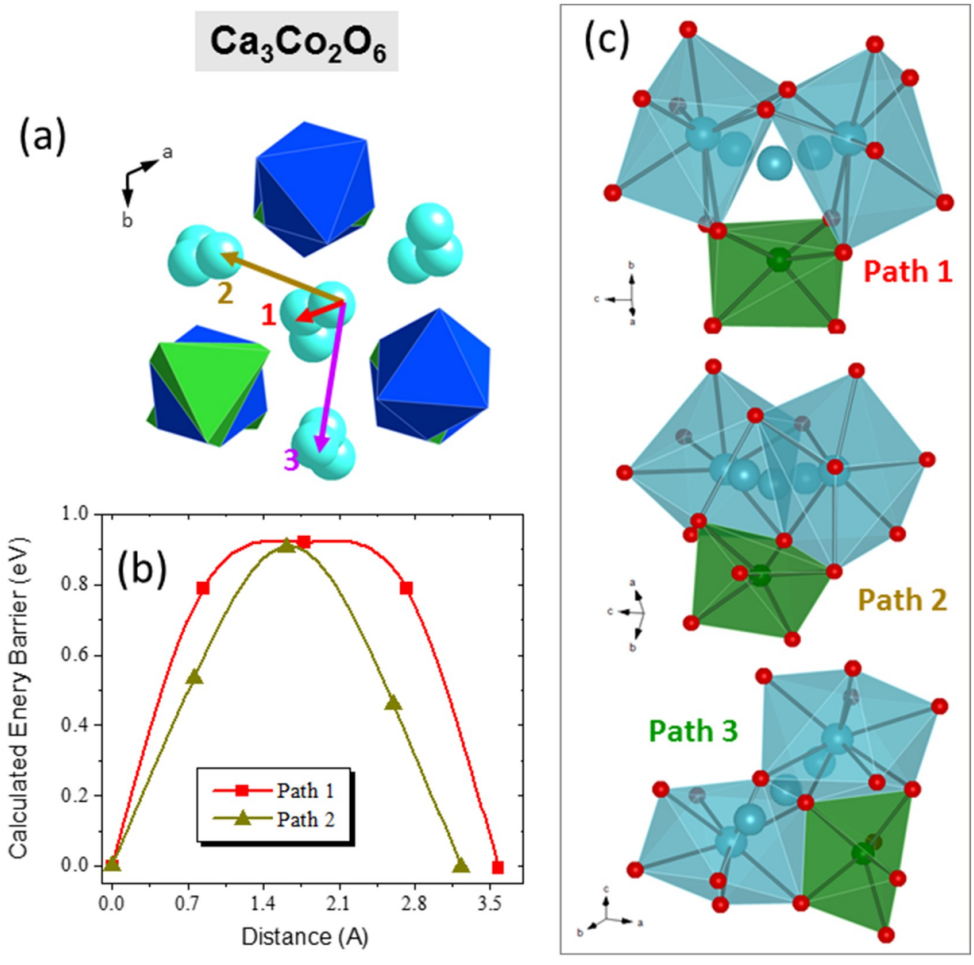

Fig. 5. (a) Investigated pathways for Ca diffusion in $Ca_3Co_2O_6$ structure. (b) Calculated energy barrier for paths 1 and 2 in a $Ca_{17}Co_{12}O_{36}$ supercell. (c) Topological analysis for each path. Color code: Ca light blue, octahedral Co dark blue, trigonal prismatic Co green, O red. (For interpretation of the references to color in this figure legend, the reader is referred to the web version of this article.)

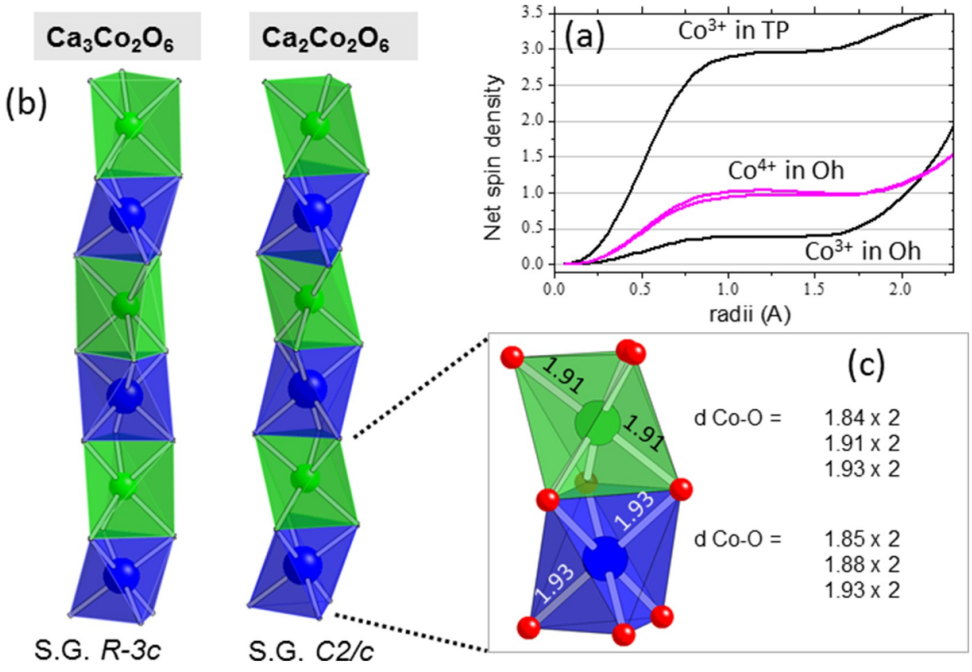

Fig. 6. (a) Unpaired charge density in $Ca_3Co_2O_6$ (black) and $Ca_2Co_2O_6$ (pink) phases. (b) Co chains along the hexagonal c axis in the optimized structures of $Ca_3Co_2O_6$ and $Ca_2Co_2O_6$. In $Ca_3Co_2O_6$ the Co chains are built by alternating face-sharing CoO_6 octahedra (in blue) and trigonal prisms (in green). Upon Ca deinsertion the trigonal prismatic sites evolve towards distorted octahedral. (c) Detail of the Co−O distances in the octahedral of $Ca_2Co_2O_6$. (For interpretation of the references to color in this figure legend, the reader is referred to the web version of this article.)

decalciation reaction of $Ca_3Co_2O_6$ and its reversibility, we have analyzed three models for the decalciated structures; the most stable Ca/vacancy configurations $Ca_{3x}Co_2O_6$ with x = 0.833 ($Ca_{2.5}Co_2O_6$) and x = 0.6667 ($Ca_2Co_2O_6$) and the hypothetical $BaCoO_3$-like $Ca_2Co_2O_6$. The latter is isostructural with $BaCoO_3$, this is to say, the n = ∞ member of the homologous series with all Co ions in octahedral sites.

As aforementioned, the Co chains in $Ca_3Co_3O_6$ are built by alternating face-sharing CoO_6 octahedra and trigonal prisms along the hexagonal *c* axis. Previous works [35,36,41,57] concluded that the Oh-Co^{3+} have nearly nonmagnetic contribution (Low Spin t_{2g}^6), while the TP-Co^{3+} are in a High Spin state of ~3 μB/Co. In good agreement, in the present work, the analysis of the crystal structure and unpaired charge density around the Co ions (see Fig. 6a) yielded two types of Co^{3+} ions; LS-Oh and HS-TP. A scheme of the *d*-configuration for both TP-Oh-Co^{3+} related to crystal field energy splitting (CFSE) is provided in Fig. S.2. Basic CFSE arguments indicates that a Co^{3+} ion is more stable in a LS-Oh than in HS-TP coordination. Indeed, Hoffmann et al. [58] pointed out that the preference for the octahedron vs the trigonal prims will be maximal for the low spin d^6 configuration. Their extended Hückel calculations on metal complexes gave for $Cr(CO)_6$ (a prototype for d^6 configuration) an energy for the octahedron 1.3 eV lower than that for an idealized prism.

DFT data indicates that Ca deintercalation has a notorious effect in the Co−O skeleton of $Ca_3Co_2O_6$. Fig. 6b shows the Co chains in the $Ca_3Co_2O_6$ and $Ca_2Co_2O_6$ crystal structures. Upon deintercalation the trigonal prism sites evolve to distorted octahedral coordination, thereby in the optimized $Ca_2Co_2O_6$ structure all the Co^{4+} ions reside in octahedral sites. The coordination sphere presents three sets of Co−O distances, which are aligned in the structure (see Fig. 6c). This distortion is related to a LS-Co^{4+} t_{2g}^5 electronic configuration, as inferred from the unpaired spin density around Co centers (Fig. 6a). Importantly, the same features are observed independently on the methodology (GGA, GGA + *U* or GGA-OPT). Results for the optimized structure of $BaCoO_3$-like $Ca_2Co_2O_6$ also evinced only octahedral-coordinated LS-Co^{4+} t_{2g}^5 ions. Note that the Co-($t_{2g}^5e_g^0$) configuration has also been found in 1D-$BaCoO_3$ [59]. Finally, in the optimized structure of $Ca_{2.5}Co_2O_6$ half of the Co-TP retain its coordination, and the other half distort to Oh. These results are in agreement with the deinserted samples being members of the homologous series $Ca_{n+2}CoCo'_nO_{3n+3}$. Importantly, once Co^{4+} ions adopt the octahedral coordination, a CFSE penalty accompanies the recovering of the TP-Co^{3+} ion upon subsequent Ca intercalation in $Ca_2Co_2O_6$ or $Ca_{2.5}Co_2O_6$. In addition, Ca deinsertion also affects the Ca-sublattice of $Ca_3Co_2O_6$. The analysis of the two optimized $Ca_2Co_2O_6$ and in the $BaCoO_3$-like structure reveals that the Ca ions rearrange from their initial sites, attaining a distinct coordination polyhedra (see Fig. S.3.).

The above results indicate that Ca deinsertion from $Ca_3Co_2O_6$ is not a topotactic reaction and that a phase transformation takes place upon Ca deinsertion. The characteristic electronic structure of $Ca_3Co_2O_6$ disappears due to the oxidation of HS-TP Co^{3+} to LS-Oh Co^{4+} and the Ca ions rearrange in a new sublattice. Therefore, Ca intercalation in $Ca_2Co_2O_6$ to recoup the initial $Ca_3Co_2O_6$ structure seems unlikely. Yet, the new phase $Ca_2Co_2O_6$ could uptake Ca ions if favourable pathways for Ca migration were available in the structure. For completeness we have evaluated the energy barriers for Ca hopping in the $BaCoO_3$-like $Ca_2Co_2O_6$ (see Fig. 7). The pathway along the *c* direction where the Ca ion exit across a triangular face is prohibited with an activation barrier larger than 2 eV. In the zig-zag pathway (labelled as 2 in Fig. 7) the diffusing Ca ions passes across a quadrangular window, with an activation energy of 1.1 eV. These results suggest that Ca mobility might be hindered in the oxidized $Ca_2Co_2O_6$ phase respective to the initial $Ca_3Co_2O_6$.

4. Conclusions

This work comprises the DFT investigation of calcium deinsertion from the cobalt-oxide frameworks of 1D-$Ca_3Co_2O_6$, 2D-$Ca_4Co_5O_{12}$ and 3D-$Ca_2Co_2O_5$ materials, in order to evaluate their electrode

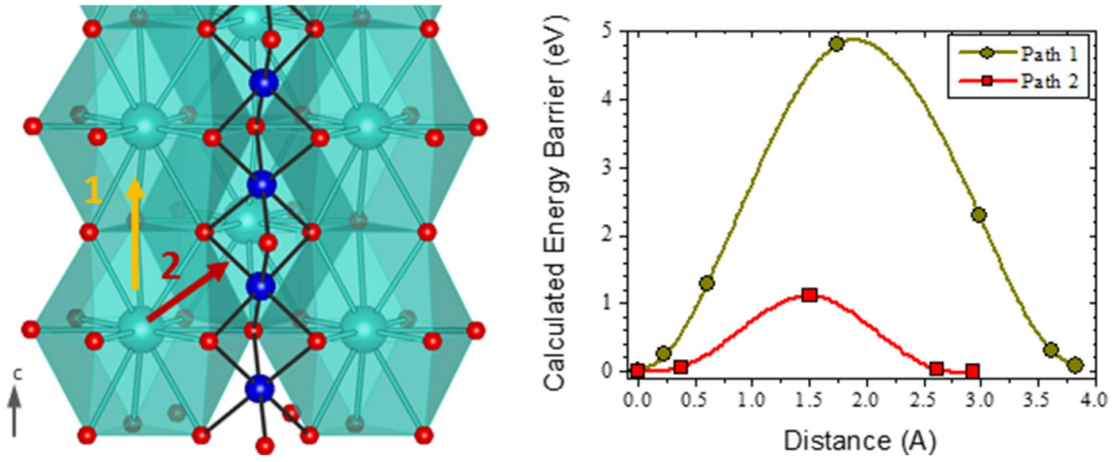

Fig. 7. Ca diffusion pathways and respective calculated energy barriers for the $BaCoO_3$-like $Ca_2Co_2O_6$ structure. A supercell $Ca_{23}Co_{24}O_{72}$ is used in the calculations. Color code: Ca light blue, Co dark blue, O red. (For interpretation of the references to color in this figure legend, the reader is referred to the web version of this article.)

characteristics for Ca-based batteries. For the three materials, the Co^{3+}/Co^{4+} redox couple falls in the 3–4 voltage window, being compatible with the known electrolytes. A positive finding is the low volume variation associated to the Ca deinsertion reactions (below 8%). The calculated energy barriers for Ca^{2+} migration (1.3 eV for the 3D, and 0.9 eV for both the 2D and 1D oxides) are indicative of a hampered Ca diffusivity in these materials. Despite these barriers are considerably lower than the reported for other oxides, they are still too high as to permit a good Ca diffusion, thereby impeding a fast kinetics for the deintercalation reaction. Yet, some electrochemical activity might be expected at low rates, as experimentally confirmed for $Ca_3Co_2O_6$ at C/200 rate [7]. In that line, 2D-$Ca_3Co_4O_9$ is other interesting material for further experimental and computational investigations.

Unsurprisingly, average insertion voltages, volume variation and theoretical specific capacities are not correlated with the lattice dimensionality. Regarding diffusion, layered (2D) materials are attractive as Ca-cathodes since the expandable interlayer space might facilitate Ca^{2+} intercalation. Yet, we found no evidence to expect a superior cathode performance for 1D/2D structures, at least for the present case where the deliverable specific capacity is determined by the redox couple, and some Ca ions will unavoidably remain in the decalciated-phases. Excluding the potential benefit of an empty interlayer/interchain space expansion, our results support that the local topology rather than the dimensionality is the main factor in Ca diffusion.

The reversibility of the Ca intercalation reactions is a major concern already remarked in the experimental investigations of $CaSi_2$ [60], TiS_2 [7], MoO_3 [61] and $Ca_3Co_2O_6$ [14]. The four materials display electrochemical activity, associated to Ca extraction or insertion, but with the common feature of a poor or negligible reversibility. Advances in experimental protocols and set-up are mandatory to discern whether irreversibility obeys to inherent properties of the cathode materials, or to issues related to the electrolyte and interfaces. In the case of 1D-$Ca_3Co_2O_6$, the present investigation discloses that Ca-deintercalation drastically modifies the electronic/crystal structures as well as the existing Ca-diffusion pathways. This phase transformation upon Ca deinsertion (Co^{3+} oxidation) may compromise the reversible capacity of $Ca_3Co_2O_6$ as cathode material.

Acknowledgements

Funding from the European Union's Horizon 2020 research and innovation programme H2020 FETOPEN-1-2016-2017 (CARBAT, grant agreement no. 766617) and from Toyota Motor Europe are acknowledged. Valuable comments from M.R. Palacín are appreciated. The authors are grateful for access to the computational facilities from Universidad de Oviedo (MALTA-Consolider cluster) and I2-Basque Centre.

Appendix A. Supplementary data

Supplementary data to this article can be found online at https://doi.org/10.1016/j.ssi.2019.115004.

References

[1] J. Muldoon, C.B. Bucur, T. Gregory, Quest for nonaqueous multivalent secondary batteries: magnesium and beyond, Chem. Rev. 114 (2014) 11683–11720.
[2] R.J. Gummow, G. Vamvounis, M.B. Kannan, Y. He, Calcium-ion batteries: current state-of-the-art and future perspectives, Adv. Mater. 30 (2018) 1801702.
[3] D. Monti, A. Ponrouch, R.B. Araujo, F. Barde, P. Johansson, M.R. Palacin, Multivalent batteries - prospects for high energy density: II. Ca batteries frontiers in chemistry, Front. Chem. 7 (2019) 79.
[4] P. Canepa, G.S. Gautam, D.C. Hannah, R. Malik, M. Liu, K.G. Gallagher, K.A. Persson, G. Ceder, Odyssey of multivalent cathode materials: open questions and future challenges, Chem. Rev. 117 (2017) 4287–4341.
[5] A. Ponrouch, M.R. Palacin, On the road toward calcium-based batteries, Curr. Opin. Electrochem. 9 (2018) 1–7.
[6] Z. Rong, R. Malik, P. Canepa, G.S. Gautam, M. Liu, A. Jain, K. Persson, G. Ceder, Materials design rules for multivalent ion mobility in intercalation structures, Chem. Mater. 27 (2015) 6016–6021.
[7] D.S. Tchitchekova, A. Ponrouch, R. Verrelli, T. Broux, C. Frontera, A. Sorrentino, F. Barde, N. Biskup, M. Elena Arroyo-de Dompablo, M. Rosa Palacin, Electrochemical intercalation of calcium and magnesium in TiS_2: fundamental studies related to multivalent battery applications, Chem. Mater. 30 (2018) 847–856.
[8] M. Smeu, M.S. Hossain, Z. Wang, V. Timoshevskii, K.H. Bevan, K. Zaghib, Theoretical investigation of Chevrel phase materials for cathodes accommodating Ca^{2+} ions, J. Power Sources 306 (2016) 431–436.
[9] M. Liu, A. Jain, Z. Rong, X. Qu, P. Canepa, R. Malik, G. Ceder, K.A. Persson, Evaluation of sulfur spinel compounds for multivalent battery cathode applications, Energy Environ. Sci. 9 (2016) 3201–3209.
[10] M.E. Arroyo-de Dompablo, C. Krich, J. Nava-Avendano, N. Biskup, M. Rosa Palacin, F. Barde, A joint computational and experimental evaluation of $CaMn_2O_4$ polymorphs as cathode materials for Ca ion batteries, Chem. Mater. 28 (2016) 6886–6893.
[11] M.E. Arroyo-de Dompablo, C. Krich, J. Nava-Avendano, M.R. Palacin, F. Barde, In quest of cathode materials for Ca ion batteries: the $CaMO_3$ perovskites (M = Mo, Cr, Mn, Fe, Co, and Ni), Phys. Chem. Chem. Phys. 18 (2016) 19966–19972.
[12] G.S. Gautam, P. Canepa, R. Malik, M. Liu, K. Persson, G. Ceder, First-principles evaluation of multi-valent cation insertion into orthorhombic V_2O_5, Chem. Comm. 51 (2015) 13619–13622.
[13] M. Cabello, F. Nacimiento, J.R. González, G. Ortiz, R. Alcántara, P. Lavela, C. Pérez-Vicente, J.L. Tirado, Advancing towards a veritable calcium-ion battery: $CaCo_2O_4$ positive electrode material, Electrochem. Commun. 67 (2016) 59–64.
[14] D.S. Tchitchekova, C. Frontera, A. Ponrouch, C. Krich, F. Barde, M.R. Palacin, Electrochemical calcium extraction from 1D-$Ca_3Co_2O_6$, Dalton Trans. (2018)

11298–11302.
[15] Z. Zhao, J. Yao, B. Sun, S. Zhong, X. Lei, B. Xu, C. Ouyang, First-principles identification of spinel $CaCo_2O_4$ as a promising cathode material for Ca-ion batteries, Solid State Ionics 326 (2018) 145–149.
[16] E. Woermann, A. Muan, Phase equilibria in system CaO-cobalt oxide in air, J. Inorg. Nucl. Chem. 32 (1970) 1455.
[17] D. Sedmidubsky, V. Jakes, O. Jankovsky, J. Leitner, Z. Sofer, J. Hejtmanek, Phase equilibria in Ca-Co-O system, J. Solid State Chem. 194 (2012) 199–205.
[18] K.T. Jacob, P. Gupta, Oxygen potentials and phase equilibria in the system Ca-Co-O and thermodynamic properties of $Ca_3Co_2O_6$ and $Ca_3Co_4O_{9.163}$, J. Solid State Chem. 221 (2015) 57–65.
[19] C.N.R. Rao, J. Gopalakrishnan, K. Vidyasagar, A.K. Ganguli, A. Ramanan, L. Ganapathi, Novel metal oxides prepared by ingenious synthetic routes, J. Mater. Res. 1 (1986) 280–294.
[20] H. Tran, T. Mehta, M. Zeller, R.H. Jarman, Synthesis and characterization of mixed phases in the Ca-Co-O system using the Pechini method, Mat. Res. Bull. 48 (2013) 2450–2456.
[21] M.T. Anderson, J.T. Vaughey, K.R. Poeppelmeier, Structural similarities among oxygen-deficient perovskites, Chem. Mater. 5 (1993) 151–165.
[22] N. Sharma, K.M. Shaju, G.V.S. Rao, B.V.R. Chowdari, Mixed oxides $Ca_2Fe_2O_5$ and $Ca_2Co_2O_5$ as anode materials for li-ion batteries, Electrochim. Acta 49 (2004) 1035–1043.
[23] K. Vidyasagar, J. Gopalakrishnan, C.N.R. Rao, A convenient route for the synthesis of complex metal-oxides employing solid-solution precursors, Inorg. Chem. 23 (1984) 1206–1210.
[24] J. Berggren, Refinement of crystal-structure of dicalcium ferrite, $Ca_2Fe_2O_5$, Acta Chem. Scand. 25 (1971) 3616–3624.
[25] Y. Miyazaki, T. Miura, Y. Ono, T. Kajitani, Preparation and low-temperature thermoelectric properties of the composite crystal $[Ca_2(Co_{0.65}Cu_{0.35})_2O_4]_{0.624}CoO_2$, Jpn. J. Appl. Phys. 41 (2002) L849–L851.
[26] R. Asahi, J. Sugiyama, T. Tani, Electronic structure of misfit-layered calcium cobaltite, Phys. Rev. B 66 (2002) 155103.
[27] A. Rebola, R. Klie, P. Zapol, S. Ogut, First-principles study of the atomic and electronic structures of misfit-layered calcium cobaltite $(Ca_2CoO_3)(CoO_2)_{1.62}$ using rational approximants, Phys. Rev. B 85 (2012) 155132.
[28] K. Boulahya, M. Parras, J.M. Gonzalez-Calbet, The $A_{n+2}B_nB'O_{3n+3}$ family (B = B′ = Co): ordered intergrowth between 2H-$BaCoO_3$ and $Ca_3Co_2O_6$ structures, J. Solid State Chem. 145 (1999) 116–127.
[29] K. Boulahya, M. Parras, J.M. Gonzalez-Calbet, The orthorhombic $(Ba_8Co_6O_{18})_\alpha(Ba_8Co_8O_{24})_\beta$ series, a new family of monodimensional oxides, Chem. Mater. 12 (2000) 2727–2735.
[30] H. Fjellvag, E. Gulbrandsen, S. Aasland, A. Olsen, B.C. Hauback, Crystal structure and possible charge ordering in one-dimensional $Ca_3Co_2O_6$, J. Solid State Chem. 124 (1996) 190–194.
[31] G. Kresse, J. Furthmuller, Efficient iterative schemes for ab initio total-energy calculations using a plane-wave basis set, Phys. Rev. B 54 (1996) 11169.
[32] J.P. Perdew, K. Burke, M. Ernzerhof, Generalized gradient approximation made simple, Phys. Rev. Lett. 77 (1996) 3865–3868.
[33] P.E. Blöch, Projector augmented-wave method, Phys. Rev. B 50 (1994) 17953.
[34] J. Reed, G. Ceder, Charge, potential, and phase stability of layered $LiNi_{0.5}Mn_{0.5}O_2$, Electrochem. Solid-State Lett. 5 (2002) A145–A148.
[35] T.-R. Chang, H.-T. Jeng, C.-S. Hsue, Electronic structures of quasi-one-dimensional ferrimagnetic insulator $Ca_3Co_2O_6$, Comput. Phys. Commun. 182 (2011) 93–95.
[36] A. Villesuzanne, M.H. Whangbo, Comparative electronic band structure study of the intrachain ferromagnetic versus antiferromagnetic coupling in the magnetic oxides $Ca_3Co_2O_6$ and Ca_3FeRhO_6, Inorg. Chem. 44 (2005) 6339–6345.
[37] H. Wu, M.W. Haverkort, Z. Hu, D.I. Khomskii, L.H. Tjeng, Nature of magnetism in $Ca_3Co_2O_6$, Phys. Rev. Lett. 95 (2005) 186401.
[38] R. Vidya, P. Ravindran, H. Fjellvag, A. Kjekshus, O. Eriksson, Tailor-made electronic and magnetic properties in one-dimensional pure and Y-substituted $Ca_3Co_2O_6$, Phys. Rev. Lett. 91 (2003) 186404.
[39] S. Lemal, J. Varignon, D.I. Bilc, P. Ghosez, Thermoelectric properties of layered calcium cobaltite $Ca_3Co_4O_9$ from hybrid functional first-principles calculations, Phys. Rev. B 95 (2017) 075205.
[40] C. Mitra, R.S. Fishman, S. Okamoto, H.N. Lee, F.A. Reboredo, Ground-state and spin-wave dynamics in brownmillerite $SrCoO_{2.5}$; a combined hybrid functional and LSDA plus *U* study, J. Phys. Condens. Matter 26 (2014) 036004.
[41] Y. Zhang, E. Kan, H. Xiang, A. Villesuzanne, M.-H. Whangbo, Density functional theory analysis of the interplay between Jahn-Teller instability, uniaxial magnetism, spin arrangement, metal-metal interaction, and spin-orbit coupling in Ca_3CoMO_6 (M = Co, Rh, Ir), Inorg. Chem. 50 (2011) 1758–1766.
[42] M.D. Johannes, I.I. Mazin, D.J. Singh, Three-dimensional magnetic interactions in Na_xCoO_2: first-principles calculations and analysis of exchange mechanisms, Phys. Rev. B 71 (2005) 214410.
[43] M.D. Radin, A. Van der Ven, Stability of prismatic and octahedral coordination in layered oxides and sulfides intercalated with alkali and alkaline-earth metals, Chem. Mater. 28 (2016) 7898–7904.
[44] S.L. Dudarev, G.A. Botton, S.Y. Savrasov, Z. Szotek, W.M. Temmerman, A.P. Sutton, Electronic structure and elastic properties of strongly correlated metal oxides from first principles: LSDA + *U*, SIC-LSDA and *EELS* study of UO_2 and NiO, Phys. Status Solidi A 166 (1998) 429–443.
[45] L. Wang, T. Maxisch, G. Ceder, Oxidation energies of transition metal oxides within the GGA + *U* framework, Phys. Rev. B 73 (2006) 195107.
[46] M.E. Arroyo y de Dompablo, Y.-L. Lee, D. Morgan, First principles investigation of oxygen vacancies in columbite MNb_2O_6 (M = Mn, Fe, Co, Ni, Cu), Chem. Mater. 22 (2010) 906–913.
[47] J. Klimes, D.R. Bowler, A. Michaelides, Chemical accuracy for the van der Waals density functional, J. Phys. Condens. Matter 22 (2010) 022201.
[48] A. Van der Ven, J.C. Thomas, Q. Xu, B. Swoboda, D. Morgan, Nondilute diffusion from first principles: Li diffusion in Li_xTiS_2, Phys. Rev. B 78 (2008) 104306.
[49] A. Van der Ven, J.C. Thomas, Q. Xu, B. Swoboda, J. Bhattacharga, Linking the electronic structure of solids to their thermodynamic and kinetic properties, Math. Comput. Simul. 80 (2010) 1393.
[50] H. Taguchi, Y. Takeda, F. Kanamaru, M. Shimada, M. Koizumi, Barium cobalt trioxide, Acta Crystallogr. Sect. B: Struct. Sci. 33 (1977) 1298–1299.
[51] G. Mills, H. Jonsson, G.K. Schenter, Reversible work transition-state theory: application to dissociative adsorption of hydrogen, Surf. Sci. 324 (1995) 305–337.
[52] M. Liu, Z. Rong, R. Malik, P. Canepa, A. Jain, G. Ceder, K.A. Persson, Spinel compounds as multivalent battery cathodes: a systematic evaluation based on ab initio calculations, Energy Environ. Sci. 8 (2015) 964–974.
[53] A. Ponrouch, C. Frontera, F. Barde, M.R. Palacin, Towards a calcium-based rechargeable battery, Nat. Mater. 15 (2015) 169–172.
[54] D. Wang, X. Gao, Y. Chen, L. Jin, C. Kuss, P.G. Bruce, Plating and stripping calcium in an organic electrolyte, Nat. Mater. 17 (2018) 16–20.
[55] G. Henkelman, H. Jonsson, Improved tangent estimate in the nudged elastic band method for finding minimum energy paths and saddle points, J. Chem. Phys. 113 (2000) 9978–9985.
[56] G. Henkelman, B.P. Uberuaga, H. Jonsson, A climbing image nudged elastic band method for finding saddle points and minimum energy paths, J. Chem. Phys. 113 (2000) 9901–9904.
[57] T.A. Albright, J.K. Burdett, M.H. Whangbo, Orbital Interactions in Chemistry, 2nd edition, John Wiley & Sons, 2013.
[58] R. Hoffmann, J.M. Howell, A.R. Rossi, Bicapped tetrahedral, trigonal prismatic, and octahedral alternatives in main and transition group 6 coordination, J. Am. Chem. Soc. 98 (1976) 2484–2492.
[59] V. Pardo, P. Blaha, R. Laskowski, D. Baldomir, J. Castro, K. Schwarz, J.E. Arias, Ising-type behavior in the antiferromagnetic phase of $BaCoO_3$ from first principles, Phys. Rev. B 76 (2007) 165120.
[60] A. Ponrouch, D. Tchitchekova, C. Frontera, F. Bardé, M.E.A. Dompablo, M.R. Palacín, Assessing Si-based anodes for Ca-ion batteries: electrochemical decalciation of $CaSi_2$, Electrochem. Commun. 66 (2016) 75–78.
[61] M. Cabello, F. Nacimiento, R. Alcantara, P. Lavela, C. Pérez-Vicente, J.L. Tirado, Applicability of molybdite as an electrode material in calcium batteries: a structural study of layer-type Ca_xMoO_3, Chem. Mater. 30 (2018) 5853–5861.

Supplementary Information

Evaluation of cobalt oxides for calcium battery cathode applications

A. Torres[a], F. Bardé[b] and M. E. Arroyo-de Dompablo[a*]

[a] Departamento de Química Inorgánica, Facultad de Ciencias Químicas, Universidad Complutense de Madrid, 28040 Madrid, Spain

[b] Toyota Motor Europe, Research & Development, Advanced Material Research, Battery & FC, Technical Centre, Hoge Wei 33 B, B-1930 Zaventem, Belgium

*Corresponding author: e.arroyo@quim.ucm.es

TABLE S.1. Calculated vs experimental lattice parameters of $Ca_2Co_2O_5$ (S.G. *Pmna*)

Approximation	a (Å)	b (Å)	c (Å)	V (Å^3)
GGA	5.330	14.594	5.535	430.67
GGA+U	5.330	14.895	5.563	441.79
Experimental [1]	5.289	14.924	5.447	429.94

TABLE S.2. Calculated lattice parameters of $Ca_8Co_{10}O_{24}$ compared to previous DFT investigations and experimental ones.

Approximation	*a (Å)*	*b* (Å) (b_{RS}+1.5b_{HX})	*c (Å)*	β(º)
Experimental [2]	4.83	8.79	10.84	98.13
GGA [3]	4.89	8.77	10.92	98.14
GGA+U (U = 5 eV) [3]	4.81	8.67	10.86	98.11
GGA	4.88	8.74	10.89	98.13
GGA-OPT	4.82	8.68	10.78	97.89
GGA+U (U = 3 eV)	4.94	8.95	11.04	98.75
GGA+U (U = 5 eV)	4.89	9.04	11.04	98.83

TABLE S.3. Calculated vs experimental lattice parameters of $Ca_3Co_2O_6$ (S.G. *R-3c*)

Approximation	a,b,c (Å)	α, β, γ (º)	V (Å^3)
GGA	6.319	92.39	251.7
GGA-OPT	6.251	92.29	243.8
GGA+U (U_{eff} = 3 eV)	6.311	92.39	250.7
GGA+U (U_{eff} = 4 eV)	6.363	92.52	256.9
Experimental [4]	6.269	92.53	245.70

Calculation of formation energies and average voltages

To examine the relative stability of the respective Co^{4+} phases we have calculated the formation energy according to the general expression:

x Ca-Host + (1-x) Host → Ca_xHost (1)

where Host refers to the fully decalciated structure and Ca-Host is the starting material (fully calciated phase). Ca_xHost is the corresponding phase exhibiting Co^{+4} ions: 3D-$CaCo_2O_5$, 2D-$Ca_2Co_5O_{12}$ and 1D-$Ca_2Co_2O_6$. The formation energy of reaction (1) can be obtained from the respective total energies. For the three oxides we found negative formation energies indicating that the intermediate phases (Co^{4+} phases) are stable with respect to phase separation into the fully inserted and deinserted phases. The formation energies allow us to determine the ground state energy vs. composition curve (convex hull) (see figure S.1. a-c). The convex hull has several vertices at which characteristic ordered structures of Ca ions and vacancies appear. These ground states result in single phase regions in the voltage composition curve at 0 K. From the convex hull we can construct the voltage-composition profile (figure S.1. d-f) following the methodology described by Aydinol *et al.* [5]. Considering the intercalation reaction:

(x2-x1) Ca(s) + Ca_{x1}Host →Ca_{x2}Host (2)

the average intercalation voltage can be extracted from a total energy expression:

$$V(V) = \frac{-E_{TOTAL}(\mathrm{Cax2Host}) + E_{TOTAL}(\mathrm{Cax1Host}) + (x2 - x1)E_{TOTAL}(Ca)}{2F(x2 - x1)} \quad (3)$$

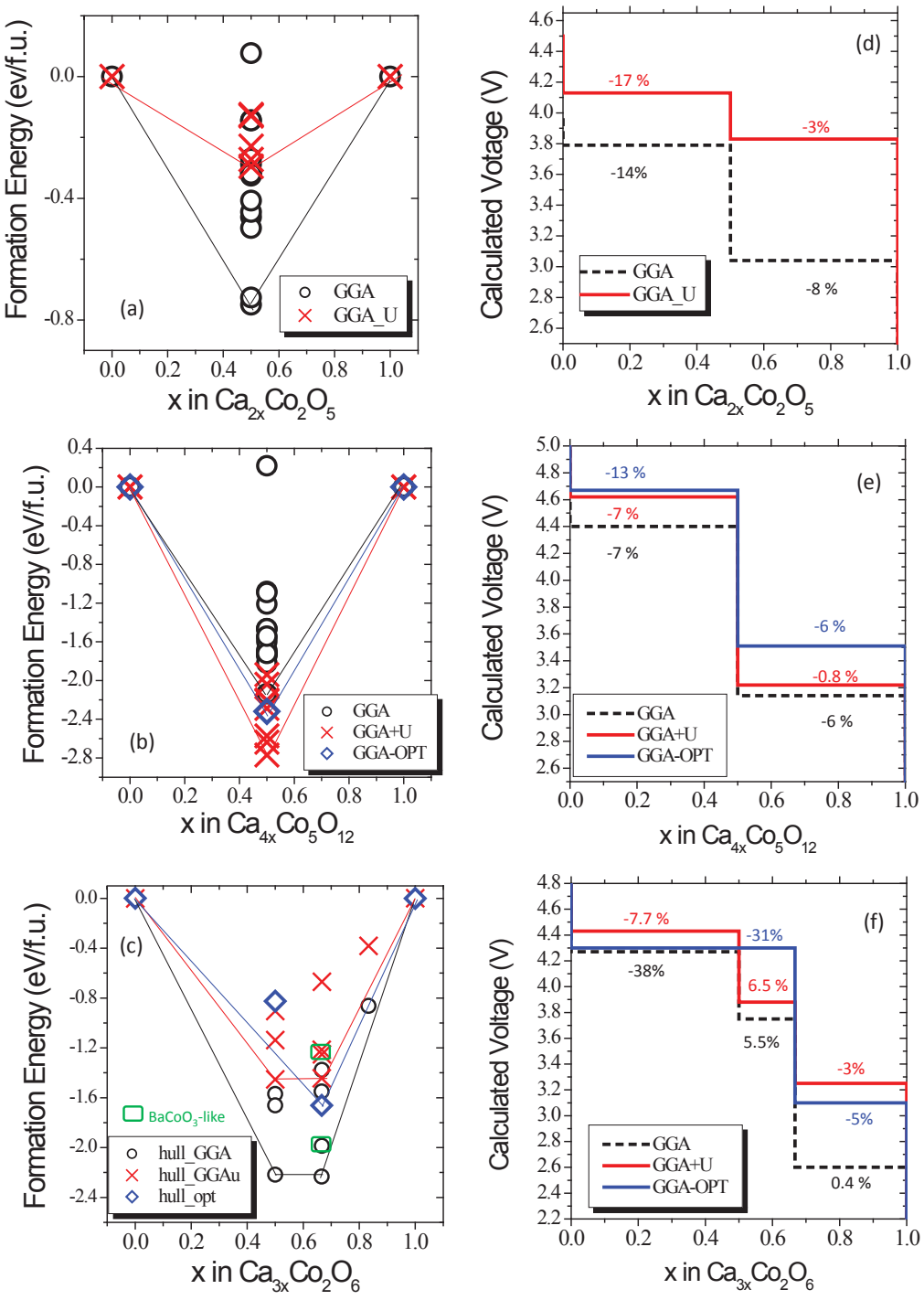

Figure S.1. (a-c). Calculated formation energies of ordered Ca-Co-O structures as a function of the Ca concentration. Blue for GGA-OPT, red for GGA+*U* (U_{eff} = 3 eV) and dashed-black for GGA. (d-f) Calculated sketch of the voltage – composition curve for the Ca-Co-O compounds. The volume variation between two consecutive single phases is given as percentage for the deinsertion process.

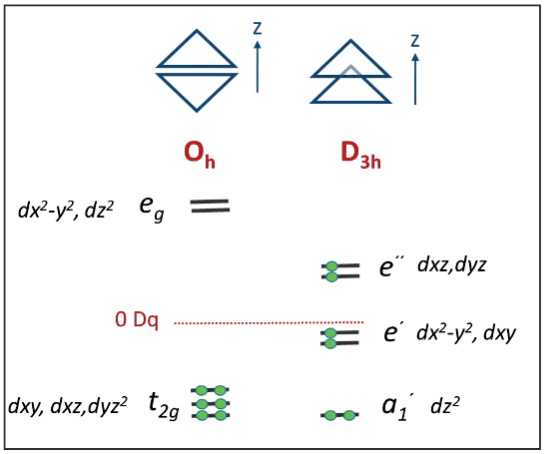

Figure S.2. Scheme of the *d*-electron configuration of a low spin- Co^{3+} ion in an undistorted octahedral site (left) and a high spin Co^{3+} ion in a regular trigonal prismatic site. Adapted from [6].

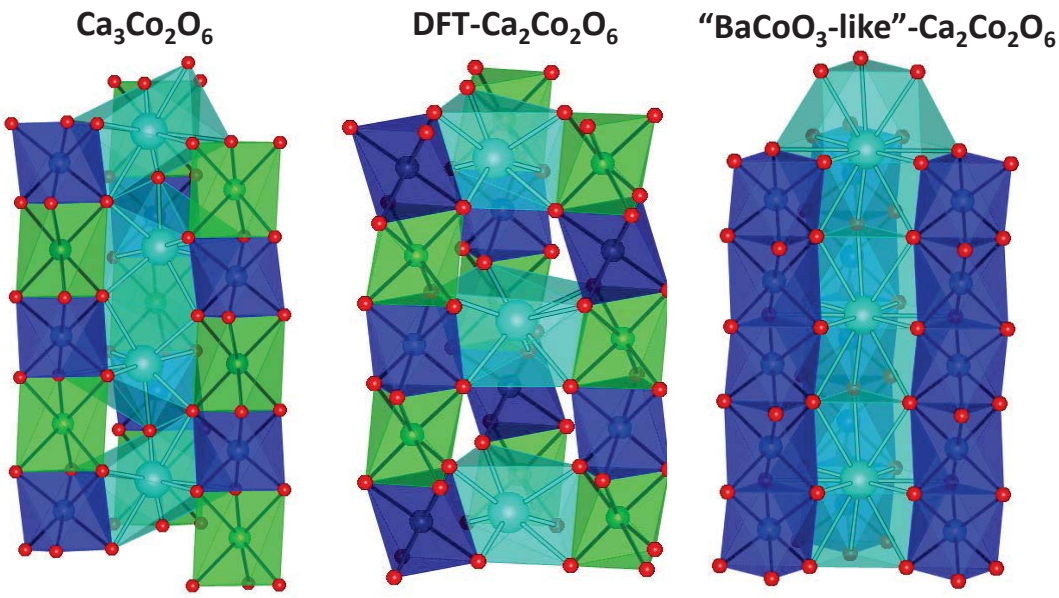

Figure S.3. View of the $Ca_3Co_2O_6$ and its decalciated structures along the *c* axis. Upon Co oxidation the Ca ions rearranged in the structure. Color code: Co in octahedral sites dark blue, Co in TP sites or derived from them in green, Ca light blue, O red.

References

[1] Zhang, J.; Zheng, H.; Malliakas, C. D.; Allred, J. M.; Ren, Y.; Li, Q. a.; Han, T.-H.; Mitchell, J. F., Brownmillerite *$Ca_2Co_2O_5$: Synthesis, Stability, and Re-entrant Single Crystal to Single Crystal Structural Transitions.* Chemistry of Materials **2014**, 26, 7172-7182.

[2] Miyazaki, Y.; Miura, T.; Ono, Y.; Kajitani, T., *Preparation and low-temperature thermoelectric properties of the composite crystal $[Ca_2(Co_{0.65}Cu_{0.35})_2O_4]_{0.624}CoO_2$*. Japanese Journal of Applied Physics Part 2-Letters **2002**, 41, L849-L851.

[3] Rebola, A.; Klie, R.; Zapol, P.; Ogut, S., *First-principles study of the atomic and electronic structures of misfit-layered calcium cobaltite $(Ca_2CoO_3)(CoO_2)_{1.62}$ using rational approximants*. Physical Review B **2012**, 85, 155132

[4] Fjellvag, H.; Gulbrandsen, E.; Aasland, S.; Olsen, A.; Hauback, B. C., *Crystal structure and possible charge ordering in one-dimensional $Ca_3Co_2O_6$.* Journal of Solid State Chemistry **1996**, 124 190-194.

[5] Aydinol, M. K.; Kohan, A. F.; Ceder, G.; Cho, K.; Joannopoulos, J., *Ab initio study of lithium intercalation in metal oxides and metal dichalcogenides*. Physical Review B **1997**, 56, 1354-1365.

[6] Hoffmann, R.; Howell, J. M.; Rossi, A. R., *Bicapped tetrahedral, trigonal prismatic, and octahedral alternatives in main and transition group six coordination*. Journal of the American Chemical Society **1976**, 98, 2484-2492.

CAPÍTULO 6

COMBINACIÓN DE DFT Y EXPERIMENTOS EN EL ESTUDIO DE $Ca_4Fe_9O_{17}$

Dalton Transactions

ROYAL SOCIETY OF CHEMISTRY

PAPER

View Article Online
View Journal | View Issue

Cite this: *Dalton Trans.*, 2020, **49**, 2671

Appraisal of calcium ferrites as cathodes for calcium rechargeable batteries: DFT, synthesis, characterization and electrochemistry of $Ca_4Fe_9O_{17}$†

Ashley P. Black, [a,b] Arturo Torres,[c] Carlos Frontera,[a,b] M. Rosa Palacín [a,b] and M. Elena Arroyo-de Dompablo *[c]

Received 9th December 2019,
Accepted 20th January 2020

DOI: 10.1039/c9dt04688g

rsc.li/dalton

Sustainability combined with high energy density prospects makes Fe-based oxides attractive as cathodes for calcium rechargeable batteries. This work presents a DFT evaluation of the $CaFe_{2+n}O_{4+n}$ ($0 < n < 3$) family, for which both the average intercalation voltage and the theoretical specific capacity decrease with the increasing n value. The term $n = 1/4$, $Ca_4Fe_9O_{17}$, meets the most appealing characteristics: a calculated average voltage of 4.16 V, a theoretical specific capacity of 230 mA h g^{-1} and the lowest energy barrier for Ca migration so far predicted for an existing oxide (0.72 eV). To overcome the previously reported synthesis difficulties, we employed a novel synthesis procedure in sealed quartz tubes followed by quenching in water. The XRD and SAED patterns of the prepared $Ca_4Fe_9O_{17}$ powder reveal a certain degree of stacking defects along the c axis. Attempts to deinsert Ca ions from $Ca_4Fe_9O_{17}$ by chemical means (NO_2BF_4 in ACN) and in electrochemical Ca cells were unsuccessful, although some hints of oxidation are observed in Li cells with the LP30 electrolyte. The suitability of $Ca_4Fe_9O_{17}$ as a Ca cathode is pending further studies utilizing Ca-electrolytes with high anodic stability.

Introduction

The Li-ion technology currently dominates the rechargeable battery market for portable electronics and appears to be a possible near term solution for applications such as electric vehicles and grid storage, in parallel with the storage of energy from renewable and intermittent sources – solar, wind, waves, *etc*. However, Li-ion batteries are currently approaching their fundamental limits in terms of energy density, which in addition to the limited supply of Li instigate the race for the development of alternative technologies exhibiting advantages in terms of energy density, safety and cost. Rechargeable batteries based on a Ca-metal anode are attractive given the abundance of calcium in the Earth's crust, the high capacity of calcium anodes (1340 mA h g^{-1}) and its negative reduction potential (only 170 mV above that of lithium metal).[1,2] Advances in the development of such batteries are intricate due to the lack of competitive cathode materials and electrolytes.[3,4] While recent findings demonstrate the feasibility of Ca anode operation using different electrolytes,[5–8] the identification of suitable cathode materials has been facing several roadblocks.[4,9,10] Limited reversible electrochemical Ca intercalation has been reported for a handful of compounds[4] (V_2O_5,[11] TiS_2,[12] MoO_3,[13] $Ca_{0.5}CoO_2$,[14] and manganese hexacyanoferrate[1]), all of them showing poor cycling, if any. Parallel experimental and computational investigations establish a link between the lack of reversible electrochemical activity (experimentally observed) and hampered Ca diffusion (computationally estimated).[15–20] In this regard, the poor diffusion of Ca^{2+} in inorganic structures is the major challenge for cathode discovery.[21] Compared to Li^+ diffusion, the hindrance to Ca mobility resides in the larger size of Ca^{2+} ions on one hand and its divalent charge on the other that increases the electrostatic repulsion/attraction with the neighbouring cations/anions in the structure.

Sustainable cathode materials should include abundant and non-toxic elements, and at the same time, comply with the high energy density requirements. These criteria prompted the investigation of light and abundant oxidizing 3d-transition

[a]*Institut de Ciència de Materials de Barcelona (ICMAB-CSIC) Campus UAB, E-08193 Bellaterra, Catalonia, Spain*
[b]*ALISTORE-ERI European Research Institute, CNRS FR 3104, Hub de l'Energie, 15 Rue Baudelocque, 80039 Amiens, France*
[c]*Departamento de Química Inorgánica, Facultad de Ciencias Químicas, Universidad Complutense de Madrid, 28040 Madrid, Spain.*
E-mail: e.arroyo@quim.ucm.es

†Electronic supplementary information (ESI) available: Table S1: DFT and lattice parameters, Fig. S1: calculated energy migration barrier for $CaFe_2O_4$, Table S2 and Fig. S2: summary of synthesis methods, Fig. S3: Rietveld refinement, and Fig. S4: electrochemistry and XRD of $Ca_2Fe_2O_5$. See DOI: 10.1039/C9DT04688G

metal oxides as cathodes for Ca batteries. So far several Mn oxides and polyoxoanionic compounds have been reported, going from the virtual spinel $CaMn_2O_4$[22] to the $CaMnO_3$ perovskite,[16] its reduced derivative -$Ca_2Mn_2O_5$,[23] the known $CaMn_2O_4$ polymorphs (marokite and its high pressure form),[15] a related oxidized phase, $CaMn_4O_8$,[23] and the minerals $K_{0.31}MnO_2$ $0.25H_2O$ (birnessite),[24] $Mg_{0.19}Na_{0.07}MnO_2$ $0.37H_2O$ (todorokite),[25] $CaMn(CO_3)_2$ (kutnahorite)[26] and $CaMnSi_2O_6$ (johannsenite).[26] In contrast, research on Fe oxides has been scarce; the perovskite $CaFeO_3$ and the related brownmillerite $Ca_2Fe_2O_5$ compounds have been only evaluated by computational means.[16,23] It was found that Ca-perovskites are not competitive materials due to hindered Ca mobility (a calculated energy barrier of 2 V).[16] In the brownmillerite structure the oxygen vacancies respective to the perovskite create a new pathway with much lower energy barrier (1 eV).[23] The present investigation turns to other known oxides in the Ca–Fe–O system with general formulae $CaFe_{2+n}O_{4+n}$ that might be worthy candidates (Fig. 1).

The crystal structure of $CaFe_2O_4$ (S.G. *Pmna*, no. 53)[27,28] consists of edge-sharing chains of MnO_6 octahedra, forming double rutile chains (see Fig. 1a). Each double-rutile chain is connected to two adjacent chains through edge-sharing oxygen. As a result, tunnels appear along the *b* axis where Ca ions reside in eight-fold coordination. The calcium ferrite $CaFe_{2+n}O_{4+n}$ family is formed by stacking along the *c* axis (S.G. *Cmcm*, no. 63) of blocks with the $CaFe_2O_4$ composition and blocks with the FeO composition (see Fig. 1b). Within this family, the compounds with n = 0, 1, 3/2, 2, 5/2, and 3 have been reported.[29,30] Interestingly, for n = 1/4, the compound $Ca_4Fe_9O_{17}$ crystallizes in a different structure (S.G. *C*2, no. 5), built up by layers of Fe atoms in edge-sharing FeO_6 octahedra and vertex-sharing Fe in trigonal-based bipyramid coordination (see Fig. 1c and d).[31] These hexagonal layers stack along the *c*-axis direction, being cross-linked by iron atoms in tetrahedral coordination. The $[FeO_4]$-tetrahedra are connected in the *ab* plane of the structure by hexa-coordinated Ca–O polyhedra (Fig. 1d). The CaO_6 distorted octahedra share edges forming rings around the FeO_4-tetrahedra. Unsurprisingly, this structure with Fe in three different coordination environments, and in an average oxidation state of 2.888, is thermodynamically quite unstable.[32–34] The oxygen partial pressure is critical in the stability of $Ca_4Fe_9O_{17}$, and therefore the complex synthesis of the material usually results in a mixture of a low crystalline $Ca_4Fe_9O_{17}$ and more stable oxides ($CaFe_2O_4$, FeO, and $Ca_2Fe_2O_5$). Indeed, the crystal structure determination was accomplished using single crystals grown under very specific conditions.[31]

To evaluate the performance of $CaFe_{2+n}O_{4+n}$ compounds as cathode materials for Ca batteries, we have selected the compounds with n = 0, 1/4, 1 and 2 for computational investigations. Density Functional Theory (DFT) calculations are used to anticipate the average intercalation voltage so as to estimate their theoretical energy density, assuming the full Ca extrac-

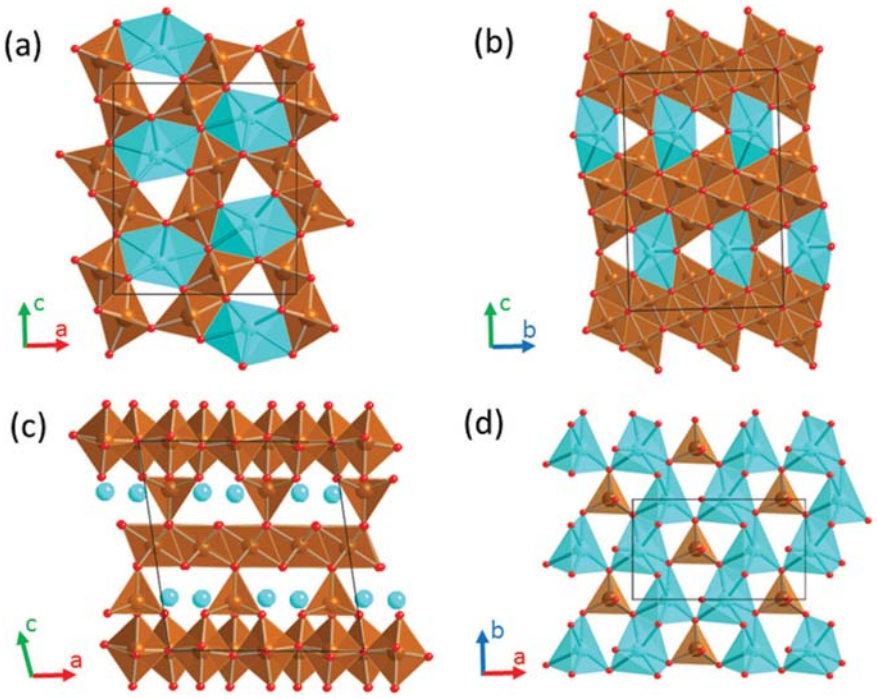

Fig. 1 Crystal structures of $CaFe_{2+n}O_{4+n}$ oxides. (a) n = 0, $CaFe_2O_4$ (b) n = 2, $CaFe_4O_6$ (c) n = 1/4, $CaFe_9O_{17}$ showing the $[CaO_6]$–$[FeO_4]$ plane in (d). Color code: Ca in blue, Fe in brown and O in red.

tion from the structures. Ca diffusion is a key parameter, for which the migration energy barriers provide an approximate indication.[3,35] Following vast literature in the field,[18,21,22,35] in this work the energy barriers for Ca migration are extracted from DFT calculations. The results found for $Ca_4Fe_9O_{17}$ motivated an experimental investigation comprising the synthesis, characterization and electrochemical testing of the material. We present a novel synthesis method to produce highly crystalline powder.

Materials and methods

Computational

The calculations have been carried out using the *ab initio* total-energy and molecular dynamics program VASP (Vienna *ab initio* simulation program) developed at the Universität Wien.[36] Total energy calculations based on Density Functional Theory (DFT) were performed within the General Gradient Approximation (GGA), with the exchange and correlation functional form developed by Perdew, Burke and Ernzerhof (PBE).[37] The interaction of core electrons with the nuclei is described by the Projector Augmented Wave (PAW) method.[38] The energy cut off for the plane wave basis set is fixed at a constant value of 600 eV throughout the calculations. The integration in the Brillouin zone is done on an appropriate set of *k*-points determined using the Monkhors–Pack scheme. A convergence of the total energy close to 10 meV per formula unit is achieved with such parameters. Spin polarization calculations were performed in all cases. All crystal structures were fully relaxed (atomic positions, cell parameters and volume). The final energies of the optimized geometries were recalculated to correct the changes in the basis set of wave functions during relaxation. Average voltages for Ca deinsertion from $CaFe_{2+n}O_{4+n}$ were calculated within the GGA+U method, following the methodology described by Aydinol *et al.*[39]. For consistency with the literature on this topic,[16,21,22,40] the effective U value for the Fe-d orbitals was set to 5 eV (J = 1 eV).

Calcium mobility is investigated using the Nudged Elastic Band method (NEB) as implemented in VASP. To study diffusion, a vacancy is created in the structural model of the stoichiometric oxides and a simple jumping mechanism from an occupied position to the vacant site is considered. Supercells 1 × 2 × 1 ($Ca_8Fe_{18}O_{34}$) and 1 × 4 × 1 ($Ca_4Fe_8O_{16}$) for the n = 1/4 and n = 0 compounds, respectively, were used for the calculations. Constant volume calculations were performed within the GGA approximation for three or five intermediate images initialized by linear interpolation between the two fully relaxed end-points. To calculate the energy at the saddle point, cubic splines were fit through the relaxed images along each hop.

Experimental

Synthesis. Polycrystalline $Ca_4Fe_9O_{17}$ powder samples were prepared by the conventional solid state synthesis method. Stoichiometric mixtures of $Ca_2Fe_2O_5$, Fe_2O_3 and Fe_3O_4 in a molar ratio of 2 : 1 : 1 were thoroughly mixed in an agate mortar, pressed into a pellet and vacuum sealed in a quartz tube. First the samples were thermally treated at 1000° C for 24 h and quenched in water. Then, the purest sample was obtained after four consecutive regrinding and annealing processes of 24 h each at 1150 °C in evacuated quartz tubes. $Ca_2Fe_2O_5$ was previously synthesized following the Pechini method. $Ca(NO_3)_2{\cdot}4H_2O$ (Aldrich 99%), $Fe(NO_3)_3{\cdot}9H_2O$ (Aldrich 99.95%), $C_6H_8O_7$ (citric acid, Aldrich 99.5%) and $C_2H_6O_2$ (ethylene glycol) were subsequently dissolved in water in a molar ratio of $Ca : Fe : C_6H_8O_7 : C_2H_6O_2$ = 1 : 1 : 3 : 1. The solution was kept under continuous stirring at 80 °C until complete evaporation. The obtained citrate complexes were decomposed in air at 500 °C for 8 h. The decomposition process was carried out at a rate of 100 °C h^{-1}. Finally, polycrystalline $Ca_2Fe_2O_5$ was obtained by calcination of the amorphous carbonates at 1000° C for 24 h.

Structural, morphological and compositional characterization. X-Ray powder diffraction patterns were acquired on a Bruker D8 Advance A25 diffractometer in a Debye Scherrer configuration equipped with an Mo $K_{\alpha1}$ radiation source. High resolution synchrotron X-ray diffraction (SXRD) patterns were collected in the MSPD beamline (ALBA synchrotron Light Source, Cerdanyola del Vallès, Spain)[41] using a Mythen detector and λ = 0.8260 Å. In both cases, 0.5 mm diameter borosilicate glass capillaries were used as sample holders and rotated during data collection.

Scanning Electron Microscopy (SEM) and Energy Dispersive X-ray Spectroscopy (EDS) analyses were performed by using a FEI Quanta 200 FEG microscope equipped with an EDAX detector (resolution: 132 eV). Selected Area Electron Diffraction (SAED) studies were performed using a JEOL 1210 transmission electron microscope operating at 120 kV and equipped with a Gathan sample holder. The specimens for electron microscopy were prepared by dispersing the powders in dimethyl carbonate and depositing a droplet of this suspension on a carbon coated film supported on a copper grid.

Electrochemical tests. Electrode tapes were prepared by dispersing a powder mixture of the active material (80 wt%), Super P carbon (10 wt%) and a polyvinylidene difluoride (PVdF, Kynar) binder (10 wt%) in *N*-methyl pyrrolidinone solvent (NMP, Sigma-Aldrich). The obtained dispersion was ball milled for 1 hour at 500 Hz with a RETSCH PM100 instrument before being doctor-blade cast on Al foil (Goodfellow, 99%). Once cast, the tapes were dried under vacuum and cut into discs of 11 mm diameter, with an average active material load of about 2 mg. The electrodes were pressed at 5 Tons before being used.

The electrochemical tests were run in two and three electrode Swagelok cells assembled in an Ar-filled dry box, employing Al and stainless steel current collectors for the working and reference (RE)/counter (CE) electrodes, respectively, and a Whatman separator soaked in 0.6 ml of electrolyte solution. Mechanically polished Ca metal discs (obtained by pressing Ca pieces under an inert atmosphere) or Li metal were used as the counter/reference or counter electrodes, respectively.

Lithium hexafluorophosphate solutions in ethylene carbonate (EC) and dimethyl carbonate (DMC) (LP30, 1.0 M LiPF6 in EC/DMC = 50/50 (v/v), Solvionic) and the lithium bis(oxalato) borate salt (LiBoB, Chemetal, Battery grade) in a 1 : 1 v/v mixture of ethylene carbonate (EC) and propylene carbonate (PC) solvents (Solvionic, 99.9%) were used as electrolytes for the electrochemical tests in Li cells. The electrolyte used in Ca cells was a dry (<40 ppm H_2O, Karl-Fischer titration) 0.45 M calcium tetrafluoroborate hydrate (Alfa Aesar) solution in EC/PC = 50/50 (v/v).

The electrochemical tests were performed on a Bio-Logic VMP3 potentiostat. Electrochemical deintercalation/intercalation tests were carried out in galvanostatic mode (*i.e.* Galvanostatic Cycling with Potential Limitation–GCPL). In order to avoid kinetic limitations the rate was set to C/100. A stabilization time of 5 hours at the OCV was applied before each measurement was carried out at 100 °C. Once tested, the cells were disassembled in an Ar-filled dry box and the electrodes were washed with dimethyl carbonate solvent (DMC, Sigma-Aldrich, ≥99%) and further collected in borosilicate glass capillaries of 0.5 mm diameter for *ex situ* XRD measurements.

Chemical oxidation tests. Chemical oxidation tests were performed by dispersing the active material in an NO_2BF_4 solution in acetonitrile (ACN) in a molar ratio of 1 : 8. The dispersion was kept under reflux at 80 °C for 6 hours. Uninterrupted Ar bubbling served to maintain the reaction atmosphere inert and to eliminate the NO_2 gas formed as the byproduct. Once the reactions were completed, the samples were washed with dry ACN, vacuum filtered, dried and collected for XRD analysis.

Results and discussion

DFT evaluation of basic electrode characteristics

The GGA+U method correctly reproduces the cell lattice parameters of $CaFe_{2+n}O_{4+n}$ compounds (see Table S1†). The deinsertion of Ca can be expressed by the reaction:

$$CaFe_{2+n}O_{4+n} \rightarrow Fe_{2+n}O_{4+n} + Ca \quad (1)$$

The higher the n term, the lower the theoretical specific capacity is. These values are listed in Table 1, together with the average voltage predicted for n = 0, 1/4, 1 and 2. As n increases the Fe ions are in a lower oxidation state, and accordingly Ca deinsertion is predicted at lower voltages. Note that the average voltage depends primarily on the redox couple, but it is also influenced by the crystal structure.[39] For instance, the voltages predicted for the Fe^{3+}/Fe^{4+} couple are 4.16 V in brownmillerite-$Ca_2Fe_2O_5$ (ref. 23) and 3.87 V in $CaFe_2O_4$. Taking the calculated voltage and the theoretical specific capacities into account, theoretical energy densities exceeding 600 mA h g^{-1} (the state of the art in the Li-ion technology) could be viable for n = 0, 1/4 and 1.

One of the major concerns in cathode material design for the Ca battery technology is the mobility of Ca^{2+} ions in inorganic structures. Although other factors can certainly limit the success of Ca battery cathodes, a good cation diffusion, that is to say a low migration energy barrier, is a necessary prerequisite. It has been estimated that for a reasonable cell power rate (discharging time 2 hours) the energy barriers for cation diffusion should be below 0.525 eV in micrometer particles and 0.65 eV in nanosized-particles.[3] The calculated energy barrier for $CaFe_2O_4$ (1.2 eV, see Fig. 1 in the ESI†) greatly surpasses this tolerable value, and therefore, the ferrites $CaFe_{2+n}O_{4+n}$ built up from $CaFe_2O_4$ blocks will also suffer from poor Ca mobility. However, the n = 1/4 term might be a viable option. Fig. 2 shows the pathway for Ca diffusion in $Ca_4Fe_9O_{17}$ and the calculated energy barrier. In the two-dimensional diffusion pathway in the $[CaO_6]$–$[FeO_4]$ plane (shown in Fig. 1d) the diffusing Ca ions exit from their polyhedra across a triangular face to occupy the intermediate tetrahedral site (see Fig. 2a). The associated energy barrier for in-plane Ca diffusion is 0.72 eV (Fig. 2b), the lower energy ever reported for an existing transition metal oxide. The tetrahedral site represents a local energy minimum in the energy landscape. The similarity in Ca–Fe distances at this intermediate site and at the equilibrium sites (3.22 Å and 3.29 Å, respectively) suggests that the diffusing Ca ion does not experience large electrostatic repulsions with the neighbouring $Fe^{+2.88}$ cations. Compared to other oxides, the lower repulsive forces between the diffusing Ca^{2+} and other cations in the structure reduce the migration energy.[4] Although the barrier is relatively low for Ca diffusion, it is still too high for fast rate performance. Note that the barriers for Li diffusion in layered, olivine and spinel cathodes are below 0.3 eV.[3,35,42,43]

Interestingly, a related compound, $K_2Fe_4O_7$, has been recently reported and suggested as a K-superionic conductor.[44] The framework of $K_2Fe_4O_7$ consists of planes of edge-sharing FeO_6 octahedra sandwiched between planes of FeO_4 tetrahedra and octahedrally coordinated K ions. The K octahedra form rings around FeO_4 tetrahedra, thus providing a 2D conduction plane similar to that in $Ca_4Fe_9O_{17}$ (Fig. 1d and 2a). When tested in the $K/K_2Fe_4O_7$/Pt cell no significant current due to

Table 1 Electrode characteristics of $CaFe_{2+n}O_{4+n}$ assuming full Ca deinsertion (reaction 1)

$CaFe_{2+n}O_{4+n}$ composition	n	Fe redox couple	Theoretical specific capacity (mA h g^{-1})	Calculated average voltage (V)	Theoretical specific energy (mW h g^{-1})
$CaFe_2O_4$	0	+3/+4	249	3.87	964
$Ca_4Fe_9O_{17}$	1/4	+2.88/3.77	230	4.16	957
$CaFe_3O_5$	1	+2.66/+3.33	186	3.66	680
$CaFe_4O_6$	2	+2.5/+3	149	2.37	353

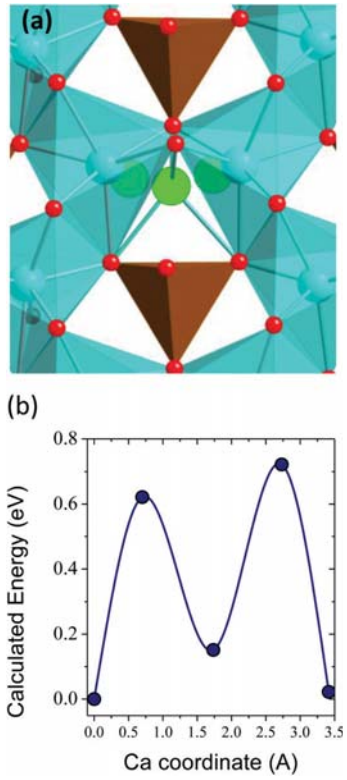

Fig. 2 (a) View of the Ca diffusion pathway in $Ca_4Fe_9O_{17}$, showing the tetrahedral site at the transition state. (b) Calculated energy barrier. Color code: Ca sites in blue, diffusing Ca in green, Fe in brown, O in red.

the solid electrolyte decomposition was observed up to 5.0 V. Despite the presence of Fe^{3+}, the authors found that the material is also stable upon reduction down to 0 V.

Synthesis

$Ca_4Fe_9O_{17}$ was first reported by B. Malaman *et al.* in the 80's[31] and its crystal structure was elucidated from a single crystal. Despite a few articles mentioning its existence (a summary of those is provided in Table S2†), no reliable bulk powder synthesis method is available in the literature. In all cases, this phase is reported to form, mixed with $CaFe_2O_4$ and $Ca_2Fe_2O_5$ phases that are stable in the same region of the FeO–Fe_3O_4–CaO phase diagram.

In view of the discrepancies present in the literature, in this work different synthesis methods were attempted at temperatures ranging from 800 to 1200 °C, including conventional solid state synthesis using $CaCO_3$ or CaO as Ca sources and Fe_2O_3, Fe_3O_4 or FeO as iron precursors. The Pechini method was also attempted.[45] Most reaction products consisted of a mixture of Fe_2O_3 and $CaFe_2O_4$ in all cases, whatever the reaction times (from 6 to 64 hours), except for the samples treated at 1200 °C for which melting and thermal reduction of iron oxide was observed. Further synthesis attempts were carried out in a tube sealed under vacuum, and the phase $Ca_4Fe_9O_{17}$ was observed in small amounts after synthesis at 1000° C for 48 h followed by quenching. Optimization of this reaction protocol, modifying precursors, temperature and time, enabled the synthesis of pure $Ca_4Fe_9O_{17}$ using a stoichiometric mixture of $Ca_2Fe_2O_5$, Fe_2O_3 and Fe_3O_4 as precursors, targeting to control the iron oxidation state by tuning the amount of oxygen available in the precursors. However, a pure phase was achieved only after several treatments at 1150 °C for 24 h each in a sealed quartz tube followed by quenching in water (a summary of synthesis results is provided in Fig. S2†).

Structure and morphology

Fig. 3 shows a full pattern matching of X-ray diffraction patterns of the as prepared $Ca_4Fe_9O_{17}$ sample in the monoclinic system, space group *C*2 using the Fullprof program. The cell parameters obtained by the Le Bail method were a = 10.44177 (24) Å, b = 6.02422(21) Å, c = 11.36840(36) Å and β = 98.7853 (16) which are in good agreement with those previously reported from the single crystal structural determination.[31]

Attempts to perform a Rietveld refinement of this X-ray diffraction pattern using the structural model reported by B. Malaman *et al.*[31] resulted in unsatisfactory fitting of the model to the experimental pattern, despite all efforts to modify cell parameters, occupation factors, *etc*. The differences in the observed and calculated integrated intensities of several reflections suggest that the prepared material might present some structural differences with respect to the single crystal studied by B. Malaman (see Fig. S3†).

In order to further characterize the structure of the as prepared $Ca_4Fe_9O_{17}$ phase, SAED was performed and micrometric particles were observed, as shown in Fig. 4. The cell parameters obtained by electron diffraction were a = 10.4 Å, b = 6.02 Å and c = 11.4 Å. The ED image along the c zone axis presents the characteristic scattered lines indicative of the presence of stacking defects along the c axis. The occurrence of stacking faults could explain the differences between observed

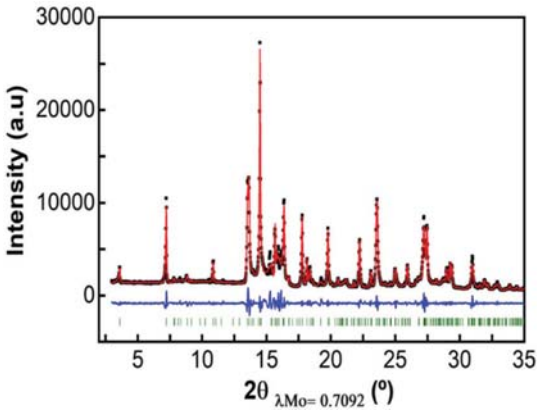

Fig. 3 Pattern matching of $Ca_4Fe_9O_{17}$ in the monoclinic system, space group *C*2.

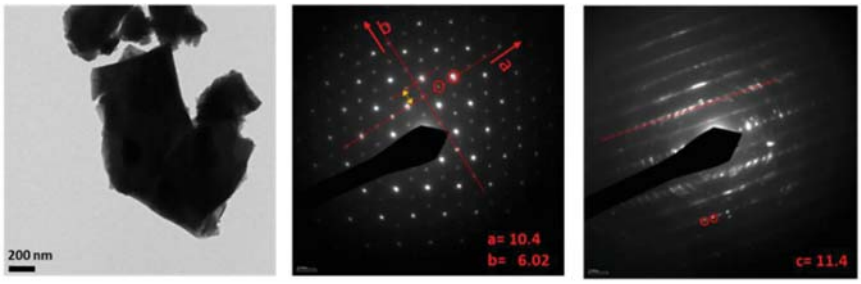

Fig. 4 SAED images of the $Ca_4Fe_9O_{17}$ sample.

and calculated intensities in Rietveld refinement. The stacking faults are not expected to perturb the in-plane Ca conductivity, unless they imply inter-layer cation mixing or phase transformations.[42,46]

Chemical and electrochemical tests on $Ca_4Fe_9O_{17}$ and $Ca_2Fe_2O_5$

Attempts to extract Ca^{2+} from $Ca_4Fe_9O_{17}$ were carried out both by chemical oxidation with NO_2BF_4 (ref. 47) and by electrochemical methods at room temperature and 100 °C. Tape electrodes were prepared and cycled according to the electrochemical protocol described in the experimental section. The characteristic potential *vs.* capacity profiles of these electrodes upon galvanostatic cycling at RT and 100 °C in Li or Ca cells and in several Li or Ca electrolytes at C/100 are shown in Fig. 5 (a and b) for $Ca_4Fe_9O_{17}$ and in Fig. S4† (left panel) for $Ca_2Fe_2O_5$. The utilization of a low rate (C/100) is in line with the calculated energy barrier of 0.72 eV, which as commented before is too high for fast-rate performance. Indeed, Ca intercalation in TiS_2 (calculated energy barrier 0.75 eV) requires similarly slow rates.[12] Upon oxidation, a short plateau-like region centered between 2.9 V and 4.8 V *vs.* M^{n+}/M (M = Li or Ca) is observed, with the potential at which the plateau appears depending on the nature of the electrolyte, the temperature and the counter electrode used. The *ex situ* X-ray powder diffraction patterns of the $Ca_4Fe_9O_{17}$ samples collected

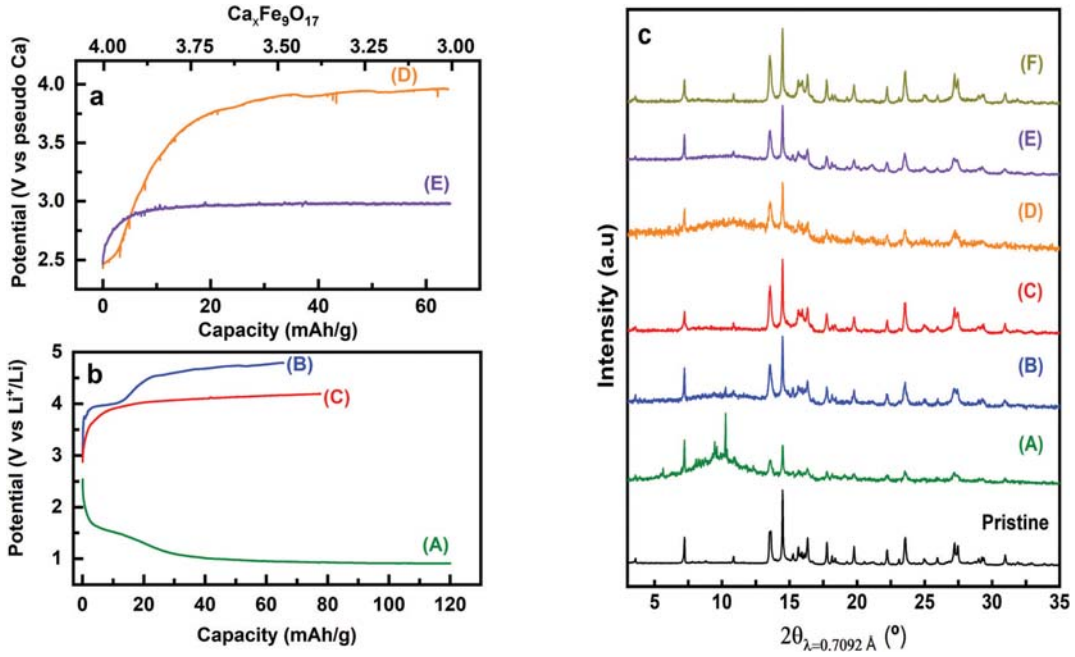

Fig. 5 Characteristic voltage profiles *versus* specific capacity (bottom) and *versus* moles of virtually de-inserted Ca^{2+} (Δx, estimated that calcium deintercalation is the only reaction taking place) (top) for $Ca_4Fe_9O_{17}$ in Ca cells (a), with 0.45 M $Ca(BF_4)_2$, EC/PC (1 : 1 vol) electrolyte at RT (D) and 100 °C (E) and in Li cells (b), with LP30 electrolyte at RT (A and B), 1 m LiBOB, EC/PC (1 : 1 vol) electrolyte at 100 °C (C). Corresponding *ex situ* XRD patterns in (c). XRD patterns of the pristine and chemically oxidized samples (F) are also displayed in (c).

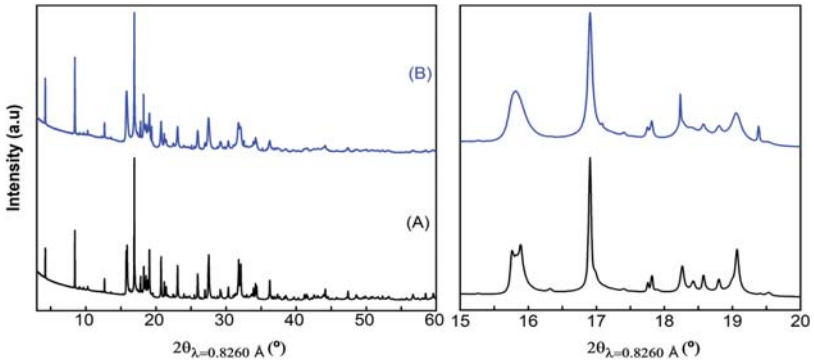

Fig. 6 Synchrotron X-ray powder diffraction patterns of pristine (A) and electrochemically oxidized (in the LP30 electrolyte) (B) $Ca_4Fe_9O_{17}$ samples.

after the electrochemical and chemical oxidation tests are shown in Fig. 5(c) and Fig. S4† (right panel), respectively. Compared with the pristine phase, neither peak shifts nor formation of extra phases is observed in any spectra except for the one corresponding to electrochemical measurement performed on $Ca_4Fe_9O_{17}$ in the lithium cell with the LP30 electrolyte. Thus, except for that case, the electrochemical capacity observed is ascribed to side reactions most likely involving electrolyte decomposition, which are enhanced at high temperature. In contrast, the synchrotron X-ray diffraction patterns of the pristine sample and the sample electrochemically oxidized in a lithium/LP30 cell exhibit minor differences (see Fig. 6). Indeed, the pattern full width at half maximum for peaks situated at Q values of 2.09 $Å^{-1}$, 2.24 $Å^{-1}$ and 2.53 $Å^{-1}$ is different.

While the origin of these subtle changes has been unclear to date, one may speculate that they could be related to deinsertion of a small amount of calcium from $Ca_4Fe_9O_{17}$ at the 4.0 V plateau (capacity 12 mA h g^{-1}, curve B in Fig. 5b) concomitant with the oxidation of iron. In fact, hypothetical oxidation to yield $Ca_{3.5}Fe_9O_{17}$ could be related to the Fe^{2+}/Fe^{3+} redox pair, with an expected voltage considerably smaller than 4.16 V, and thus within the voltage window of the LP30 electrolyte stability. Further oxidation should involve the Fe^{3+}/Fe^{4+} couple, with a higher voltage (*ca.* 4.2 V), which may be out of the voltage window of the electrolyte stability, especially if polarization is significant. Yet, in light of the low value of the capacity and the disorder present in the crystals, this phenomenon has not been further studied.

Regardless of the partial oxidation of Fe detected in Li cells (likely the Fe^{2+}/Fe^{3+} couple), further oxidation has not been achieved either electrochemically or chemically. Noteworthily, the calculated average voltage for the full Ca deinsertion, the $Fe^{+2.88}/Fe^{+3.77}$ couple (4.16 V, see Table 1), is probably beyond the anodic stability of available Ca electrolytes[5] and in the limit of Li electrolytes if cell polarization is significant. In this regard, we attempted the electrochemical and chemical oxidation of $Ca_2Fe_2O_5$, for which DFT investigations found an average voltage of 4.16 V for the Fe^{3+}/Fe^{4+} couple, although with a sluggish kinetics (calculated energy migration barrier 1 eV).[23] The combination of electrochemical and XRD characterization (see Fig. 3 in the ESI†) reflects the inactivity of $Ca_2Fe_2O_5$ in both Ca and Li electrolytes. A plausible explanation is that Ca deintercalation from these materials requires electrolytes operating in the 5 V range, so as to allow the oxidation of Fe to the +4 oxidation state.

To test the electrochemical stability window of $Ca_4Fe_9O_{17}$, Li/LP30/$Ca_4Fe_9O_{17}$ cells were discharged down to 1 V. Upon reduction, the potential *vs.* capacity profiles for $Ca_4Fe_9O_{17}$ displayed in Fig. 5b(A) present a long plateau-like region centered at 1 V *vs.* Li^+/Li and additional diffraction peaks are observed in the 2θ = 10° region of the corresponding *ex situ* X-ray powder diffraction pattern shown in Fig. 5c(A). This large capacity can be regarded as the combination of two competing processes: the low-voltage decomposition of the electrolyte and the reduction of Fe^{3+} to Fe^{2+} upon Li uptake. Noteworthily, a similar potential *vs.* capacity profile is observed for the reduction of Fe_2O_3 electrodes in Li cells;[48] the electrochemical conversion reactions of Fe^{3+} compounds with lithium are known to evolve until the eventual formation of small Li_2O and metallic iron domains.[48,49] In the present case, the identification of the phases formed during the reduction remains undetermined due to the complex nature of the starting material. However, these results highlight the instability of $Ca_4Fe_9O_{17}$ upon reduction, contrary to the reported stability of the related K-phase down to 0 V *vs.* K^+/K.[44]

Conclusions

Sustainability combined with high energy density prospects makes Fe-based oxides appealing cathodes for calcium rechargeable batteries. The present DFT investigation reveals that among the $CaFe_{2+n}O_{4+n}$ materials, $Ca_4Fe_9O_{17}$ combines the most appealing characteristics. The favorable local topology for Ca diffusion in $Ca_4Fe_9O_{17}$ bestows the lowest energy barrier so far reported for an existing oxide (0.72 eV). However, the predicted average deintercalation voltage (4.16 V for full Ca

deinsertion) is beyond the stability range of current Ca electrolytes and, accordingly, electrochemical attempts to deintercalate Ca ions from $Ca_4Fe_9O_{17}$ in Ca cells were unsuccessful. However, a small charge capacity probably associated with the oxidation of Fe^{2+} to Fe^{3+} is observed in Li cells using the LP30 electrolyte. The suitability of $Ca_4Fe_9O_{17}$ as a Ca cathode is pending further studies utilizing electrolytes with higher anodic stability. Electrochemical and any other property investigations will no doubt benefit from the novel synthesis route reported here which, contrary to previous strategies, allows synthesizing pure and crystalline $Ca_4Fe_9O_{17}$ powders.

Conflicts of interest

There are no conflicts to declare.

Acknowledgements

This research was funded by the European Union's Horizon 2020 research and innovation programme H2020 FETOPEN-1-2016-2017 (CARBAT, grant agreement no. 766617). The authors are grateful for access to the computational facilities from Universidad de Oviedo (MALTA-Consolider cluster), to ALBA synchrotron for the provision of beam time and to Dr F. Fauth for his help during data collection and also acknowledge Dr. J. Oró-Solé for assistance with electron diffraction and Dr. Clemens Ritter for helpful discussions. ICMAB authors are also grateful to the Spanish Ministry for Economy, Industry and Competitiveness Severo Ochoa Programme for Centres of Excellence in R&D (SEV-2015-0496).

Notes and references

1 A. L. Lipson, B. Pan, S. H. Lapidus, C. Liao, J. Y. Vaughey and B. J. Ingram, *Chem. Mater.*, 2015, **27**, 8442–8447.
2 J. Muldoon, C. B. Bucur and T. Gregory, *Chem. Rev.*, 2014, **114**, 11683–11720.
3 P. Canepa, G. S. Gautam, D. C. Hannah, R. Malik, M. Liu, K. G. Gallagher, K. A. Persson and G. Ceder, *Chem. Rev.*, 2017, **117**, 4287–4341.
4 M. E. Arroyo-de Dompablo, A. Ponrouch, P. Johansson and M. R. Palacin, *Chem. Rev.*, 2019, DOI: 10.1021/acs.chemrev.9b00339.
5 A. Ponrouch, C. Frontera, F. Barde and M. R. Palacin, *Nat. Mater.*, 2015, **15**, 169–172.
6 D. Wang, X. Gao, Y. Chen, L. Jin, C. Kuss and P. G. Bruce, *Nat. Mater.*, 2018, **17**, 16–20.
7 A. Shyamsunder, L. E. Blanc, A. Assoud and L. F. Nazar, *ACS Energy Lett.*, 2019, **49**, 2271–2276.
8 Z. Li, O. Fuhr, M. Fichtner and Z. Zhao-Karger, *Energy Environ. Sci.*, 2019, **12**, 3496–3501.
9 A. Ponrouch and M. R. Palacin, *Curr. Opin. Electrochem.*, 2018, **9**, 1–7.
10 R. J. Gummow, G. Vamvounis, M. B. Kannan and Y. He, *Adv. Mater.*, 2018, **30**, e1801702.
11 G. G. Amatucci, F. Badway, A. Singhal, B. Beaudoin, G. Skandan, T. Bowmer, I. Plitza, N. Pereira, T. Chapman and R. Jaworski, *J. Electrochem. Soc.*, 2001, **148**, A940–A950.
12 D. S. Tchitchekova, A. Ponrouch, R. Verrelli, T. Broux, C. Frontera, A. Sorrentino, F. Barde, N. Biskup, M. E. Arroyo-de Dompablo and M. R. Palacin, *Chem. Mater.*, 2018, **30**, 847–856.
13 M. Cabello, F. Nacimiento, R. Alcantara, P. Lavela, C. Pérez-Vicente and J. L. Tirado, *Chem. Mater.*, 2018, **30**, 5853–5861.
14 M. Cabello, F. Nacimiento, J. R. González, G. Ortiz, R. Alcántara, P. Lavela, C. Pérez-Vicente and J. L. Tirado, *Electrochem. Commun.*, 2016, **67**, 59–64.
15 M. E. Arroyo-de Dompablo, C. Krich, J. Nava-Avendano, N. Biskup, M. R. Palacin and F. Barde, *Chem. Mater.*, 2016, **28**, 6886–6893.
16 M. E. Arroyo-de Dompablo, C. Krich, J. Nava-Avendaño, M. R. Palacín and F. Bardé, *Phys. Chem. Chem. Phys.*, 2016, **18**, 19966–19972.
17 R. Verrelli, A. P. Black, C. Pattanathummasid, D. S. Tchitchekova, A. Ponrouch, J. Oro-Sole, C. Frontera, F. Barde, P. Rozier and M. R. Palacin, *J. Power Sources*, 2018, **407**, 162–172.
18 G. S. Gautam, P. Canepa, R. Malik, M. Liu, K. Perssonb and G. Ceder, *Chem. Commun.*, 2015, **51**, 13619–13622.
19 D. S. Tchitchekova, C. Frontera, A. Ponrouch, C. Krich, F. Barde and M. R. Palacin, *Dalton Trans.*, 2018, **47**, 11298–11302.
20 A. Torres, F. Bardé and M. E. Arroyo-de Dompablo, *Solid State Ionics*, 2019, **340**, 115004.
21 Z. Rong, R. Malik, P. Canepa, G. S. Gautam, M. Liu, A. Jain, K. Persson and G. Ceder, *Chem. Mater.*, 2015, **27**, 6016–6021.
22 M. Liu, Z. Rong, R. Malik, P. Canepa, A. Jain, G. Ceder and K. A. Persson, *Energy Environ. Sci.*, 2015, **8**, 964–974.
23 A. Torres, F. J. Luque, J. Tortajada and M. E. Arroyo-de Dompablo, *Energy Storage Mater.*, 2019, **21**, 354–360.
24 J. Hyoung, J. W. Heo and S.-T. Hong, *J. Power Sources*, 2018, **390**, 127–133.
25 S. Suzuki, T. Kato, H. Kawabata and M. Miyayama, *J. New Mater. Electrochem. Syst.*, 2016, **19**, 51–55.
26 A. Torres, F. J. Luque, J. Tortajada and M. E. Arroyo-de Dompablo, *Sci. Rep.*, 2019, **9**, 9644.
27 E. F. Bertaut, P. Blum and G. Magnano, *Acta Crystallogr.*, 1957, **10**, 238–238.
28 B. F. Decker and J. S. Kasper, *Acta Crystallogr.*, 1957, **10**, 332–337.
29 B. Malaman, H. Alebouyeh, F. Jeannot, A. Courtois, R. Gerardin and O. Evrard, *Mater. Res. Bull.*, 1981, **16**, 1139–1148.
30 O. Evrard, B. Malaman, F. Jeannot, A. Courtois, H. Alebouyeh and R. Gerardin, *J. Solid State Chem.*, 1980, **35**, 112–119.

31 B. Malaman, H. Alebouyeh, A. Courtois, R. Gerardin and O. Evrard, *Mater. Res. Bull.*, 1982, **17**, 795–800.
32 M. Aspiala, T. Hidayat, P. Taskinen and E. Jak, *J. Alloys Compd.*, 2016, **658**, 939–945.
33 H.-Y. Li and X.-M. Guo, *Metall. Mater. Trans. B*, 2015, **46**, 278–285.
34 E. Rosen and B. Saitton, *Scand. J. Metall.*, 1995, **24**, 176–179.
35 D. Morgan, A. Van der Ven and G. Ceder, *Electrochem. Solid-State Lett.*, 2004, **7**, A30–A32.
36 G. Kresse and J. Furthmuller, *Phys. Rev. B: Condens. Matter Mater. Phys.*, 1996, **54**, 11169–11186.
37 J. P. Perdew, K. Burke and M. Ernzerhof, *Phys. Rev. Lett.*, 1996, **77**, 3865–3868.
38 P. E. Bloch, *Phys. Rev. B: Condens. Matter Mater. Phys.*, 1994, **50**, 17953.
39 M. K. Aydinol, A. F. Kohan, G. Ceder, K. Cho and J. Joannopoulos, *Phys. Rev. B: Condens. Matter Mater. Phys.*, 1997, **56**, 1354–1365.
40 A. Torres and M. E. Arroyo-de Dompablo, *J. Phys. Chem. C*, 2018, **122**, 9356–9362.
41 F. Fauth, I. Peral, C. Popescu and M. Knapp, *Powder Diffr.*, 2013, **28**, 360–370.
42 C. R. Fell, D. H. Lee, Y. S. Meng, J. M. Gallardo-Amores, E. Moran and M. E. Arroyo-de Dompablo, *Energy Environ. Sci.*, 2012, **5**, 6214–6224.
43 Y. S. Meng and M. E. Arroyo-de Dompablo, *Energy Environ. Sci.*, 2009, **2**, 589–609.
44 H. Yuan, H. Li, T. Zhang, G. Li, T. He, F. Du and S. Feng, *J. Mater. Chem. A*, 2018, **6**, 8413–8418.
45 M. P. Pechini, *US Pat*, 3330697, 1967.
46 B. Mortemard de Boisse, M. Reynaud, J. Ma, J. Kikkawa, S.-i. Nishimura, M. Casas-Cabanas, C. Delmas, M. Okubo and A. Yamada, *Nat. Commun.*, 2019, **10**, 2185.
47 A. R. Wizansky, P. E. Rauch and F. J. Disalvo, *J. Solid State Chem.*, 1989, **81**, 203–207.
48 D. Larcher, D. Bonnin, R. Cortes, I. Rivals, L. Personnaz and J.-M. Tarascon, *J. Electrochem. Soc.*, 2003, **150**, A1643–A1650.
49 J. M. Tarascon, S. Grugeon, S. Laruelle, D. Larcher and P. Poizot, in *Lithium Batteries: Science and Technology*, ed. G. Nazri and G. Pistoia, Kluwer Academic Publishers, 2004.

Electronic Supplementary Material (ESI) for Dalton Transactions.

Supplementary Information

Appraisal of calcium ferrites as cathode for calcium rechargeable batteries: DFT, synthesis, characterization and electrochemistry of $Ca_4Fe_9O_{17}$

A. P. Black,[1,2] A. Torres[3], C. Frontera[1], M.R. Palacín[1,2], and M. E. Arroyo-de Dompablo[3*]

[1]Institut de Ciència de Materials de Barcelona (ICMAB-CSIC) Campus UAB, E-08193 Bellaterra, Catalonia, (Spain)

[2]ALISTORE-ERI European Research Institute

[3]Departamento de Química Inorgánica, Universidad Complutense de Madrid, 28040 Madrid, (Spain)

Table 1. Experimental vs. Calculated (GGA+U, U_{eff} = 5 eV) lattice parameters for $CaFe_{2+n}O_{4+n}$

Composition	Experimental lattice parameters (Å)	Calculate lattice parameters (Å)
$CaFe_2O_4$ [1]	9.230(12), 3.024(4), 10.705(1)	9.342, 3.055, 10.852
$Ca_4Fe_9O_{17}$ [2]	10.441(2) 6.025(2) 11.384(2) ß= 98.8(2)	10.586, 6.101, 11.552 ß = 98.663
$CaFe_3O_5$ [3]	3.021(1), 10.009(1), 12.643(1	3.052, 10.292, 12.728
$CaFe_4O_6$ [4]	3.050(1), 9.986(1), 15.321(2)	3.122, 10.391, 16.396

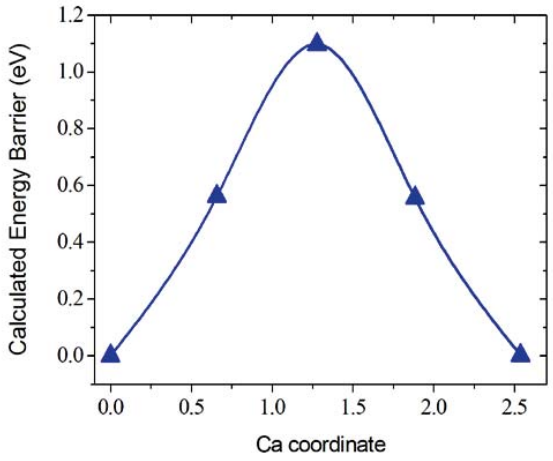

Figure S1. Calculated energy barrier for Ca migration in $CaFe_2O_4$

Table 2. Summary of literature reports on $Ca_4Fe_9O_{17}$ synthesis methods.

Reactants	Conditions	Products	[ref]
$FeO + CaFe_2O_4$	1120°C for 15 days under vacuum	$Ca_4Fe_9O_{17}$ single crystal	[2]
$CaFe_2O_4 + Ca_2Fe_2O_5 + Fe_3O_4$	1000°C for 1 to 10 days, quenched in water	undetermined	[5]
$Fe(NO_3)_3 \cdot 9H_2O$ + $Ca(NO_3)_2 \cdot 4H_2O$ ratio (1:0,5)	670-830°C for 6h in Air	$Ca_2Fe_2O_5 + Ca_4Fe_{14}O_{25} + CaFe_2O_4 + Ca_4Fe_9O_{17}$	[6]
$CaFe_2O_4 + Ca_2Fe_2O_5 + FeO$	1200°C for 8h in Air	$Ca_2Fe_2O_5 + CaFe_2O_4 + Ca_4Fe_9O_{17}$	[7]
$Fe_3O_4 + Fe_2O_3 + CaO$	2x1300°C for 1h + 1100°C for 2 days + 1000°C for 7 days in Ar and quenched in water	$Ca_2Fe_2O_5 + CaFe_2O_4 + Ca_4Fe_9O_{17}$	[8]

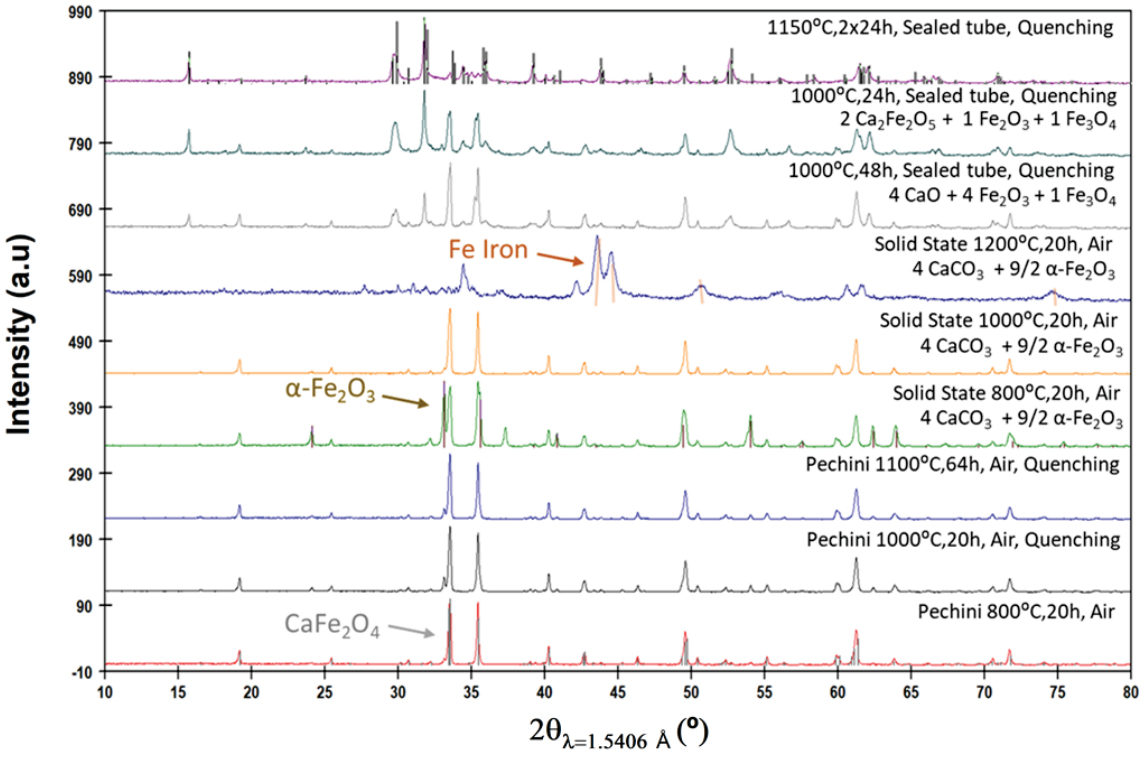

Figure S2. Selected x-ray diffraction patterns of $Ca_4Fe_9O_{17}$ synthesis attempts during synthesis route optimization.

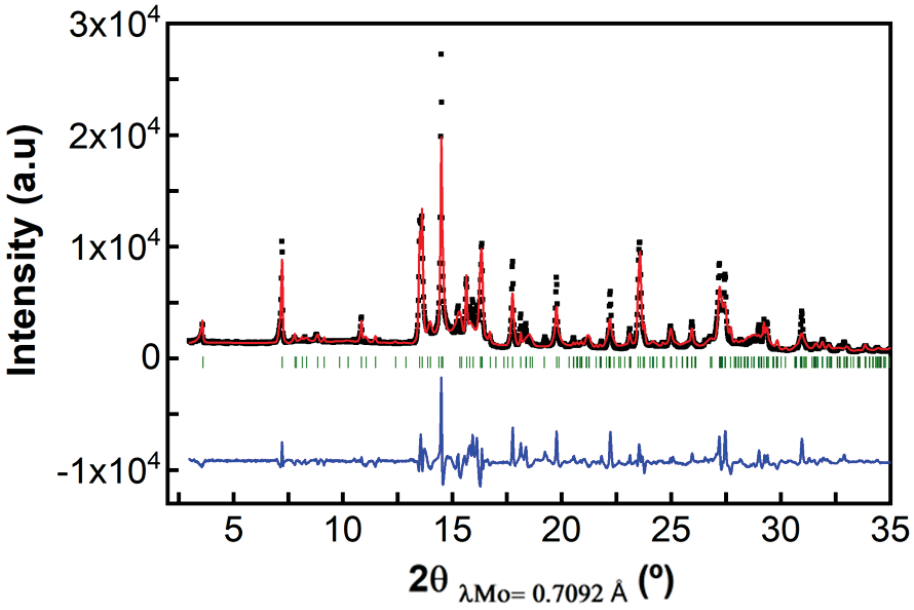

Figure S3. Rietveld refinement of the $Ca_4Fe_9O_{17}$ x-ray diffraction pattern using the structural model reported in [2].

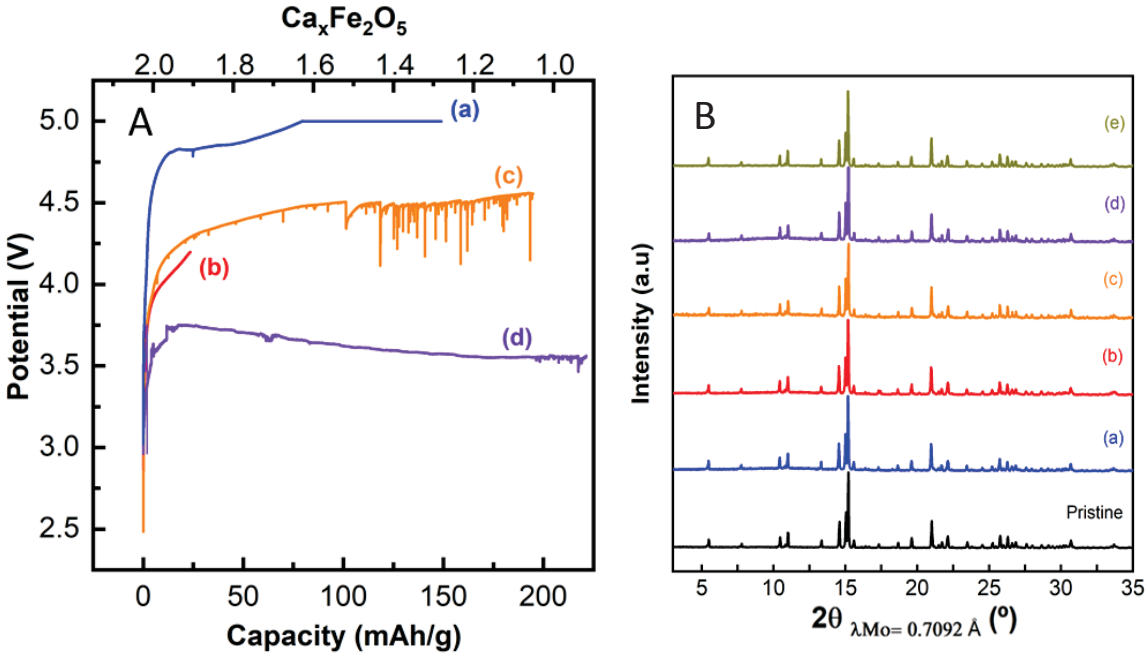

Figure S4. **(A)** Characteristic voltage profiles versus specific capacity (bottom) and versus moles of virtually de-inserted Ca^{2+} (Δx, estimated that calcium deintercalation is the only reaction taking place) (top) for $Ca_2Fe_2O_5$ in Li cells, with LP30 electrolyte at RT **(a)**, 1 m LiBOB, EC/PC (1:1 vol) electrolyte at 100°C **(b)** and in Ca cells, with 0.45 M $Ca(BF_4)_2$, EC/PC (1:1 vol) electrolyte at RT **(c)** and 100°C **(d)** and corresponding ex-situ XRD patterns in **(B)**. XRD patterns of the pristine and chemically oxidized samples are also displayed in **(B).**

References

[1] B.F. Decker, J.S. Kasper, The structure of calcium ferrite, Acta Cryst., 10 (1957) 332-337.

[2] B. Malaman, H. Alebouyeh, A. Courtois, R. Gerardin, O. Evrard, The crystalline-structure of $Ca_4Fe_9O_{17}$ - hexagonal layers of FeO_6 octahedrons and FeO_5 bipyramids linked by FeO_4 tetrahedrons, Mat. Res. Bull., 17 (1982) 795-800.

[3] B. Malaman, H. Alebouyeh, F. Jeannot, A. Courtois, R. Gerardin, O. Evrard, Preparation and characterization of calcium ferrites of the form $CaFe_{2+n}O_{4+n}$ with fractional values of n (3/2,5/2) and their incidence in the Fe-Ca-O diagram at 1120-degrees-c, Mat. Res.Bull., 16 (1981) 1139-1148.

[4] O. Evrard, B. Malaman, F. Jeannot, A. Courtois, H. Alebouyeh, R. Gerardin, The synthesis of a new calcium ferrite ($CaFe_4O_6$) and determination of calcium-ferrite crystalline-structures ($CaFe_{2+n}O_{4+n}$) - a new example of the intergrowth process, J. Solid State Chem., 35 (1980) 112-119.

[5] S. Holmquist, Two new complex calcium ferrite phases, Nature, 185 (1960) 604.

[6] H. Saleh, Synthesis and formation mechanisms of calcium ferrite compounds, J. Mater. Sci. Techol., 20 (2004) 530-534.

[7] H-Y. Li, X-M. Guo, Determination of Gibbs free energy of formation from elements for $Ca_4Fe_9O_{17}$ by Solid-State Galvanic Cell, Metall. Mat. Trans. B, 46.1 (2015), 278–85

[8] A. Markus, H. Taufiq, T. Pekka, J, Evgueni, Determination of thermodynamic properties of $Ca_4Fe_9O_{17}$ by solid state EMF method, J. Alloys Comp., 658(2016), 939-945.

CAPÍTULO 7

CONCLUSIONES

El desarrollo de baterías secundarias basadas en reacciones de intercalación de calcio requiere encontrar materiales útiles como electrodo positivo, y que deben cumplir una serie de requisitos de cara a que la batería proporcione buenas prestaciones. Éste ha sido el objetivo final de esta Tesis. Así mismo, teniendo en cuenta el escaso conocimiento de la química de intercalación del Ca, se ha intentado ampliar el conocimiento sobre este tipo de reacciones. Para alcanzar ambos objetivos (aplicado y fundamental), se han realizado cálculos DFT en un conjunto de materiales. A partir del estudio de los materiales presentados en los capítulos 3-6 se pueden establecer las siguientes conclusiones:

1) La metodología de cálculo DFT permite predecir parámetros de interés sobre el comportamiento de un material como electrodo positivo en baterías de calcio. En esta Tesis sólo se han abordado los aspectos más básicos (variación de volumen asociada a la reacción de inserción, voltajes de intercalación y conductividad iónica de los materiales). Estas características básicas son suficientes, en primera instancia, para descartar materiales y centrarse en el estudio experimental de los más prometedores. Un estudio computacional más avanzado sobre los materiales de electrodo puede hacerse utilizando otras metodologías, como la dinámica molecular ab initio (AIMD) para el cálculo de coeficientes de difusión, o la combinación de DFT con mecánica estadística para construir las curvas composición-voltaje.

2) En todos los materiales estudiados, la forma sintetizable es la “calciada”, es decir, todos los compuestos contienen calcio en su estructura, por lo que la reacción estudiada es la desintercalación de calcio. Sin entrar en consideraciones de su aplicabilidad, los resultados sugieren que no en todos los materiales es factible la desinserción de Ca. Por ejemplo, en los minerales estudiados las barreras de migración (> 2 eV) indican que el Ca es “inmóvil”, no siendo posible su desinserción, lo que está de acuerdo con su estabilidad en entornos naturales.

3) En los materiales estudiados la desinserción de Ca^{2+} es concomitante con la oxidación del metal de transición, por lo que es previsible una disminución del volumen de la celda unidad. Los resultados DFT corroboran esta hipótesis. Dado el tamaño del Ca^{2+}, las variaciones de volumen son en algunos casos considerables (15 % en el piroxeno $CaMn(SiO_3)_2$). Sin embargo, en aquellos materiales en los que la desinserción el Ca^{+2} es parcial, la variación del volumen puede ser moderada, por ejemplo, 3% en el caso de $Ca_3Co_2O_6$ (experimentalmente confirmado). Para este material, a pesar de la leve

modificación de los parámetros y el volumen de la celda unidad, se predicen cambios significativos a nivel local que afectan al entorno de coordinación del Co y del Ca. Estos cambios pueden originar una trasformación irreversible del material, lo que no es infrecuente en las reacciones de intercalación. En última instancia, las transformaciones estructurales comprometen la capacidad específica reversible que pueda desarrollar el material.

4) Para los óxidos estudiados de los que previsiblemente el Ca^{2+} puede desinsertarse, la reacción transcurriría a voltajes medios adecuados para su aplicación en baterías de alta densidad energética, esto es, en el rango de los 3-4 V vs Ca^{2+}/Ca. Los voltajes de intercalación de los pares redox estudiados (Co^{4+}/Co^{3+}, Fe^{4+}/Fe^{3+}) son similares a los encontrados en la tecnología de ion-Li.

5) De acuerdo con estudios previos a esta Tesis, la baja movilidad del Ca^{2+} en las estructuras inorgánicas es el mayor obstáculo para el desarrollo de materiales de electrodo basados en reacciones de intercalación. La figura 7.1 recoge los valores de las energías de activación calculadas mediante DFT para los materiales estudiados en esta Tesis y en otros trabajos computacionales. Puede verse cómo algunos de los óxidos estudiados ($Ca_4Fe_9O_{17}$, $Ca_3Co_2O_6$, y $Ca_3Co_4O_9$) presentan las barreras más bajas reportadas hasta la fecha. No obstante, las barreras energéticas de los óxidos son superiores a las encontradas en calcogenuros, si bien, como contrapartida los óxidos ofrecen mayor densidad energética. La mayor participación covalente en el enlace en los calcogenuros parece justificar la mejor difusión del Ca^{2+} en sus estructuras cristalinas. En este sentido, y de cara a completar el mapa de estructura-composición-propiedades, sería esencial estudiar el comportamiento de oxisulfuros y nitruros.

6) La predicción de propiedades mediante técnicas computacionales debe contrastarse con investigaciones experimentales siempre que sea posible. En esta Tesis, para el material $Ca_4Fe_9O_{17}$ se ha realizado un estudio experimental que demuestra una cierta actividad electroquímica en celdas de litio. El ensayo de material en celdas de calcio está limitado por los electrolitos disponibles actualmente, y que permiten trabajar hasta 4 V vs. Ca^{2+}/Ca. Por tratarse de un material de alto voltaje (dato DFT 4.17 V), sería necesario desarrollar electrolitos con una amplia ventana de estabilidad electroquímica. Así mismo, los resultados experimentales ponen de manifiesto la importancia del diseño de celda, y de los protocolos experimentales que contribuyen a la polarización del electrodo. En resumen, mientras que DFT es una metodología apropiada y eficaz para cribar materiales de electrodo, las

limitaciones experimentales deben solventarse de cara al examen de estos materiales a nivel de laboratorio.

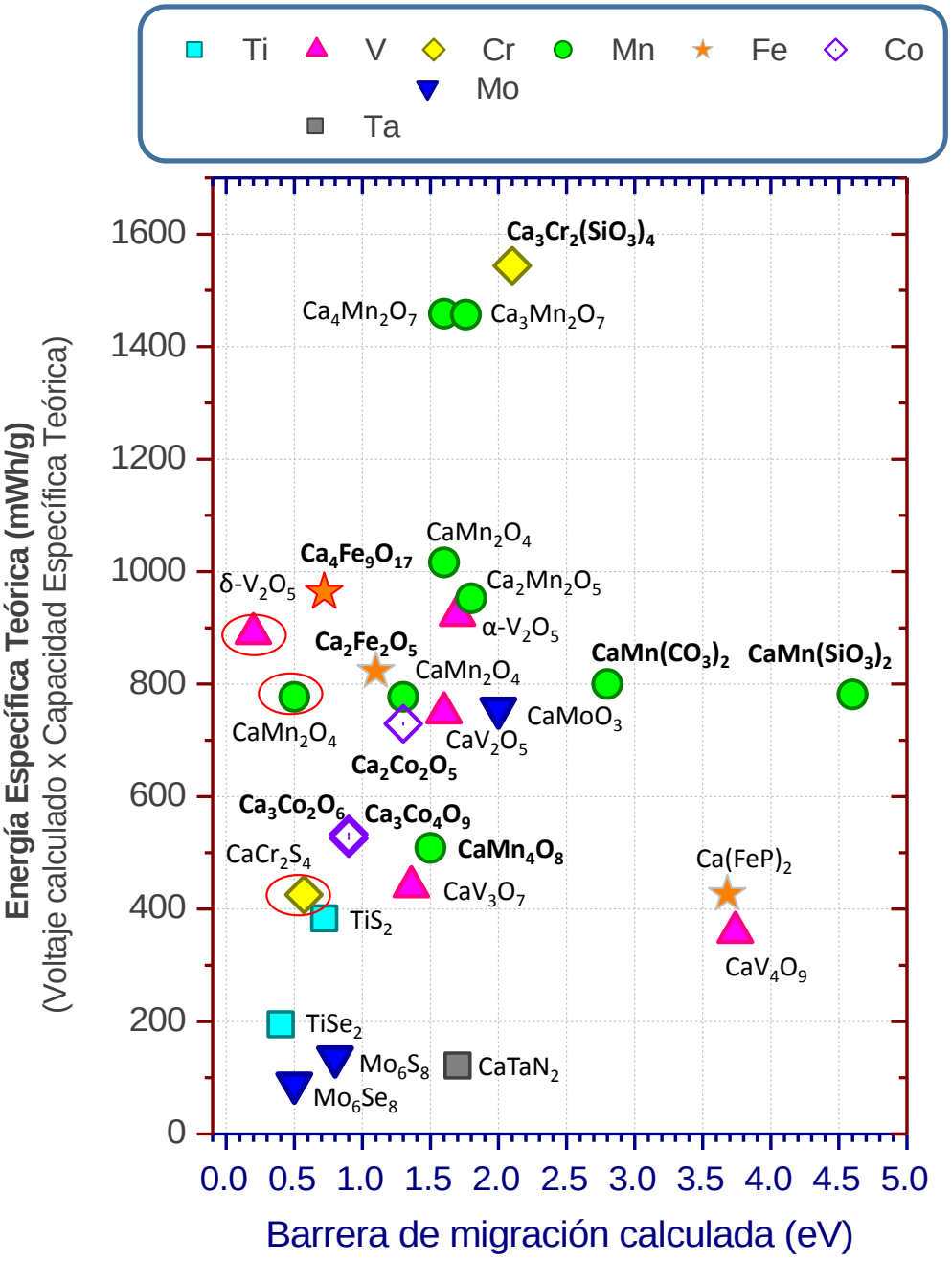

Figura 7.1. "Mapa" de energía específica frente a barrera de migración. Los datos de voltaje y energía de migración han sido calculados mediante la metodología DFT/NEB. Los materiales estudiados en esta Tesis se señalan en negrita. En rojo se indican los materiales "virtuales", que no se han sintetizado hasta la fecha. Figura adaptada de Arroyo et al. "Achievements, Challenges and Prospects of Calcium Batteries" Chemical Reviews 2020.